DEFECT ENGINEERING ON ZNS SURFACES: IMPACTS ON ELECTRONIC STRUCTURE, OPTICAL PROPERTIES, AND SURFACE REACTIVITY FROM A SOLID-STATE PHYSICS PERSPECTIVE

A Thesis

Presented to the Brazilian Center for Research in Physics in Partial Fulfillment of the Requirements for the Degree of Doctor of Philosophy

> by Pablo R.A de Oliveira Jun 2025



MINISTÉRIO DA CIÊNCIA, TECNOLOGIA E INOVAÇÃO



"DEFECT ENGINEERING ON ZnS SURFACES: IMPACTS ON ELECTRONIC STRUCTURE, OPTICAL PROPERTIES AND SURFACE REACTIVITY FROM A SOLID-STATE PHYSICS PERSPECTIVE"

PABLO RIBEIRO ALVES DE OLIVEIRA

Tese de Doutorado em Física apresentada no Centro Brasileiro de Pesquisas Físicas do Ministério da Ciência Tecnologia e Inovação. Fazendo parte da banca examinadora os seguintes professores:



Fernando Loureiro Stavale Junior - Orientador/CBPF

Jorge Anibal Boscoboinik 18 de julho de 2025 Jorge Anibal Boscoboinik – BNL-USA

Eduardo Cisternas - UFRO-CHI

GOV.DY RENATAANTOUN SIMAO Data: 13/10/2025 15:16:52-0300 Verifique em https://validar.iti.g

Renata Antoun Simão - UFRJ

Tulio Costa Rizuti da Rocha - CNPEM-BR

Rio de Janeiro, 15 de julho de 2025.

Centro Brasileiro de Pesquisas Físicas Rua Doutor Xavier Sigaud, 150, URCA, Rio de Janeiro, Brasil Tel.: +55 21 2141-7100 CEP:22290-180 http://www.cbpf.br

DEFECT ENGINEERING ON ZNS SURFACES: IMPACTS ON ELECTRONIC STRUCTURE, OPTICAL PROPERTIES, AND SURFACE REACTIVITY FROM A SOLID-STATE PHYSICS PERSPECTIVE

Pablo R.A de Oliveira, Ph.D.

CBPF 2025

Abstract

In this thesis, we explore defect engineering in metal sulfide systems, with particular focus on Zinc Sulfide (ZnS) surfaces. By integrating surface-science spectroscopic methods—particularly ultra-high vacuum and ambient-pressure X-ray photoelectron spectroscopy (XPS and AP-XPS)—with first-principles Density Functional Theory (DFT) calculations, we systematically investigate how defects influence ZnS properties. We show that introducing zinc vacancies transforms the insulating ZnS surface into a more conductive structure. Cation-defect engineering also enhances ZnS's optical response, extending its absorption and emission into the visible range. Additionally, ZnS surfaces modified with zinc vacancies develop new catalytic sites that promote reactions with oxygen-containing species. Upon oxidation, these defective surfaces evolve into a type-II ZnO/ZnS heterostructure. Zinc vacancies also drive CO_2 adsorption and CO oxidation on ZnS. This work provides a solid-state-physics-based foundation for understanding defect-induced phenomena in semiconductors. These results highlight the potential of defect engineering as a strategy for tuning the electronic, optical, and catalytic properties of ZnS-based systems.

Resumo

Nesta tese, exploramos a engenharia de defeitos em sulfetos metálicos, com foco nas superfícies de sulfeto de zinco (ZnS). Combinando técnicas espectroscópicas de ciência de superfícies — especialmente XPS e AP-XPS — com cálculos de primeiros princípios baseados na Teoria do Funcional da Densidade (DFT), investigamos como os defeitos modificam as propriedades do ZnS. Mostramos que vacâncias de zinco tornam a superfície isolante do ZnS mais condutora. A engenharia de defeitos catiônicos também intensifica sua resposta óptica, ampliando a absorção e emissão para a faixa visível. Além disso, essas vacâncias criam sítios catalíticos ativos para reações com espécies oxigenadas, e a oxidação dessas superfícies leva à formação de uma heteroestrutura tipo-II ZnO/ZnS. Também demonstramos que vacâncias de zinco favorecem a adsorção de CO_2 e a oxidação de CO. Este trabalho oferece uma base sólida, fundamentada na física do estado sólido, para entender fenômenos induzidos por defeitos em semicondutores. Os resultados destacam o potencial da engenharia de defeitos como estratégia para ajustar propriedades eletrônicas, ópticas e catalíticas de sistemas baseados em ZnS.

Contributions derived from this

thesis

Scientific articles

1. Zinc blende ZnS (001) surface structure investigated by XPS, LEED, and DFT

P. Oliveira, C. Arrouvel, F. Stavale 10.1016/j.vacuum.2024.113566

2. Formation mechanism, stability and role of zinc and sulfur vacancies on the electronic properties and optical response of ZnS

<u>P.R.A. Oliveira</u>, L. Lima, G. Felix, P. Venezuela, F. Stavale 10.1088/1361-6463/ae048a

3. Growth and Surface Characterization of a Type-II ZnO/ZnS Heterostructure

P.R.A. Oliveira, I. Coelho, G. Felix, P. Venezuela, F. Stavale 10.1021/acs.jpcc.5c05124

4. Insights into CO2 adsorption on ZnS surfaces

<u>P.R.A. Oliveira</u>, P. Venezuela, F. Stavale, J.Boscoboinik (Manuscript in submission) 5. CO co adsorbs on defective ZnS surface

<u>P.R.A. Oliveira</u>, C.F.Codeço, P. Venezuela, F. Stavale, J.Boscoboinik (Manuscript in preparation)

6. Niobium doping of CVD-WS2 monolayers using solid precursors with and without salt-KBr as a catalyst: A comparative study

N Stand, AN Barbosa, <u>P.R.A. Oliveira</u>, CD Mendoza, FL Freire Jr 10.1016/j.apsusc.2024.159816

7. Ti1-xAlxN or TiN+ AlN: An investigation about Al influence on titanium aluminum nitride thin films structural organization

I.Lemos, <u>P.R.A. Oliveira</u>, RL Rezende, L.F.S. Sabino, I.Z Damasceno, F. Stavale, E.K Tentardini

10.1016/j.ceramint.2024.11.157

Main Conference Contributions

1. Defect Engineering of ZnS surfaces: Where real world challenges meet solid state physics

P.R.A. Oliveira, F.Stavale

Physical Electronics Conference (PEC), Brookhaven, NY (Aug 2025):

Oral presentation as one of the Nottingham Prize finalists, showcasing my overall thesis research results.

2. AP-XPS and DFT investigation of CO2 adsorption and CO oxidation on ZnS surface

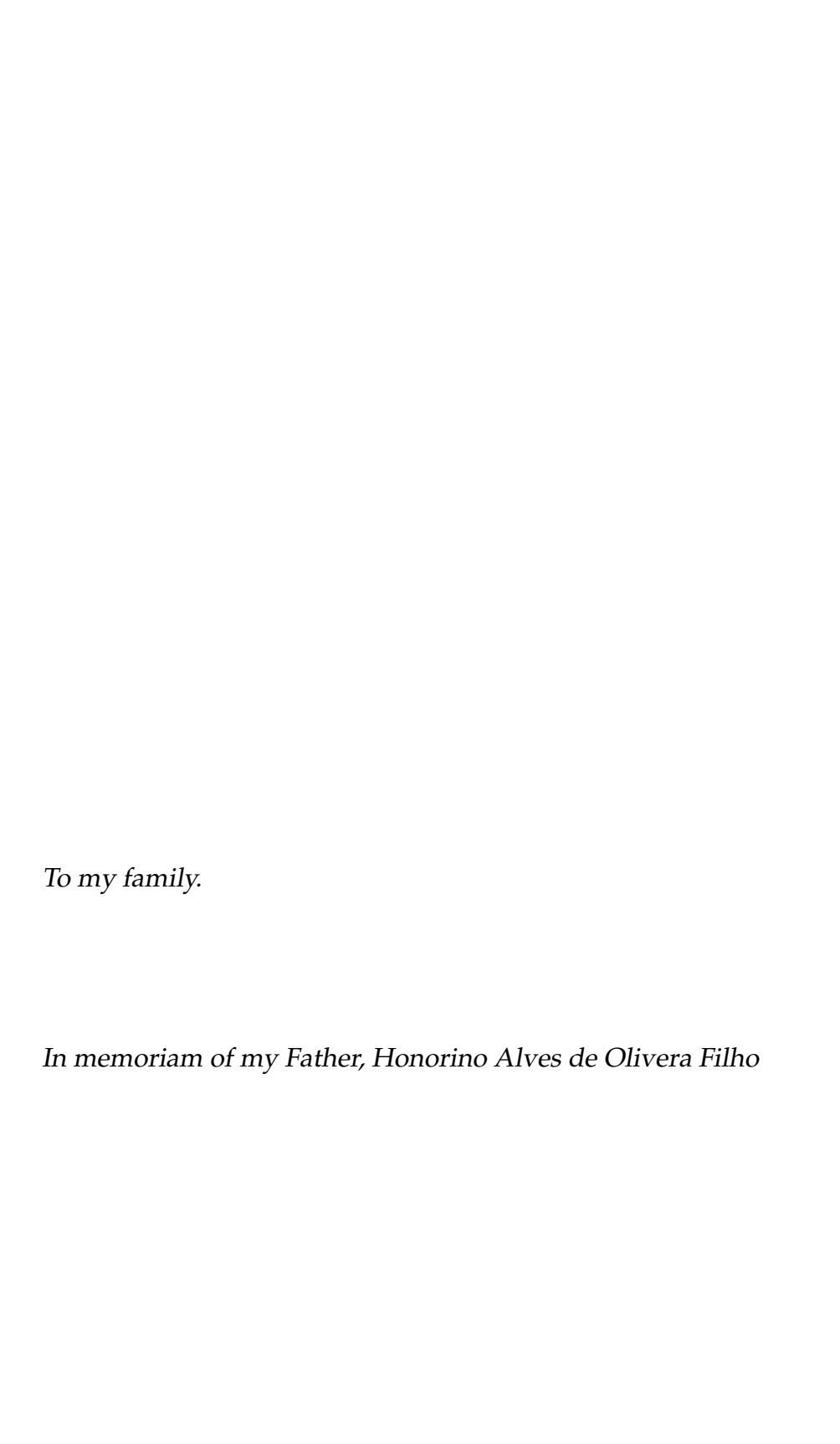
P.R.A. Oliveira, P.Venezuela, F. Stavale, J.Boscoboinik

Brazilian-German Workshop on Applied Surface Science, Oberstdorf, (Sept 2025): Oral presentation on CO_2 action and CO oxidation on ZnS defective surface combining AP-XPS and DFT modeling.

3. The in-situ formation of a ZnO/ZnS heterostructure

P.R.A. Oliveira, I.Coelho, G. Felix, F. Stavale

Best Poster award at the Autumn meeting of the Brazilian Physical Society, Para 2025



Acknowledgements

The scientific journey is often marked by several challenges both external and internal. Throughout this path, I have been fortunate to receive unwavering support from many people across different stages of my life and work.

First and foremost, I thank God, who made the impossible possible. The place from where you come cannot limit your horizons. Dream is still for free, so why not dream bigger I did, but not only did it. I had to give everything I had to turn those dreams into reality. If I had to go through everything again, I would. Without hesitation.

I am deeply grateful to my family in Bahia. Though far away, their support has always been present. Much of my motivation comes from the desire to make my mother's dream come true. Dona Sueli, this achievement is for you! Also to my brothers, Patricio and Patrick, and my sister, Luiza, for their love and encouragement. I also acknowledge my uncle Zeca, who has been like a father throughout my life. And to my father, who now rests in heaven. His lost during my first year of PhD was a devasting storm with a lasting impact. Yet, that pain pushed me forward. I hope you are proud of all that I've achieved. Your absence is deeply felt, but your strength continues to live on in me.

In addition to my family, I've been blessed with friends who became family. To Paulo and Jhonny and their families—thank you for always being close

since my childhood. I could not forget to mention 'Seu Anselmo' and his family, notably his daughter Fernanda, who was always pushing me forward and believing in my dreams. Fortunately, At CBPF, I found a community that supported me both scientifically and personally. I thank everyone from Lab 112 B, especially my Advisor Dr. Fernando Stavale, for his patience, guidance, and the many opportunities he provided. I'm also thankful to my colleagues Dr. Astrid, MSc Igor, Guilherme, and Luiza for the joyful memories we made. Still on CBPF, I thank Dr. Philipe Fabritis, MSc Carlos Rodolfo, and Dr. Henrique for the great discussions and memorable times we shared, especially in the "República do Dendê," one of the most unforgettable parts of my life in Rio. A special thanks to Munique Araújo, for her kindness and the funny moments we shared, especially during the 2025 Autumn Meeting. I also thank the entire CBPF staff, from the director, Dr. Márcio, to the reception and security teams, despite most of them not supporting Vasco da Gama!

I want to acknowledge external collaborators, especially my friend Dr. Emmanuel Victor from the Federal University of Uberlândia, for always cheering me on. I am also grateful to Prof. Pedro Venezuela from UFF for his unwavering support and valuable guidance. My special thanks go to the BNL staff, especially Prof.Dr Anibal Boscoboinik and his group. The period I lived there was the most exciting and inspirational phase of my academic journey. Prof. Anibal is not only a brilliant scientist but also one of the kindest individuals I've had the pleasure to meet. Also BNL is a unique environment with deep values too beyond the massive search for results. I had the privilege of meeting many incredible people during my time there, including Dr. Shyam Patel and Dr. Steven Arias—two friends I'll carry with me for life. I also thank Eliseo Pérez, my fun and sharp Argentinian buddy, along with Drs Mueed, Laiba, Tani, Tian-

hao, Ashley, and Sabrina, for their friendship and support. A special mention goes to Dr. Peter Sun—I miss our daily scientific discussion in my cubicle. I learned so much at BNL, but most importantly, I discovered the best version of myself.

And of course, I must highlight the unforgettable soccer sessions. Thank you, Ricardo, Olensky, Kazu, Billy, and the entire BNL team, for making those moments so joyful—on and off the field.

In the end, this thesis is not just a personal achievement. It is the result of a collective journey, and I am deeply grateful to everyone who walked this path with me.

Siiii!.

Table of Contents

	Abs	tract	4				
	Con	tributions derived from this thesis	iii				
			vi				
	Ack	nowledgements	⁄ii				
	Tabl	e of Contents	Х				
	List	of Figures	aii				
1	Introduction 1						
	1.1	General Overview	1				
	1.2	Thesis outline	4				
2	Met	hods: General Survey	7				
	2.1	XPS	7				
	2.2	DFT framework	14				
3	ZnS zinc blende investigated by LEED, XPS, and DFT 18						
	3.1	Motivation and challenges	18				
	3.2	Results and discussion	21				
4	For	mation mechanism, stability and role of zinc and sulfur vacancies					
	on t	he electronic properties and optical response of ZnS	29				
	4.1	J	30				
	4.2		32				
	4.3		35				
		J	35				
		1 1 \mathbf{J}	37				
		J	41				
		J	43				
		4.3.5 Optical properties calculations	1 5				
5	In situ growth of a type-II ZnO/ZnS heterostructure: From stability to						
	ban	d-offset	50				
	5.1	1	50				
	5.2		51				
	5.3	Results and discussion	54				

		5.3.1	XPS analysis	54
		5.3.2	AFM analysis	58
		5.3.3	Electronic structure analysis	61
		5.3.4	Band offsets	64
6	Insi	ghts in	to CO_2 adsorption and CO oxidation	70
	6.1	Overa	ll contextualization	70
	6.2	Usefu	l background review	71
		6.2.1	Adsorption mechanism: Chemisorption x Physisorption .	71
		6.2.2	Modeling molecule adsorption	72
	6.3	Resul	ts and Discussion	73
		6.3.1	CO_2 adsorption	74
		6.3.2	On the activation mechanism	76
		6.3.3	Mixing atmosphere: $CO_2 + O_2 \dots \dots \dots \dots$	84
		6.3.4	CO oxidation	92
7	Gen	eral Re	emarks	99
A	Furt	her Ex	perimental details	100
		-	le preparation and description of further experimental tech-	
			S	100
	A.2		ve Atomic concentration - IMFP correction scheme	103
			ilm thicker estimation through the Thickogram method	104
			gap estimation from XPS	106
В	Furt	her Co	mputational details	109
_			outational method	
		_	$BE - \alpha$ method	

List of Figures

2.1	Schematic illustration of relevant energy terms in XPS	8
2.2	(a) Illustration of processes that electron can undergo when leav-	
	ing the solid. (b) Comparison of XPS spectra with and without	
	Monochromated source	10
2.3	General XPS setup (a) and (b) foundations of a hemispherical	11
2.4	electron analyzer	11
2.4	lab; (b) The NAP XPS machine itself at the Interface's lab	13
2.5	Illustration of the Self-Consistent Cycle	16
 .0	indication of the sen consistent cycle	10
3.1	Schematic side (left) and top (right) view of the ZnS (001)struc-	
	ture. Blue and yellow balls denote zinc and sulfur atoms, respec-	
	tively. The (001) plane is marked in pink. The bulk and surface	
	lattice parameter are highlighted by a black and red square, re-	20
3.2	spectively	20
J.Z	with flood gun and ZnS (001) after a high surface treatment	
	with annealing temperature at 1420 K (black, blue and red	
	curves, respectively). (b) Zn 2p (c) S 2p and (d) Zn 3p core-level	
	spectra. All the spectras were acquired at room temperature	21
3.3	Quantification of the relative atomic concentration based on the	
	S 2p and Zn 3p peak regions as a function of (a) sample UHV an-	
	nealing temperatures at normal photoemission geometry and (b)	
	the photoemission take-off angle geometry for a fixed tempera-	
	ture (at 1420 K). In (a) the S 2p and Zn 3p regions were collected	
	with the assistance of an e-flood gun at the conditions described in the experimental section, except for the 1420 K annealed sam-	
	ple. In (b) the S 2p and Zn 3p regions were analyzed as collected.	25
	pie. In (b) the 5 2p and 211 5p regions were analyzed as concered.	20

3.4	In (a), (b), and (c)/(d) are shown LEED patterns obtained for samples prepared at annealing temperatures of 473 K, 1320 K, and 1420 K, respectively. In (e), the LEED intensity line profile is shown for the black line indicated/labeled in (d). In (f) is depicted the LEEDpat simulated pattern for the proposed (1x2) reconstructed surface structure. The double-circled points denote the ideal (1 \times 1) arrangement, while the reconstruction finger-print is provided by the two extra points (in black) between each line. All LEED pattern photographs were adjusted to enhance their contrast for clarity	27
4.1 4.2	Radiative (a) and non-radiative (b) recombination process XPS spectra of bare and UHV annealed ZnS single crystal. (a) survey scan and (b) small region analysis spanning from S 2p to Zn 3p. All the spectra were acquired at room temperature and at	33
4.3	normal emission	35
4.4	perature	37
4.5	tion of the electronic chemical potential in an S-rich scenario Projected Density of states of (a) pristine, (b) V_{Zn}^0 , (c) V_{Zn}^{-1} , (d) V_S^0	41
	and (e) V_S^{+2} doped ZnS.The VBM was shifted to 0 eV for clarity	43
4.6	Theoretical absorption spectra of of (a) pristine, (b) neutral V_{Zn} and (c) charged V_{Zn} ZnS	45
4.7	Joint Density of states (JDOS) of (a) pristine, (b) neutral V_{Zn} and (c) charged V_{Zn} ZnS. Pictorial diagram level illustrating the emissions in the (d) pristine and (e) p-doped scenarios	47
5.1 5.2	Illustration of some Heterostructure prototypes XPS (a) Survey and (b) high-resolution O 1s analysis of the ZnS sample after several oxidation cycles; (C) Zn 3p x O1s relative atomic concentration and (d) film thickness estimation as a function of the oxidation cycle. All the spectra were collected at Room temperature in UHV conditions. All binding energies were calibrated with respect to the Zn 3s orbital	52 54

5.3	Tapping-mode AFM measurements of the ZnS (001) single-crystal (a) before and (b) after obtaining a ZnO/ZnS heterostructure. (C) Phase image of the height AFM image in (b). The up-	
	left corner inset emphasizes the hexagon-like shape, as pointed	
	by the red contour with 6 blue points in each vertices	58
5.4	High-Resolution XPS spectra of (a) Zn 2p, (b) S 2p, and (C) Zn	
5.5	LMM. All the spectra were collected at room temperature Valence band XPS spectra of (a) ZnS (b) ZnO (c) and ZnO/ZnS system. In (d), (e) and (f) are displayed the valence band maximum action time for all the spectrum to the mantiaged and an arrangement of the spectrum to the spectrum of the sp	61
	mum estimation for all these structures, in the mentioned order.	
E (All the spectra were collected at room temperature	64
5.6	(a) Reliable XPS spectra to get the core-level shift estimation. (b)	
	Pictorial band diagram illustrating the individual ZnO and ZnS	((
	configuration before contacting vs the hybrid system junction	66
6.1	APXPS operando analysis of (a) Zn 2p (b) O 1s spectra as a function of the heating temperature; (C) Relative atomic concentra-	
	tion of the C 1s components after cycles as a function of the tem-	
	perature.	74
6.2	(a) C 1s components after NAP experiments at 0.55 mbar (top	
	panel) and 0.1 mbar (bottom panel) of CO_2 ; (b) C 1s components	
	relative concentration as a function of the pressure of CO_2 used	
	in the experiments. In all cases, the sample was heated at 573 K	79
6.3	Zn 2p (left panel) and C 1s (right panel) of ZnS after a reaction	
	in a mixed CO+CO ₂ atmosphere (a) at 573 K and (b) 673 K The	
	spectra called "before" means the system right before start the	
	AP-XPS experiments, while the label "After" stands for spectra	
	collected after AP XPS experiments, at room temperature	81
6.4	Zn 2p (a) C 1s (b) and (c) O 1s components before (bottom panel)	
	and after (top panel) AP XPS experiments in a mixed environ-	
	ment of O_2 and CO_2 . All the spectra were collected at Room tem-	
	perature. In these experiments, the sample was heated up to 573	_
	K	84
6.5	DFT modeling of ZnS pristine (a),(b), and doped (c),(d) before	0.0
	(left panel) and after (right panel) interacting with CO_2	88
6.6	DFT modeling of ZnS pristine (a),(b), and doped (c),(d) before	00
(7	(left panel) and after (right panel) interacting with O_2	90
6.7	Zn 2p (a), C 1s (b), and O 1s(c) before (bottom panel) and after	
	(top panel) AP-XPS experiments in a stoichiometric CO + O_2 at-	
	mosphere. During the experiments, the samples were heated at 573 K. All the spectra were collected at room temperature	Ω
	3/3 N. An the spectra were conected at room temperature	93

6.8	Zn 2p (a), C 1s (b), and O 1s(c) before (bottom panel) and after	
	(top panel) AP-XPS experiments in an oxygen-rich CO + O_2 at-	
	mosphere. During the experiments, the samples were heated at	
	573 K. All the spectra were collected at room temperature	95
6.9	DFT model of CO oxidation on ZnS surface	96
A.1	The thickogram method	105
A.2	The band gap estimation method applied on (ZnS) and (ZnO)	
	systems	108

Chapter 1

Introduction

1.1 General Overview

Over the time, several social demands have been overcome due to advances in semiconductor physics. The scalability, high performance, and robust architecture of electronic devices were some of the challenges of recent decades that were resolved by improving the understanding of the electronic properties of these materials, especially at the atomic level [1]. Nowadays, the rise of greenhouse gases and the energetic crisis are some of the main society's concerns. For this reason, the replacement of 'dirty' energy sources by renewable alternatives have been discussed worldwide. Once again, the hope for solving theses problems relies on semiconductor's physics advance. There has been a significant increase in studies exploring new materials for applications in photovoltaic energy, and catalyst platforms that might be used to convert pollutant gases such as CO2 and CO into green-friendly products such as methanol and hydrogen

The requirement for the choice of the model system is solid states guided. For instance, for achieving a high efficiency of solar cells, the reduction of lose mechanism such as thermal and material lose are need. In a solid state physics point view, this mean that materials with indirect band gap and high degradation are not suitable for this kind of application. Still, given the wide energy solar radiation, a potential candidate for solar cells must pursue a wide and tunable band gap, which could allow for broadening its absorption energy [3]. On photocatalytic process like the CO_2 reduction reaction, CO oxidation, or hydrogen and oxygen evolution reaction, it is important ensure that the catalyst surface display active sites, in addition to electronic edges level matching the energy required for these reaction take place, as well as efficient charge separation for obtaining the final products [4]. Over the past decades, various material classes like metal oxides [5], perovskites [6], halides [7], and nitrides [8], have been explored for heterogeneous catalysis. However, despite their promising activity, these materials often suffer from intrinsic limitations, including low catalytic efficiency, poor long-term stability, and complex synthesis routes

Metal sulfides, on the other hand, have emerged as an attractive alternative due to their abundance, electronic tunability, and durability, making them a strong candidate for next-generation catalytic platforms [9]. Its ideal electronic structure, with a less positive valence band occupied by S 3p states and small effective mass that allow a fast charge carrier dynamic in both intrisic and hybrid system (heterostructures materials) [10]. One of the main question on metal sulfide class is the wide band gap of several special materials, especially binary metal sulfides Despite wide band gap materials display a UV- response range,

for photocatalysis, as aforementioned, a visible light-response range must be achieved. Furthermore, the low conductivity of some sulfide hamper some surface science investigations. To overcome both barriers, defect engineering on metal sulfide materials has been widely explored [11, 12]. The band gap modulation is achieved either by removing native species as including substitutional impurities in the lattice. Indeed, point defects, such as vacancies, interstitials, and substitutional impurities, introduce localized electronic states that can promote charge transfer and lower adsorption energy barriers [13]. In particular, it might allow for the formation of hybrid interfaces, giving rise to the well-known heterostructure, which is another promising strategy for enhancing the overall reactivity of sulfide systems

Among the various metal sulfides, zinc sulfide (ZnS) stands out due to its long-standing role in optoelectronic devices. It is one of the earliest known metal sulfide semiconductors ¹, widely reported for applications in light-emitting devices and sensors. However, its high resistivity and large band gap (close to 3.6 eV) have historically limited its application in solar energy conversion and photocatalysis. In this direction, the doping on ZnS arises as a good strategy to overcome this issue. *Bao and Colleagues* reported that the replacement of zinc atom by a cobalt atom in the wurtzite structure promotes impurity levels in the valence band, in addition to shift the conduction band downward, hence decreasing the band gap and enhancing the absorption in the visible light range [14]. A similar effect is reported by *Pang* [15]. It is reported that zinc vacancies are responsible for the improvement in the material's optical response. Despite these interesting results, it is worth to note that ZnS most stable phase is the Zinc Blende [16]. Moreover, it might facilitate the formation of oxide/sulfide

¹It was used in the historical Rutherford experiment

system. In this case, the built-in electric field generated after the contact between the species further enhances charge separation efficiency, creating a type-II heterostructure configuration that optimizes electron and hole transport. In addition, it might play a role in CO_2 adsorption reactions, providing active sites that intermediate Van der Waals-like interactions between molecules and the semiconductor's surface [17, 18]. Thus, much efforts to fully understand how to improve the ZnS properties via defect-engineering would be expected . Curiously, advances in this regarded are still limited. Indeed, as mentioned above, the poor conductivity of ZnS hinders surface science techniques experiments like XPS and LEED, which might explains the lack of investigations on ZnS surfaces and defect-driven phenomena on this structure.

1.2 Thesis outline

In this thesis we explored ZnS single crystals, especially ZnS (001) surfaces. Combining traditional surface techniques and firs-principles calculations we investigate the fundamental electronic, optical, and catalytic properties of ZnS, with particular emphasis on defect engineering. For this purpose, this thesis is based on four main problems: (i) Surface modification on ZnS (001); (ii) impacts on electronic and optical structure due to point defects on ZnS; (iii) New interface design on defective ZnS surfaces; (IV) CO_2 adsorption and CO oxidation on defective ZnS surfaces. Before entering in the core part of the results and discussion section of each of these problems, a short motivation as well as useful background review are provided. Overall, to provide a logic connection between the problems and strategy employed to solve them, this thesis is struc-

tured as follows:

- Chapter 2: Provides general information on the experimental and theoretical methods used in this thesis. Focusing on XPS and DFT, this chapter guides the reader into the main methods employed throughout the thesis.
- Chapter 3: Discuss the general features of the zinc blende ZnS (001) surface, based on XPS, LEED and DFT investigations. This is the first problem pointing on the role of zinc vacancies on electronic properties of ZnS surfaces.
- Chapter 4: Unveil the role of native vacancies on electronic and optical properties of ZnS. Inspired by the findings derived by the first problem, we computed the formation energy of sulfur and zinc vacancies at different charge states, besides comparing the electronic and optical properties, combining XPS, Photoluminescence and DFT analysis.
- Chapter 5: We discuss the in-situ formation of a type-II ZnO/ZnS heterostructure. Once the first two problems suggest that zinc vacancies on ZnS drives ultimately improvements on electronic and optical properties, we believe this scenario favor reactivity on ZnS. By exposing the system to an oxygen atmosphere, we studied the oxygen evolution in the ZnS (001) surface. Notably, exploring the band-alignment model, we computed the bending of the bands upon the full formation of the hybrid interface.
- Chapter 6: After the success results from the oxidation of ZnS surfaces, we aimed to explore further reactions with oxygen-containing molecules such as CO_2 and CO. Therefore, this chapter provides fruitful insights into CO_2 adsorption and CO oxidation on ZnS. Based on AP-XPS measurements and DFT calculations, we reported that cation vacancies allow CO_2

to adsorb on ZnS surfaces via a partial dissociation mechanism. Moreover, we reported oxygen-rich atmosphere is the driving force for promoting the CO oxidation on defective ZnS surfaces, which takes place via a co-adsorption mechanism.

Ending, details regarding experimental and computational methods are provided in the Appendix A and B, respectively.

Chapter 2

Methods: General Survey

2.1 XPS

General aspects

X-ray photoelectron spectroscopy (XPS) is a highly effective technique for probing the surface composition and electronic structure of various materials. The power of XPS stems from both theoretical insights, such as Einstein's foundations on the photoelectric effect, and significant experimental advancements, notably the development of sophisticated ultra-high vacuum (UHV) instrumentation and electron analyzers [19]. Together, these advancements have allowed XPS to evolve beyond simple chemical-shift-based analyses, enabling detailed insights into surface chemistry, electronic states, and interface properties. In short words, XPS measures the kinetic energy of photoelectrons ejected from

a surface due to incidence of a X-ray generated photons of energy $\hbar\omega$, providing information on the binding energy of these particles. The mechanism is schematically illustrated in Fig.2.1.

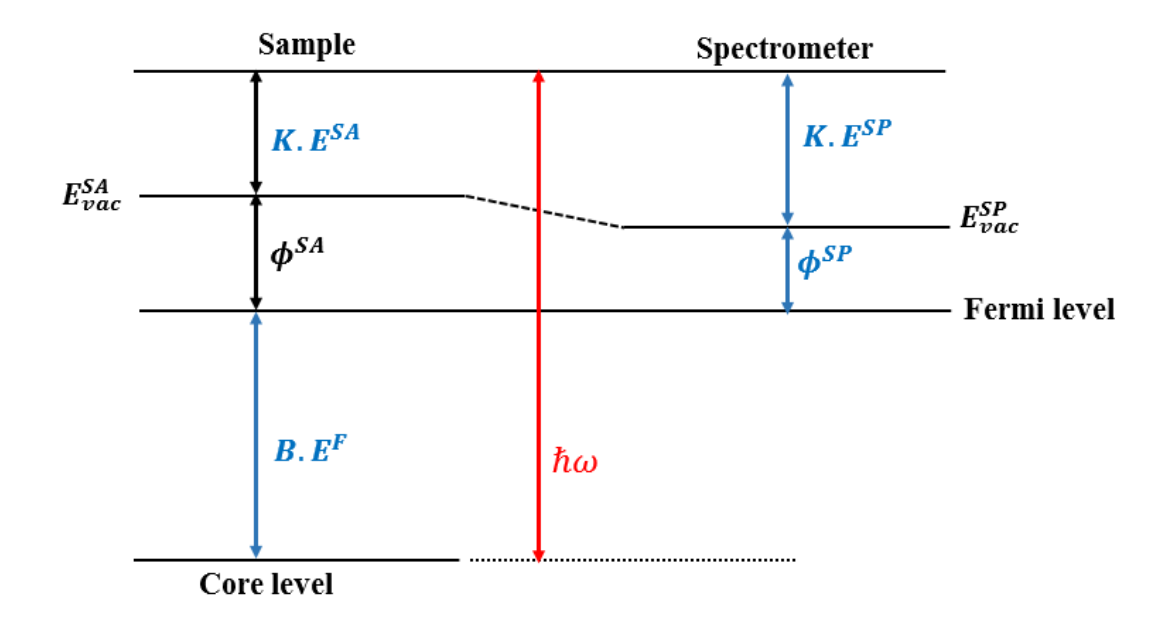


Figure 2.1: Schematic illustration of relevant energy terms in XPS.

Adapted from [20]

The electrons escape from the solid to the vacuum level after overcoming a particular potential energy, the so-called sample work function ϕ^{SA} . Given a good electrical contact between the sample and the spectrometer, the kinetic energy of the sample $K.E^{SA}$ is given by:

$$K.E^{SA} = \hbar\omega - BE^F - \phi^{SA}. \tag{2.1}$$

In Eq.2.1 $B.E^F$ denotes the binding energy of the emitted electron from the sample. This is measured is with respect to the Fermi level. From the diagram

illustrated in Fig.2.1 we can also observe that

$$K.E^{SA} + \phi^{SA} = K.E^{SP} + \phi^{SP},$$
 (2.2)

where $K.E^{SP}$ and ϕ^{SP} are the kinetic energy that the photoelectrons reach the spectrometer and the work function of the spectrometer, respectively. It worth noting XPS computes $K.E^{SP}$ rather than $K.E^{SA}$. Fluctuations in the measured binding energy with no physical meaning are strictly related to deviations from the spectrometer work function rather the sample work function. Indeed, Combining Eqs.2.1 and 2.2, one can note that the binding energy of the sample is independent of the sample work function:

$$B.E^F = \hbar\omega - K.E^{SP} - \phi^{SP} \tag{2.3}$$

The spectrometer work function is constant, usually calibrated before the experiments. Therefore, given a core level and ensuring a well performed spectrometer calibration, deviations in the B.E are uniquely addressed to electronic screening or charge redistribution, leading to either under or overcompensation of the generated electron-hole pair. This aspect is quite interesting for semiconductor's sample and will be discussed in details throughout this thesis.

Information derived from XPS are limited to the mean distance that electrons can travel without undergoing energy loss collisions as they escape from the sample surface. This quantity is called Inelastic Mean Free Path (IMFP), that in general varies from 5 up to 15 nm. In this range, detailed information regarding the core-level region are provided, making XPS a powerful tool for probing

the surface of a material. The XPS signal takes into account both elastic (vast majority of XPS signal) as well as inelastic contributions - related to several energy loss mechanisms, such as surface and bulk plasmons, or instrumental artifacts such as radiation backscattering [21]. To mitigate such undesired contributions, Monochromated X-ray sources are commonly employed. An example comparing XPS events and a monochromatic and non-monochromatic XPS spectra is shown in Fig.2.2(a) and (b), respectively.

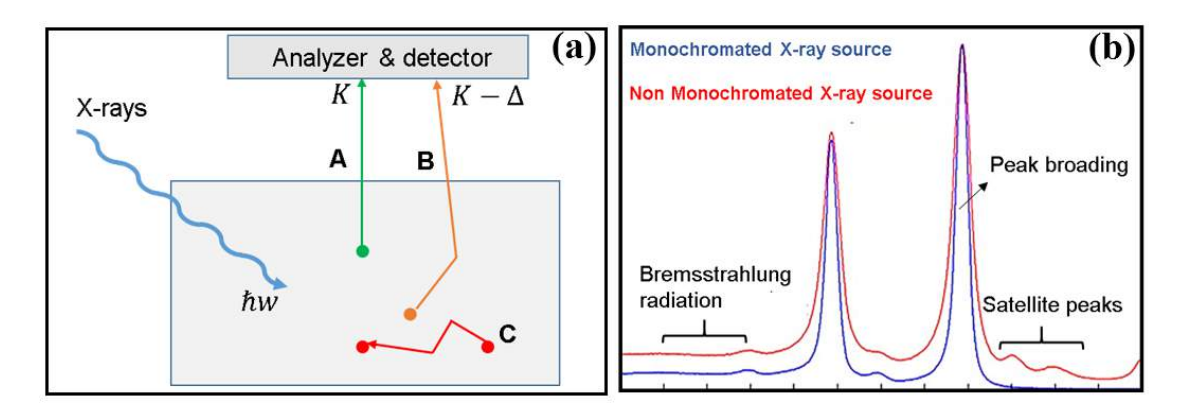


Figure 2.2: (a) Illustration of processes that electron can undergo when leaving the solid. (b) Comparison of XPS spectra with and without Monochromated source.

Adapted from [22] and [23]

The background of XPS spectra might play a role in XPS analyses. Although linear and Shirley line shapes are commonly employed, Tougaard method provides a more robust and physically meaningful approach for background subtraction [24]. Beyond background selection, determining the optimal line shape for individual peaks also constitutes a critical step in XPS analysis. Typically, XPS peak profiles are described by a mixed Gaussian-Lorentzian function, often called a Voigt or pseudo-Voigt profile. The optimal mixing parameter between Gaussian and Lorentzian components can be identified by systematically fitting test peaks and minimizing the overall residuals of the peak-fitting

procedure [25]. Proper handling of these parameters is crucial before utilizing more advanced analytical capabilities of XPS, such as relative atomic quantification, band-gap estimation, and thin-film thickness determination [26]. These methodological details and their practical implementation are further elaborated in Appendix A.

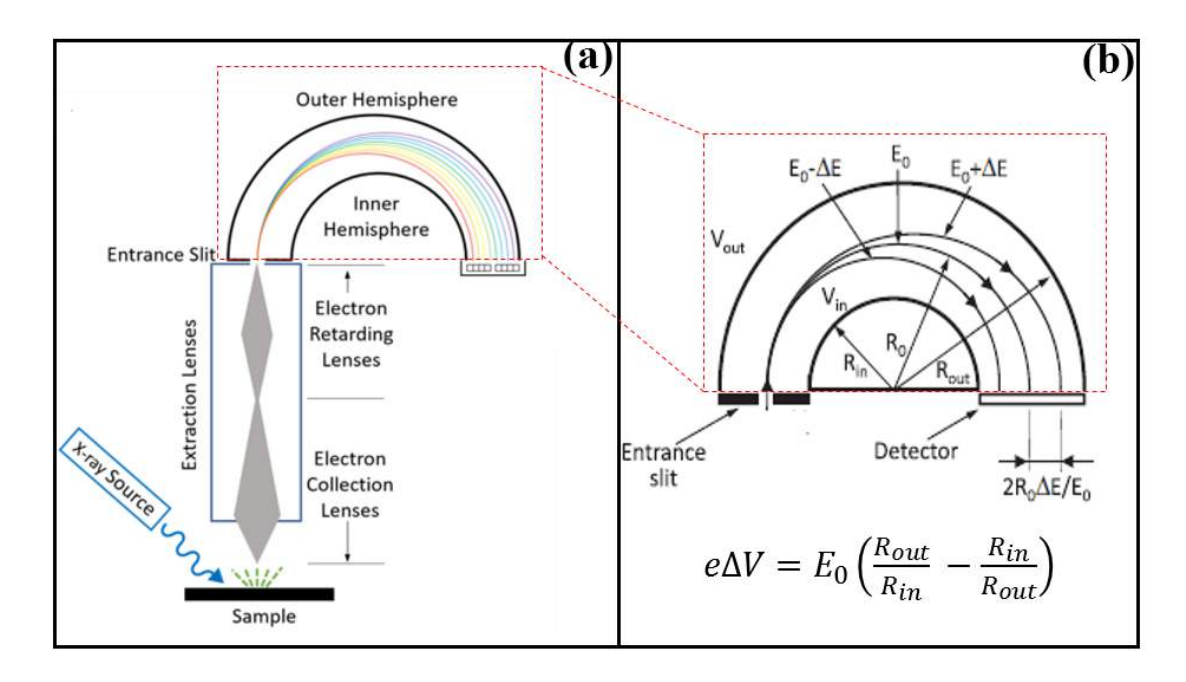


Figure 2.3: General XPS setup (a) and (b) foundations of a hemispherical electron analyzer.

Adapted from [19]

Traditional XPS setup requires an UHV system coupled with an electrostatic lens system that accelerates the photoelectrons toward the electron analyzer, with this last part being the heart of XPS. Although cylindrical analyzers were the former shape, hemispherical shapes are the most employed setup nowadays. Fig.2.3 (a) illustrates the overall XPS setup. The analyzer consists of two hemispheres, called "inner" and "outer" hemispheres, from which the photoelectrons pass before reaching the detector. Its major function is to filter the photo-

electron energy, by setting the minimum energy allowed to pass through them, i.e., the *Energy pass*. Fig.2.3 (b) illustrate some features of an electron analyzer. Essentially, by applying a potential difference ΔV between the inner and outer hemispheres, the electron selectivity will be limited to the energy pass according to [22]:

$$e\Delta V = E_0 \left(\frac{R_{out}}{R_{inner}} - \frac{R_{inner}}{R_{out}} \right)$$
 (2.4)

Although traditional XPS systems are limited to UHV range, recent progress in UHV instrumentation has allowed the improvement of this technique, opening way for operating it in a pressure range close to near ambient conditions - up to 10 mbar. This new setup is well-known as NAP-XPS or AP-XPS, depending on the range of operations. The general design is shown in Fig.2.4(a). In NAP-XPS systems, a differential pumping arrangement is employed, typically involving multiple turbomolecular pumps and small apertues. This design allows the sample to remain at near-ambient pressures, while simultaneously maintaining the analyzer at UHV conditions (on the order of 10^{-7} mbar). Additionally, the X-ray source is isolated from the analysis chamber by a transparent window—commonly fabricated from silicon carbide (SiC)—to prevent gas contamination while allowing X-ray transmission. A critical element of this configuration is the use of a small aperture (approximately 3 mm diameter), often referred to as the nozzle, positioned very close to the sample surface (see inset of Fig.2.3 (a)). Photoelectrons emitted from the sample must pass through that aperture before reaching the electrostatic lens system. Typically, due to the short IMFP in gas atmosphere, electrons will experience frequent collisions when exposed to ambient conditions, which would mitigate the XPS signal. However, in the nap-xps system, the volume behind the nozzle is connected to the pump system, reducing the pressure along the photoelectron path toward the analyzer. As a result, the high-pressure path length for electrons is minimized, such that the energy loss contribution becomes narrower enough to not hinder the XPS spectra signal. In Fig.2.4 is shown the AP-XPS available at the Interfaces's lab at the CBPF.

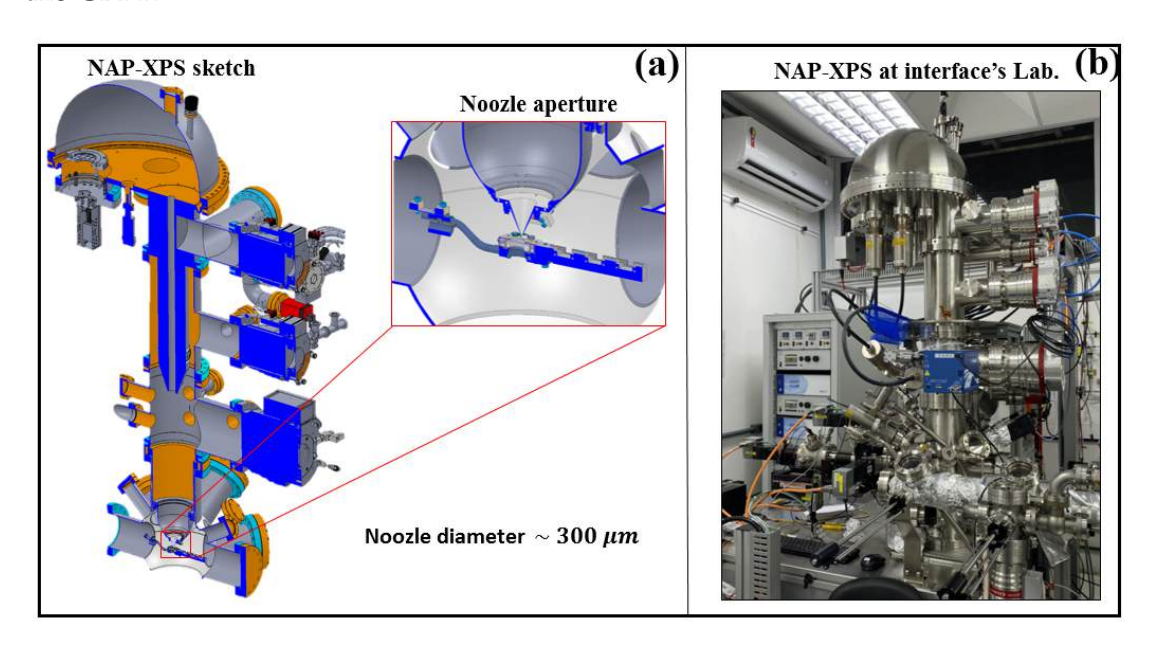


Figure 2.4: Schematic of the NAP XPS machine available at the Interface's lab; (b) The NAP XPS machine itself at the Interfcae's lab

In this thesis, we explored both traditional and AP-XPS systems. In the project one, we used a traditional XPS setup equipped with a SPECS PHOI-BOS 150 hemispherical analyzer, and a SPECES ErLEED 150 setup. XPS spectra were acquired using a monochromatic $Al - K\alpha$ source (1486.6 eV) operating at 150 W at room temperature. In the projects two and three, we used a NAP-XPS setup - Yet not exposing the system to ambient conditions in these works. The system is equipped a NAP-150 SPECS PHOIBOS hemispherical analyzer, using a monochromatic $Al - k\alpha$ X-ray source (1486.6 eV) operating at 60 W. The sample current remained below 1.5 nA during acquisition, and the chamber

pressure was maintained below 7.10^{-10} mbar. In this setup, the photoelectrons escape through an small aperture of 300 μ m, and the exposed surface is confined to < 1 mm^2 . Ending, in project 4 and 5, we explored an AP-XPS available at the *Center for Functional Nanomaterials*, at Brookhaven National Laboratory. The system is quite similar to the aforementioned described.

2.2 DFT framework

DFT is a powerful tool in Solid State Physics, providing a practical framework for predicting electronic, structural, and dynamical properties of materials. The breakthrough in this theory relies on the conversion of the problem of N interacting electrons into N non-interacting single-particle problems. The core theory behind such an achievement is the Hohenberg and Kohn paper ¹, which states the DFT theorems, establishing the relation between the external potential and the electronic density, as well stating the ground state energy as a minimum for a given exact electronic density [27]. In short, the DFT theory shed light on the solution of the following equation:

$$\int \delta \rho(\mathbf{r}) \left\{ \frac{\delta T_0}{\delta \rho} + \nu(\mathbf{r}) + \int \frac{\rho(\mathbf{r}')}{|\mathbf{r} - \mathbf{r}'|} d^3 r' + \nu_{xc} - \mu \right\} d^3 r = 0.$$
 (2.5)

In (2.5), v_{xc} is the exchange-correlation potential defined as [28]:

$$v_{xc}[\rho] = \frac{\delta E_{xc}}{\delta \rho} \tag{2.6}$$

¹This is the most cited solid state physics paper ever

The kinetic energy can be expressed as:

$$T_0[\rho] = -\frac{1}{2} \sum_{i} \int \psi_i^* \nabla^2 \psi_i d^3 r.$$
 (2.7)

Combining with the auxiliary charge density

$$\rho(\mathbf{r}) = \sum_{i}^{N} |\psi(\mathbf{r})|^{2}, \qquad (2.8)$$

we can solve (2.5) by solving the single particle Schrodinger equation given by [28]:

$$\left(-\frac{1}{2}\nabla^2 + v^{KS}[\rho]\right)\psi_i(\mathbf{r}) = \epsilon_i\psi_i(\mathbf{r}). \tag{2.9}$$

In 2.9 the term $v^{KS}[\rho]$ stands for the effective Khon-Sham potential. Its general form is given by:

$$v^{KS} = v(\mathbf{r}) + \int \frac{\rho(\mathbf{r}')}{|\mathbf{r} - \mathbf{r}'|} d^3 r' + v_{xc}(\rho), \qquad (2.10)$$

It is worth noting the KS potential depends on the charge density, as well as the charge density will depend on the v^{KS} . Therefore the Kohn-Sham equation is solved Self-consistently. A schematic illustration of the method is shown in Fig.2.5.

In principle, DFT is an exact theory. In practice, it is an approximation, since the exact exchange-correlation energy is not exactly evaluated. Two of the main approaches are the Local Density Approximation (LDA) and the Generalized Gradient Approximation (GGA). While LDA takes into account only the charge

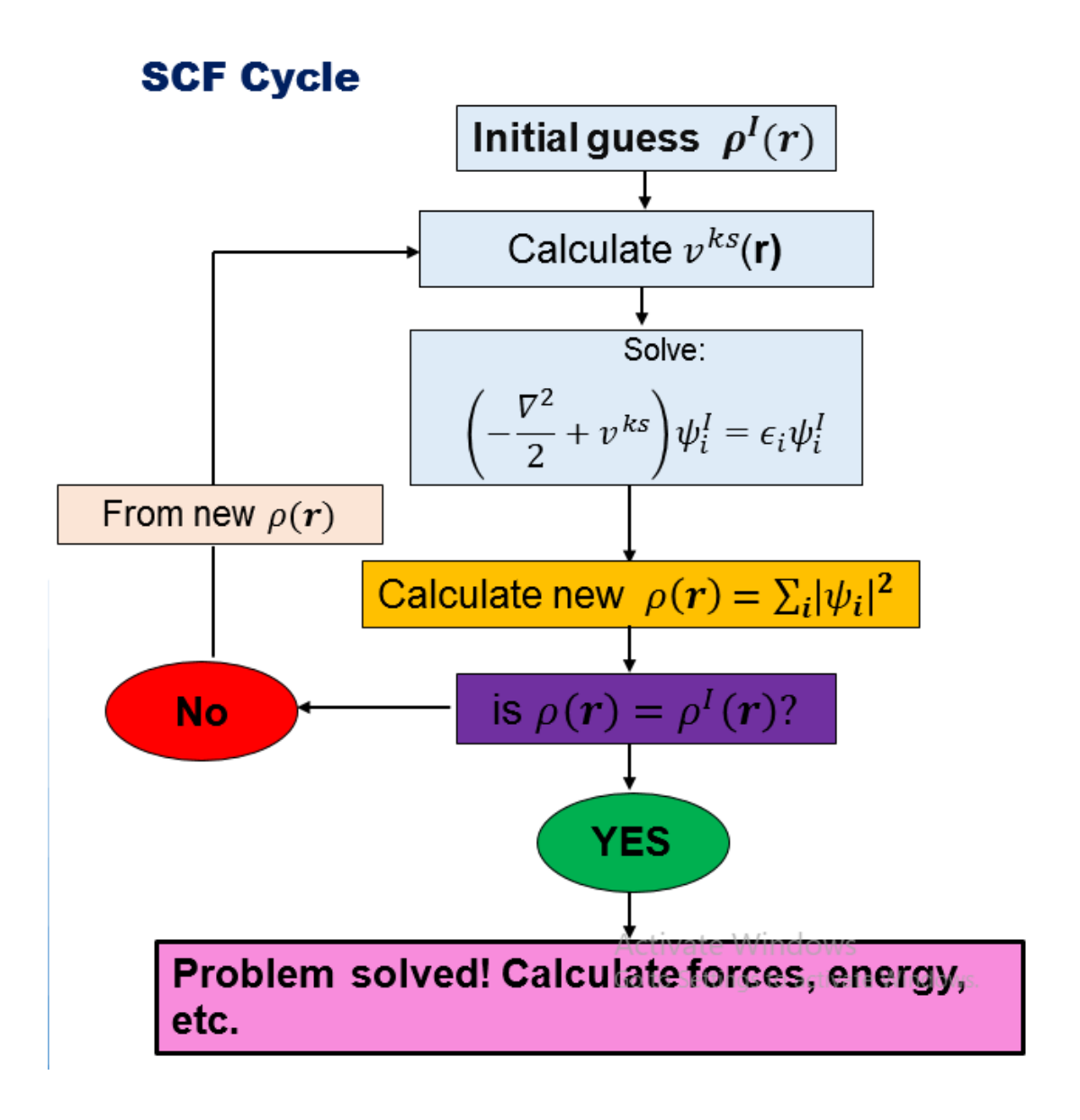


Figure 2.5: Illustration of the Self-Consistent Cycle.

density, the GGA methodology computes the gradient of the charge density following the description provided by Perdew, Burke, and Erzenhorf (PBE) [29]. Overall, both methods are well suitable for describing the geometric properties such as Lattice parameter, strain, bulk Modulus, etc [30]. However they are limited in providing an accurate description of the electronic structure, especially the band gap, since they do not take into account the self energy due to electron-

electron interaction, which turns the band gap calculations derived from these approximations underestimated [30].

From the converged electronic density based on GGA or LDA approximations, one can mixing it with a Hartree-Fock description of the Exchange-correlation energy, i.e. [31]

$$E_{xc}^{PBE-\alpha} = E_{xc}^{GGA} + \alpha (E_x^{HF} - E_x^{GGA}). \tag{2.11}$$

In Eq. 2.11, the parameter α represents the fraction of exact Hartree–Fock exchange included within the exchange-correlation functional. Typically, setting $\alpha = 0$ corresponds to the pure generalized gradient approximation (GGA) approach known as PBE, whereas the inclusion of exact exchange ($\alpha = 0.25$ by default) defines the hybrid functional known as PBE0. Alternative hybrid functionals, such as the HSE06 approach, incorporate a screened Coulomb potential to improve computational efficiency and better describe short-range exchange interactions [32]. Beyond hybrid DFT methods, many-body perturbation theories such as the GW approximation provide even more accurate predictions of electronic structure properties, although at a considerably higher computational cost [33]. In this thesis, we predominantly employ the standard PBE approximation due to its well-established accuracy and computational efficiency. Nevertheless, in the second paper, we utilized the hybrid PBE0 functional to compute optical properties within the framework of the Random Phase Approximation (RPA). Details on the $PBE - \alpha$ is provided in the Appendix B. All the calculations were performed using the Quantum Espresso open source package [34].

Chapter 3

ZnS zinc blende investigated by

LEED, XPS, and DFT

3.1 Motivation and challenges

The increasing demand for sustainable energy and efficient photocatalytic materials has placed wide-bandgap semiconductors like ZnS at the forefront of research into next-generation optoelectronic and catalytic technologies. Zinc sulfide is particularly attractive due to its low toxicity, earth abundance, and promising photocatalytic properties. However, the industrial application of ZnS remains limited, mainly due to its poor conductivity and large band gap — characteristics that hinder charge transport and light absorption in the visible range. These technological limitations have motivated intensive efforts to engineer ZnS properties at both bulk and surface level. In a solid state physics perspective,

there are some issues that turn detailed investigations on ZnS surfaces a tough task. In particular, the poor conductivity that hinder some usual surface science investigation like XPS and LEED due to the strong charging effect in these systems.

In this sense, defect engineering is one of the main topics widely explored. It has been shown that depending on the degree of impurities, at a bulk level, either intrinsic or extrinsic doping can alter the semiconducting nature (n-type or p-type), reduce the gap, and increase the range of light absorption response [35, 36]. This last topic will be explored in the next chapter. Here we are gonna focus on the electronic point of view. In this perspective, both intrisic (native defects) and extrinsic (substitutional impurities) are suitable strategies to introduce states into the forbidden zone, which might increase the number os major carries and thus enhance the overall conductivity of the system.

Of particular interest of ZnS surface features are their polarity. Both planes ZnS (001) and (111) are polar structures. Of particular interest in this thesis, ZnS (001) surfaces are Tasker type III, which are expected to undergo crystal-lographic reconstruction according to the degree of defects (cationic or anionic) on the surface [37]. Fig.3.1 illustrate the ZnS (001) surface explored in this chapter. In Polar binary semiconductors as ZnS, part of the anions species moves outward to the surface, while the cations relax inward to the surface. Although this results is well-known, the final pattern resulted from that mechanism was not accessed before, since LEED experiments were not yet achievable on polar ZnS surfaces due to charging effects.

The mechanism behind the influence of thermodynamic conditions and point defects on ZnS surface would be individually disclosed by working with

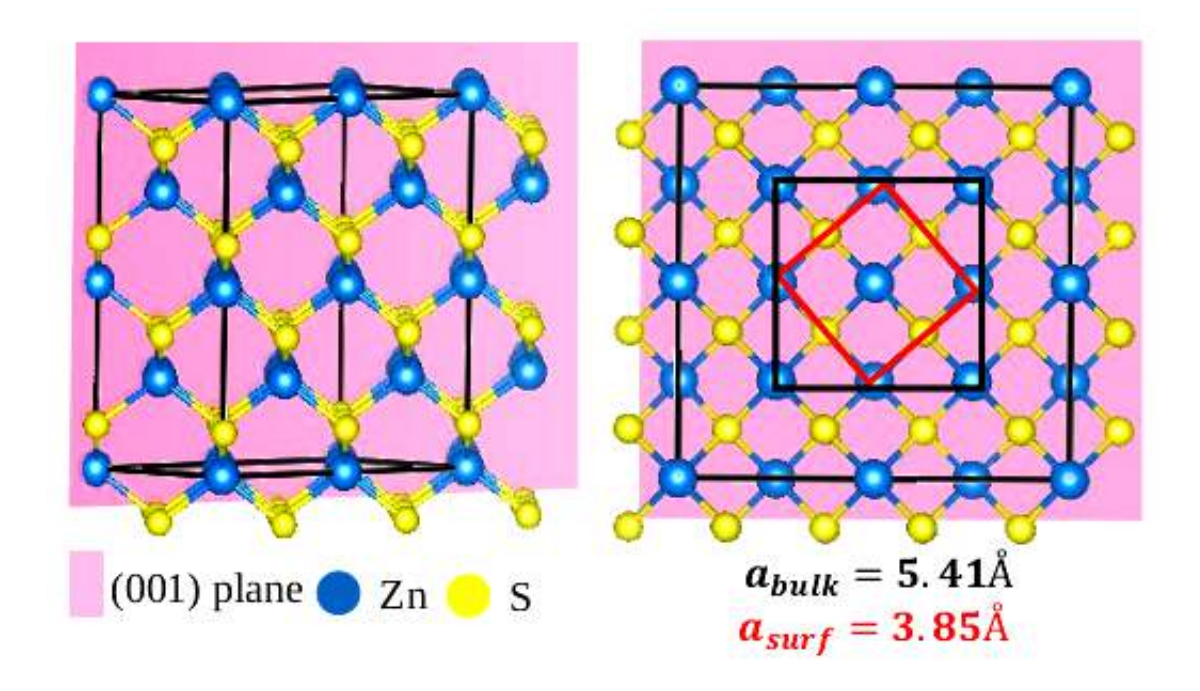


Figure 3.1: Schematic side (left) and top (right) view of the ZnS (001)structure. Blue and yellow balls denote zinc and sulfur atoms, respectively. The (001) plane is marked in pink. The bulk and surface lattice parameter are highlighted by a black and red square, respectively

a high-purity single crystal and relating experimental results with theoretical calculations. Nevertheless, efforts in this direction were only applied to WZ-ZnS [15] systems and have not been explored yet for ZB ZnS surfaces. In this study, we investigate the surface structure of ZnS (001) single crystals by XPS, LEED, and DFT calculations. In our work, we aim to understand the role of preparation conditions of the ZnS (001) surface on its structure and electronic properties. Our findings reveal that at ultra-high vacuum conditions, an S-rich - reconstructed surface structure characterized by missing rows of zinc cations is formed. Please refer to full paper - [38] - for further details not discussed in this chapter.

3.2 Results and discussion

Identifying surface chemical species

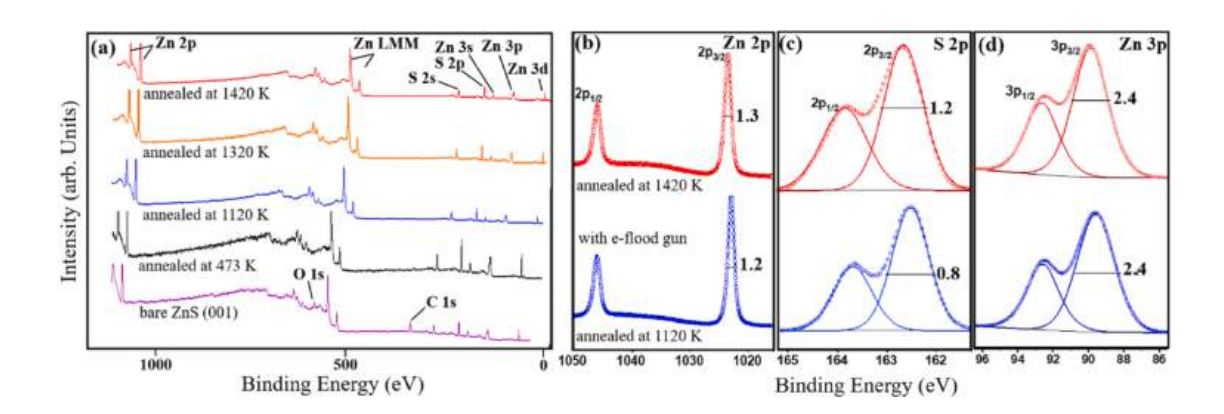


Figure 3.2: (a) XPS survey spectra of clean ZnS (001) pristine, ZnS (001) with flood gun and ZnS (001) after a high surface treatment with annealing temperature at 1420 K (black, blue and red curves,respectively). (b) Zn 2p (c) S 2p and (d) Zn 3p core-level spectra. All the spectras were acquired at room temperature.

XPS measurements at normal emission geometry of the ZnS (001) surface at different preparation conditions are depicted in Fig. 3.2. In Fig. 3.2 XPS survey spectra as collected are shown for the bare sample surface as-loaded in the UHV chamber and compared to samples prepared at different UHV annealing temperatures. The XPS survey spectra shown in Fig. 3.2a are shown as recorded without e-flood gun assistance. The bare sample (purple) displays the main core level peaks located at 1085.6 eV, 562 eV, and 229.2 eV, which corresponds to Zn 2p, Zn LMM, and S 2p, respectively, as well as the presence of oxygen and adventitious carbon species on the surface. These binding energies are significantly shifted towards higher positions than their typical values reported in the literature [39, 40]. This binding energy shift is connected to the insulator nature of the ZnS surface, which implies a low electron-hole recombination rate, resulting in a strong electrostatic interaction between the ejected photoelectron and the positive charge accumulated at the surface. This phenomenon is responsible for the decrease of the photo-electron kinetic energies, thereby leading the peaks to appear at larger binding energy values.

Sample surface cleaning following several cycles of Ar^+ sputtering and gentle UHV annealing at 473 K (Fig. 3.2a in black) resulted in an apparently clean surface, although significant charging is still observed. In this case, Zn 2p, Zn LMM, and S 2p peaks are identified at 1077.3 eV, 554 eV, and 220.2 eV, respectively. Further sample treatment by additional cycles of Ar^+ sputtering and annealing in UHV up to 1420 K promotes an appreciable reduction of sample charging. At the UHV annealing conditions displayed in Fig. 3.2a, the Zn $2p_{3/2}$ component binding energy position decreases as a function of the temperature increase: Starting at 1085.6 eV (bare sample) reducing to 1077.3 eV (annealed at 473 K), 1030.6 eV (annealed at 1120 K), 1024 eV (annealed at 1320 K) and

ending at 1022.6 eV (annealed at 1420 K). These binding energy values correspond to an energy shift of about 63.6, 55.3, 12.6, 2 eV, and 0.6 eV, as compared to the expected Zn $2p_{3/2}$ component position at 1022 eV [44,53]. Although Zn $2p_{3/2}$ component binding energy may display appreciable differences depending on the Zn-content system, these shift values are equivalent if we take Zn 3s peak position at 140.5 eV as a reference. This choice is justified because the Zn 3s binding energy does not vary significantly for several zinc-based materials such as sulfides, oxides, and sulfates [41, 42]. Given the good agreement of the XPS binding energy peak positions measured for samples annealed at 1420 K in UHV with the expected values reported in the literature for ZnS, it is believed that most sample charging could be avoided at such preparation conditions.

Further XPS characterization of the sample surface changes promoted by the annealing temperature is explored in Fig. 3.2b, c, and 3.2d. In this, we compare the main Zn 2p, S 2p, and Zn 3p core-level peaks obtained from the sample annealed at 1420 K (in red) to the 1120 K one with the assistance of the e-flood gun (in blue). Noteworthy, the XPS spectra obtained for the samples annealed below 1420 K display charging-related features, which leads to peak intensity modification and line shape tail on the low binding energy side [22]. To tackle this issue, we have performed XPS measurements using an e-flood gun under the conditions described in the experimental section. The appropriate adjustment of the e-flood gun was useful in determining the shape and relative intensity of Zn and S peaks as a function of the annealing temperature. As a result, the e-flood gun compensated high-resolution spectra shown in Fig. 1b, c, and 1d (in blue colored) display peaks arising closer to their characteristic binding energies, namely Zn $2p_{3/2}$ at 1022 eV, S $2p_{3/2}$ at 162.3 eV, and Zn $3p_{3/2}$ at 89.4 eV.

XPS spectra analysis of Fig. 3.2b indicates the characteristic spin-orbit components with Zn peaking at 1022.6 eV and 1022 eV for 1420 K (in red) and 1120 K (in blue) annealed samples, respectively. In both samples, the spin-orbit doublet separation appears close to 23 eV, a typical value reported in the literature for zinc species bonded to sulfur anions in ZnS compounds [40]. Similarly, S 2p and Zn 3p regions are presented in Fig. 3.2c and d, respectively. The XPS spectrum acquired for the sample prepared at 1120 K using the e-flood gun displays the S $2p_{3/2}$ and S $2p_{1/2}$ components at 163.4 eV and 162.2 eV and for the Zn $2p_{3/2}$ and Zn $2p_{1/2}$ components at 90 eV and 89.4 eV,respectively. For samples prepared at 1420 K, the S $2p_{1/2}$ and S $2p_{3/2}$ component lies at 164 eV and 162.8 eV, and for the Zn $3p_{3/2}$ and Zn $3p_{1/2}$ components at 90.6 eV and 90 eV , respectively. In general, these binding energy values are also characteristic of sulfur species in the ZnS structure [39]. At the sample preparation conditions explored in our work, the spin-orbit components separation and their intensity ratio are not dependent on the annealing temperature. Yet, it is worth mentioning that the peak fitting analysis displayed in Fig. 3.2c suggests a subtle FWHM broadening for the S $2p_{3/2}$ component, varying from 0.8 to 1.2 eV, as a function of the annealing temperature. In general, this peak broadening may suggest that sulfur anions may be subject to distinct chemical environments/structures, as will be explored in the following sections.

Fig. 3.3a and b shows the relative Zn and S atomic concentration analysis as a function of annealing temperature and surface-sensitive (different photoemission take-off geometries) XPS measurements. In Fig. 3.3a, we observe that samples prepared at different annealing temperatures result in changes in the relative atomic concentration, indicating that as the temperature increases, the S 2p/Zn 3p ratio becomes larger as compared to the bare surface as-loaded in

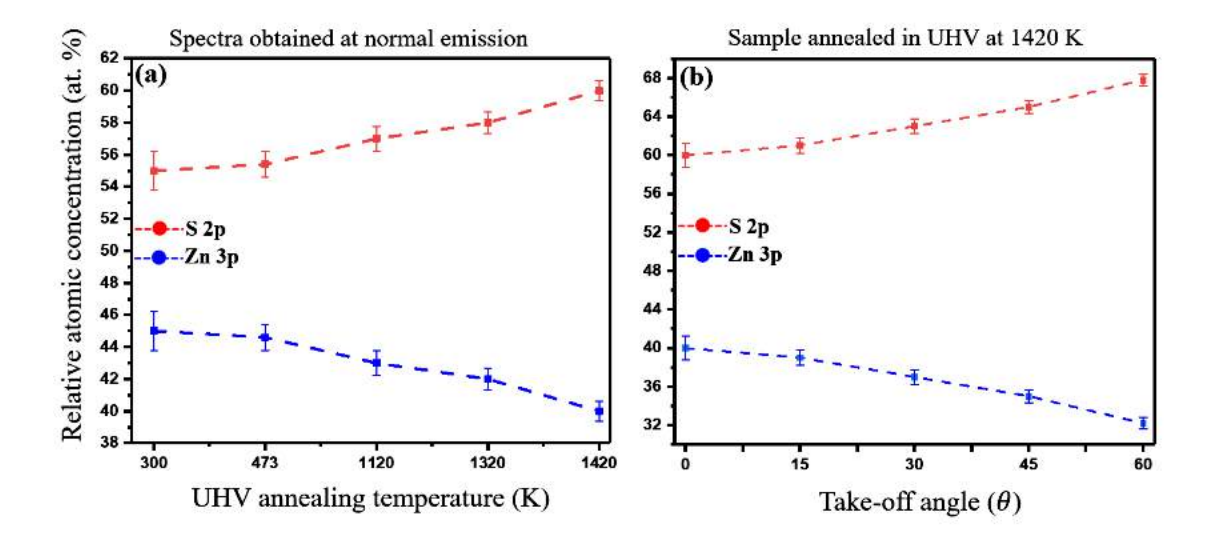


Figure 3.3: Quantification of the relative atomic concentration based on the S 2p and Zn 3p peak regions as a function of (a) sample UHV annealing temperatures at normal photoemission geometry and (b) the photoemission take-off angle geometry for a fixed temperature (at 1420 K). In (a) the S 2p and Zn 3p regions were collected with the assistance of an e-flood gun at the conditions described in the experimental section, except for the 1420 K annealed sample. In (b) the S 2p and Zn 3p regions were analyzed as collected.

UHV. It is worth mentioning in Fig. 3.3a that although the sulfur-zinc ratio at 300 K is quantified from surfaces contaminated by adventitious oxygen and carbon species (Fig. 3.2a in purple), its magnitude may only vary marginally and offset the actual ratio, which would not change the observed trend. The direct comparison of the bare sample to the 1420 K UHV annealed one displays a relative sulfur-to-zinc ratio increase of about 5 %, suggesting an apparent sulfur enrichment at the surface. In Fig. 3.3b, the XPS characterization of the 1420 K annealed samples obtained at different take-off geometries confirms the surface region sulfur enrichment at the expense of zinc species. Importantly, these relative concentration changes as a function of the annealing temperature point

out that vacancies are introduced in the sample surface, giving rise to a larger conductivity than the bare sample. These findings agree with the generally accepted mechanism expected to take place on polar surfaces like the ZnS (001) in which the surface electrostatic stability is achieved through the formation of intrinsic defects and/or surface reconstruction [43]. For this reason, we have attempted to characterize the ZnS (001) surface annealed at 1420 K using scanning tunneling microscopy, yet poor sample conductivity has not allowed sufficiently stable tunneling conditions. Alternatively, low energy electron diffraction (LEED) measurements were employed to characterize its surface structure as follows.

Surface Structure characterization

In Fig. 3.4 additional information about the ZnS surface structure is obtained by LEED. We experienced significant difficulties related to sample charging when attempting to observe LEED patterns. Depending on the surface preparation conditions, the degree of charging leads to non-observed diffraction spots, ill-defined spots, and distorted patterns. The most effective method to reduce charging was to work with a small sample size in which the fixing metal plate was relatively close to the analyzed area. Under these conditions, excessive charging could be partially avoided. Yet, we were restricted to only exploring the LEED patterns obtained, keeping the sample current as low as possible and using a minimum e-beam primary energy of 65 eV.

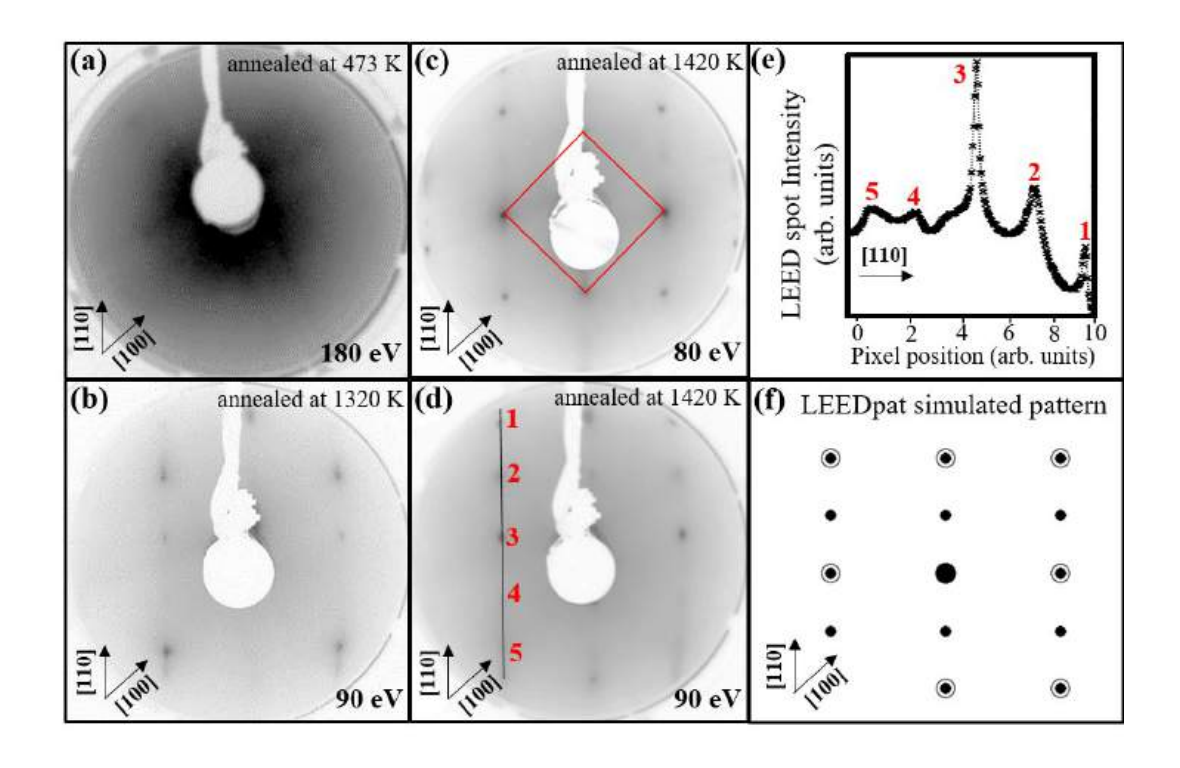


Figure 3.4: LEED patterns and analysis of the ZnS (001) surface structure. In (a), (b), and (c)/(d) are shown LEED patterns obtained for samples prepared at annealing temperatures of 473 K, 1320 K, and 1420 K, respectively. In (e), the LEED intensity line profile is shown for the black line indicated/labeled in (d). In (f) is depicted the LEEDpat simulated pattern for the proposed (1x2) reconstructed surface structure. The double-circled points denote the ideal (1×1) arrangement, while the reconstruction fingerprint is provided by the two extra points (in black) between each line.All LEED pattern photographs were adjusted to enhance their contrast for clarity

Fig. 3.4a-d show the LEED patterns obtained for the ZnS surface prepared in UHV at 473 K, 1320 K, and 1420 K annealing temperatures. Comparing the LEED patterns, we note that as the annealing temperature increases, the initially disordered/insulating sample surface characterized by the intense background pattern (Fig. 3a) is partially converted to intensified and better-defined diffrac-

tion spots (see Fig. 3.4b, c, and 3.4d). The LEED patterns observed for 1320 K (Figs. 3b) and 1420 K (Fig. 3.4c and d) UHV annealed sample display diffuse and asymmetric diffraction spots when comparing left/right and upper/down maxima. These LEED pattern asymmetries and distortions are related to persistent poor sample surface conductivity. To assist our sample diffraction pattern analysis, LEED patterns were obtained for a reference clean Ag (001) single crystal surface at the same position with the LEED screen and e-beam energy of the ZnS surface. The reference LEED measurement (not shown here) displays a square pattern as expected of the Ag (001). This reference measurement was used, considering the standard lattice constant for Ag of 0.298 nm, to identify and estimate the actual sample diffraction pattern. By this means, we could identify in Fig. 3.4c the corresponding diffraction maxima LEED screen position expected by the (1x1) ZnS (001) surface, as highlighted by the red-colored square pattern. Further LEED analysis were performed for the samples prepared at 1420 K annealing temperature shown in Fig. 3.4d. In Fig. 3.4e, surface diffraction spots are readily identified by measuring the LEED intensity line profile indicated by the black line in Fig. 3d. The diffraction spots labeled in Fig. 3d and e are organized in rows along the [110] single-crystal surface direction, separated by an approximated half-distance of the nearby row, which is compatible with the formation of a (1x2) surface reconstruction. Fig. 3.4f shows the LEED diffraction pattern simulation obtained using the LEEDpat software package to assist further with the identified (1x2) reconstructed surface structure proposal [44].

Chapter 4

Formation mechanism, stability and role of zinc and sulfur vacancies on the electronic properties and optical response of ZnS

Low-cost and highly stable optical devices are some of the industrial demands regarding optical material's candidates. Notably, it has been noted a seeking for new platforms with a broad range of optical response, suitable for applications such as multi-spectral images, smart windows, and modulators. Again, solid-state physics might pave the way toward new platforms in this field. As widely reported in recent years, defect engineering has been proven to be a useful tool to model the optical properties of several systems. Among

these systems, zinc sulfide-based architectures have been reported as potential candidates. Usually, these materials are responsive only in a minor range of the sunlight spectrum, most likely ranging from ultra ultraviolet-visible (UV-VIS) range. However, depending on the kind and level of impurity, one can broaden the optical absorption range, tuning to the infrared and visible range. In this work, we explore the role of point defects on ZnS, investigating its stability (n-type x p-type ZnS) and effect on the emission spectra, combining photoluminescence spectra and DFT calculations.

4.1 Point defects stability

In the theoretical point of view, the formation energy of defect D in a particular charge state q ($E_{form}(D^q)$) is a well-known strategy for describing the stability of point defects [45]. Given a particular chemical potential μ_e , it is evaluated as:

$$E_{form}(D^q) = E_{defect} - (E_{bare} + \mu_x) + q(\mu_e + VBM).$$
 (4.1)

In Eq.4.1, E_{defect} and E_{bare} are the system energy with and without defect, respectively, and VBM is the valence band maximum of the system. The parameter μ_x stands for the electronic chemical potential, usually spanning from the top of the valence band (pinned at zero) until the conduction band minimum. The term μ_x is the chemical potential of the added (removed) specie. This parameter is computed by taking into account that for a given system AB, its chemical potential μ_{AB} is limited to the sum of the individual chemical potential

 μ_A and μ_B , i.e:

$$\mu_{AB} \le \mu_A + \mu_B. \tag{4.2}$$

Therefore, for a particular A-rich scenario, one can evaluate the chemical potential μ_A by modeling the individual system A in an isolated box, computing its total energy $E_{tot}(A)$, since

$$\mu_A = E_{tot}(A). \tag{4.3}$$

Given Eq.4.2 and Eq.4.3, once computed the total energy of the system AB, i.e, $E_{tot}(AB)$, we can obtain μ_B :

$$\mu_B = E_{tot}(AB) - \mu_A. \tag{4.4}$$

By Handling all these ingredients, one can compute the formation energy as a function of the Fermi level. The particular μ_e position where the formation energy of a defect in the charge state q ($E^f(q)$) is equal to the defect in charge state q' ($E^f(q')$) is known as the defect-transition level $\epsilon(q/q')$, which can be represented as

$$\epsilon(q/q') = \frac{E^f(q) - E^f(q')}{q' - q}.\tag{4.5}$$

The stability of a doped system as a n or p-type material depends on the position of μ_e in which the transition level takes place. While transition level close to the VBM stands for p-type classifications, transition occurring near to the CBM results in an n-type configuration. All these aspects will be of particu-

lar interest to understand the stability of ZnS architectures, as discussed next in this chapter.

4.2 Photoluminescence mechanism: Basic principles and modeling

The Luminescence mechanism stands for an emission of a photon with a particular energy E' upon stimulation (thermal, electronic, photon). When the primary source of excitations are photons impining in the material with energy E, the emission of the photons are described as photoluminescence. In this scenario, an electron is promoted to a higher level, leaving a hole behind. After relaxation, that electron-hole pair can undergo either radiative (RR) or non-radiative (NR) recombination. While the first scenario results in an emission of a photon such that E' is equal to the difference between the levels enrolled in the process, the photon emission in the last mechanism is vanished. These process are illustrated in Fig.4.1.

In a general form, the luminesce efficiency η_r is a relative balance between those process, i.e

$$\eta_r = \frac{1}{1 + \tau_{RR}/\tau_{NR}}. (4.6)$$

The terms τ_{RR} and τ_{NR} regards radiative and non-radiative life-time, respectively. It is interesting to note that as long as $\tau_{RR} \to \infty$, the luminescence effi-

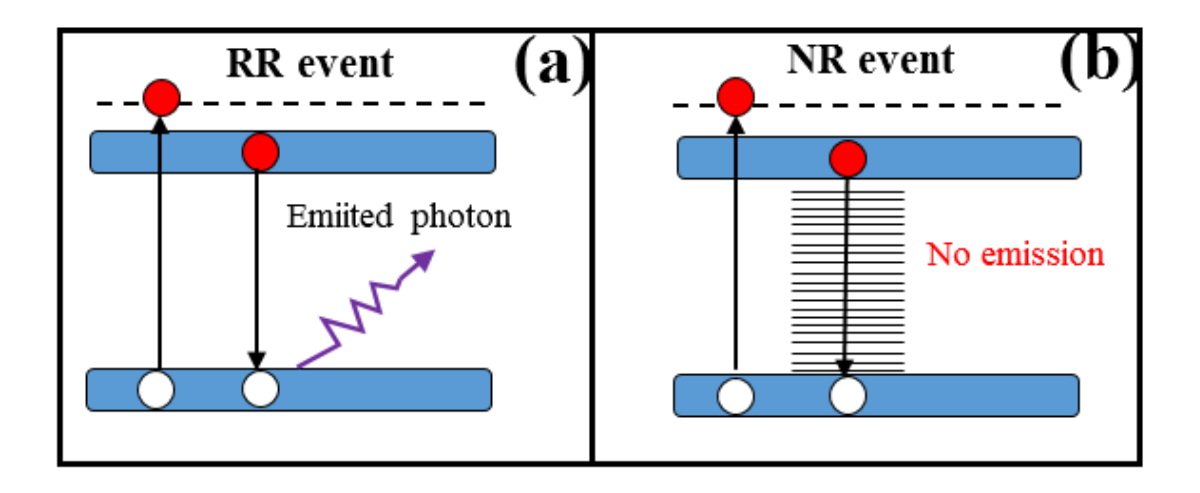


Figure 4.1: Radiative (a) and non-radiative (b) recombination process.

ciency achieves its maximum value. Typically, τ_{RR} is of the order of nanosecond, which is larger than τNR - usually in the range of femtoseconds.

As mentioned in the last chapter, point defects can introduce new levels into the forbidden zone. These levels can act as recombination centers, thus resulting in an emission that corresponds to the difference between the excited and impurity levels. These mid-gaps states are the driving force that allows for exciting the system even with a source whose energy is lower than the band gap. Usually, these new levels resembles atomic levels, hence their pictorial description might be explained in terms of discrete energy levels, as discussed later in this chapter.

In the theoretical point of view, one can gain insights from emission spectra of defect-free and defective systems by computing the Joint-Density of States (JDOS). It stands for the sum of transitions from the valence band (n) and the conduction band (n') states. Generally speaking, the JDOS computes the allowed transition through the entire volume of the lattice cell (Ω)according to

[34]

$$JDOS = \sum_{n} \sum_{n'} \frac{\Omega}{(2\pi)^3} \int d^3 \mathbf{k} \delta(E_{\mathbf{k},n'} - E_{\mathbf{k},n} - \hbar \omega) [f(E_{\mathbf{k},n}) - f(E_{\mathbf{k},n'})]. \tag{4.7}$$

The terms $E_{\mathbf{k},n'}$ and $E_{\mathbf{k},n'}$ denote the energy states in the conduction and valence band, respectively. The overall distribution of these states is computed by the function $f(E_{\mathbf{k},n})$ ($f(E_{\mathbf{k},n'})$). The delta function is implemented by Gaussian or Lorentzian function. Both options are dependent on the broadening parameter set up in the input file. As explained in the Quantum-Espresso documentation, in the sight of JDOS, the two cases are equivalent. In the next section we are gonna discuss in the details the role of intrisic defects on electronic and optical properties of zb-ZnS. Please refer to the full paper [46] for accessing further details not discussed in this chapter.

4.3 Results and Discussion

Experimental Resutls

4.3.1 XPS analysis

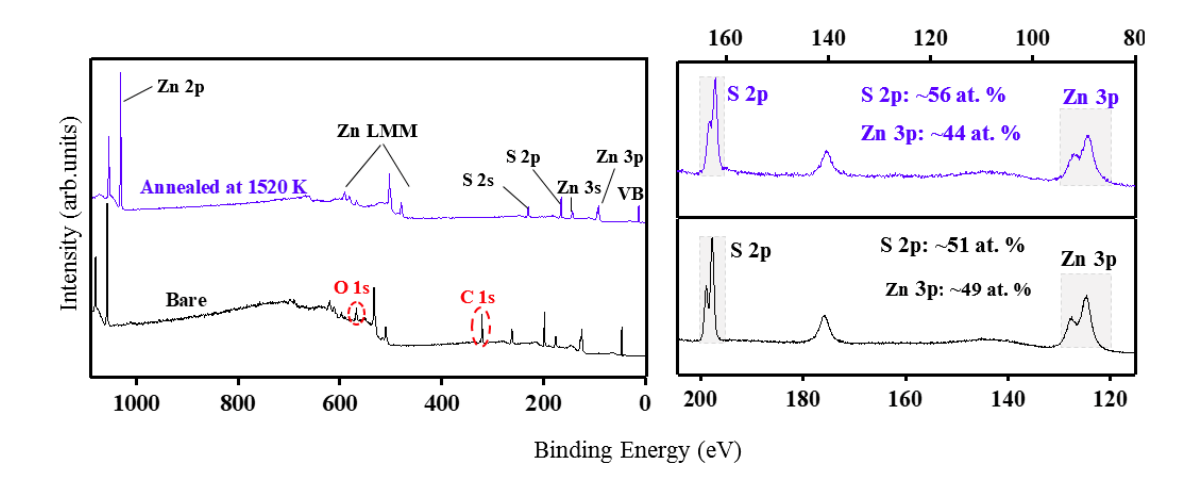


Figure 4.2: XPS spectra of bare and UHV annealed ZnS single crystal. (a) survey scan and (b) small region analysis spanning from S 2p to Zn 3p. All the spectra were acquired at room temperature and at normal emission.

Fig.4.2 shows the XPS spectra of the ZnS single crystal before and after insitu surface preparation. In Fig.4.2(a), the effect of the annealing temperature on the binding energy position of the ZnS main components is highlighted. In the bare sample scenario, that is,the sample measured as loaded, the XPS components appeared almost 35 eV offset from the expected positions. For instance, Zn 2p, C 1s, and S 2p are identified at 1058 eV, 320.8 eV, and 197.8 eV, while in the literature accepted values are 1022 eV, 284.8 eV and 161.8 eV, respectively [39]. These binding energy shifts are explained by the insulating nature of pristine

ZnS systems [40, 38]. The absence of an effective electron-hole recombination rate results in strong electrostatic charging in the sample, thus reducing the kinetic energy of the emitted photoelectrons. One effective strategy to mitigate this scenario is in-situ preparation at high annealing temperatures [38]. Indeed, several annealing cycles at 1520 K allowed for a shift toward lower binding energies, as shown in the blue survey spectrum in Fig.4.2(a). Here, Zn 2p and S 2p are located at 1022.8 eV and 161.8 eV, in good agreement with the binding energies of Zn atoms bound to S species in the Zn^{2+} - S^{2-} configuration. Contamination species like carbon or oxygen were not found because UHV annealing removes such initially adsorbed surface species. Additionally, as we recently reported, this procedure might induce defect formation in the system, increasing the number of majority carriers and suppressing the sample charging. In that case, the ZnS surface displayed a more conductive character, and the XPS components were identified at the expected binding energies [38]. To gain insights into the nature of the defects (cationic or anionic), the relative atomic concentration between S 2p and Zn 3p in the bare and UHV-annealed samples are shown in Fig.4.2(b). It is worth noting that the S 2p and Zn 3p photoelectrons are ejected from equivalent depths, and their relative sensitivity factors, following the *Scofield* table, are similar [47]. Therefore, the relative atomic concentrations obtained from these peaks are helpful in following the surface modifications occurring due to the sample UHV treatment. As discussed, prior in-situ treatment the binding energy shift of the main components is close to 35 eV. While for the bare sample the S 2p and Zn 3p components are found at 196 eV and 125 eV, respectively, these components after the UHV annealing at 1520 K are located at 161.8 eV and 90 eV. Although there is a large binding shift, it does not play a role in atomic species quantification. In this case, we can evaluate the relative atomic concentration of sulfur and zinc in each scenario without losing generality. While in the pristine scenario (insulating sample) an almost 1 : 1 ratio is found, the UHV annealed sample reveals an increase in the sulfur content by up to 5 at.% relative to zinc atoms. This finding suggests a sulfur-rich surface, which is attributed to the formation of a cation-defective system.

4.3.2 Electronic structure and Optical response analysis

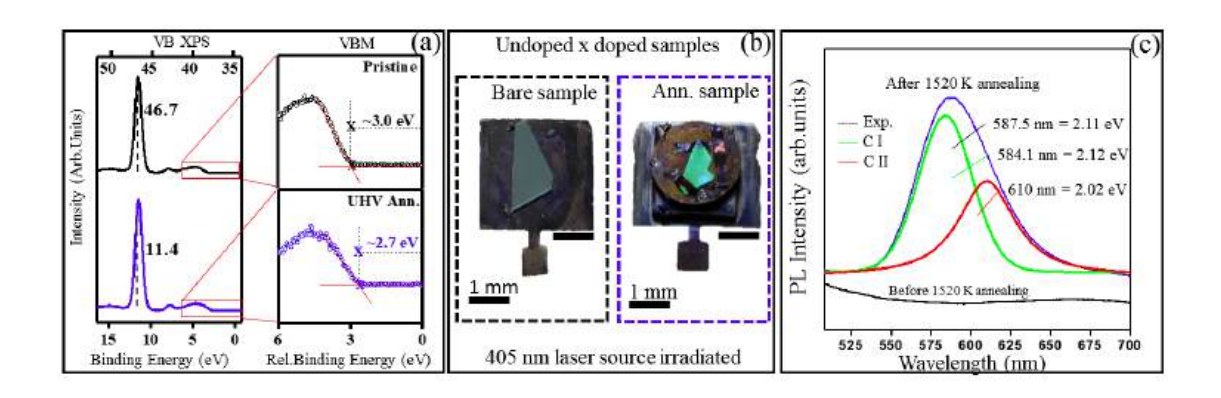


Figure 4.3: (a) Valence band XPS spectra of bare (top) and UHV annealed (bottom) ZnS single crystal; (b) Undoped and doped ZnS single crystal appearance upon laser irradiation. (c) Ex-situ PL spectrum before and after UHV annealing at 1520 K. The XPS spectra are shown as loaded. All the spectra were collected at room temperature.

More information regarding the role of cation defects in the electronic and optical responses of zinc blende ZnS is shown in Fig.4.3. In Fig.4.3(a) (left panel), the valence band spectra of bare and in-situ prepared at 1520 K ZnS are depicted. It should be noted the Zn 3d peak in the bare sample is significantly shifted. The typical binding energy in ZnS sample is close to 11.4 eV, while in this scenario it rises at 46.7 eV, configuring a B.E shift of 35.2 eV, compared to the expected value. The UHV annealed sample, on the other hand, does not re-

veal any binding energy shift, as depicted in the bottom of Fig.4.3(a) (left panel). This sample seems to be more conductive due to the removal of zinc atoms, as discussed later. In this scenario, the main component related to Zn 3d orbital is found at 11.4 eV, as expected.

More insights into the electronic structure were obtained comparing the valance band maximum (VBM) of both samples, as displayed in right panel of Fig.4.3(a). These measurements are regarding to the Fermi-level, which means they are reliable even for the bare sample, because the relative binding energy is considered. In this scenario, the VBM of the bare sample was found to be close to 3 eV, while the UHV annealed sample VBM displayed a slight shift toward low binding energy, with the VBM arising close to 2.7 eV, as noted in the top and bottom of the Fig.4.3(b) (right panel), respectively. This finding is a general trend for p-type semiconductors. In ZnS, the most likely way to obtain a ptype system is through the formation of either zinc vacancies or sulfur interstitials. However, only the former one would give rise to an S-rich surface, which seems to be the ZnS scenario after UHV treatment as discussed in Fig. 4.2(b). An interesting strategy to probe the nature of the semiconductor (n or p) is the laser-assisted XPS measurements, as recently reported[48]. Indeed, UV-laserassisted XPS is a well-known method to mitigate sample charging [49]. Due to the low wavelength, it can excite electrons near to the surface, which enhances the electron-hole recombination rate, hence mitigating the positive electrostatic field generated due to the photoelectron emission. This aspect is highlighted in Fig S2-(a), where the binding energy of the bare sample is almost corrected due to the incidence of a 405 nm laser source [49]. However, in the presence of doping (either native defects or substitutional impurities), two additional phenomena can be observed in laser-assisted XPS measurements: under-compensation (left-hand binding energy shift) and overcompensation (right-hand binding energy offset).

The direction is dependent on the nature of defects, with n-type and ptype standing for higher and lower binding energy shifts, respectively [48]. In our case, the VB band measurement of the UHV annealed sample is slightly shifted toward low binding energy, indicating the p-type nature of the system. However, a detailed investigation on this subject must be carefully considered because the total offset seems to be dependent on both wavelength and laser power, though it is beyond the scope of this work. Nonetheless, a quite interesting aspect to note – which is independent of those aforementioned parameters - is the ZnS color appearance under illumination of the 405 nm laser. If the bare ZnS does not reveal any color-like appearance (Fig 4.3(b) left panel), the annealed sample, on the other hand, displays a green color emission (Fig.4.3(b) right panel). In view of the wide band gap of ZnS (at about 3.6 eV), the visible emission observed in UHV annealed sample under a 405 nm (3.06 eV) irradiation might signal an optical response enhancement due to the formation of cation defects. This aspect was quantitatively explored by photoluminescence measurement performed ex-situ. To this end, the ZnS samples were transferred from the XPS UHV chamber to our PL experimental setup by exposing them to ambient conditions followed by immediate PL measurements. Fig. 4.3(c) shows the PL spectra obtained for the bare, and UHV annealed ZnS samples. Noticeably, the bare sample does not display any photoluminescence response in the visible range, as indicated by the black spectrum. In general, ZnS can exhibit a near band-edge emission in the UV range (around 3.6 eV) when excited with the appropriate light source, and its optical response could reportedly be modified by including transition and rare earth metal dopants [50, 51]. In our PL experimental setup, however, we can only excite the sample with 488 nm (2.54 eV), and investigation of the sample near band-edge emission is beyond the scope of this work. Yet, the PL response using our setup is helpful for identifying the sample's optical properties modifications promoted by the UHV annealing, as indicated by the blue spectrum.

In Fig.4.3(c), the UHV annealing results in an intense and broad peak located at approximately 587.5 nm (spectrum in blue). The PL peak analysis can be performed employing two components, labeled as C1 (green line) and C2 (red line) located at 584 nm and 610 nm, respectively. In our previous study on the ZnS (001) surface, it was identified at similar UHV annealing conditions the formation of a stable zinc-terminated surface in which relative changes in the S/Zn atomic concentration were linked to the improvement of the surface conductivity due to the potential formation of Zn vacancies [38]. However, the observed changes in the ZnS sample color appearance (Fig.4.3(b) right panel) and the development of the photoluminescence response shown in Fig.4.3(c) suggest that the formation of the Zn vacancies may indeed extend to the ZnS bulk counterpart and be connected to the PL response. In general, cation defects such as zinc vacancies might yield few states just above the VBM. These states can behave like shallow acceptors, trapping electrons and promoting the recombination process, which gives rise to new emission lines via radioactive recombination [52]. To rationalize these experimental findings, in the following paragraphs, we have explored through theoretical calculations the stability and electronic properties modification related to the formation of Zn and S vacancies in the ZnS bulk.

Theoretical Results

4.3.3 Point defect stability and electronic structure

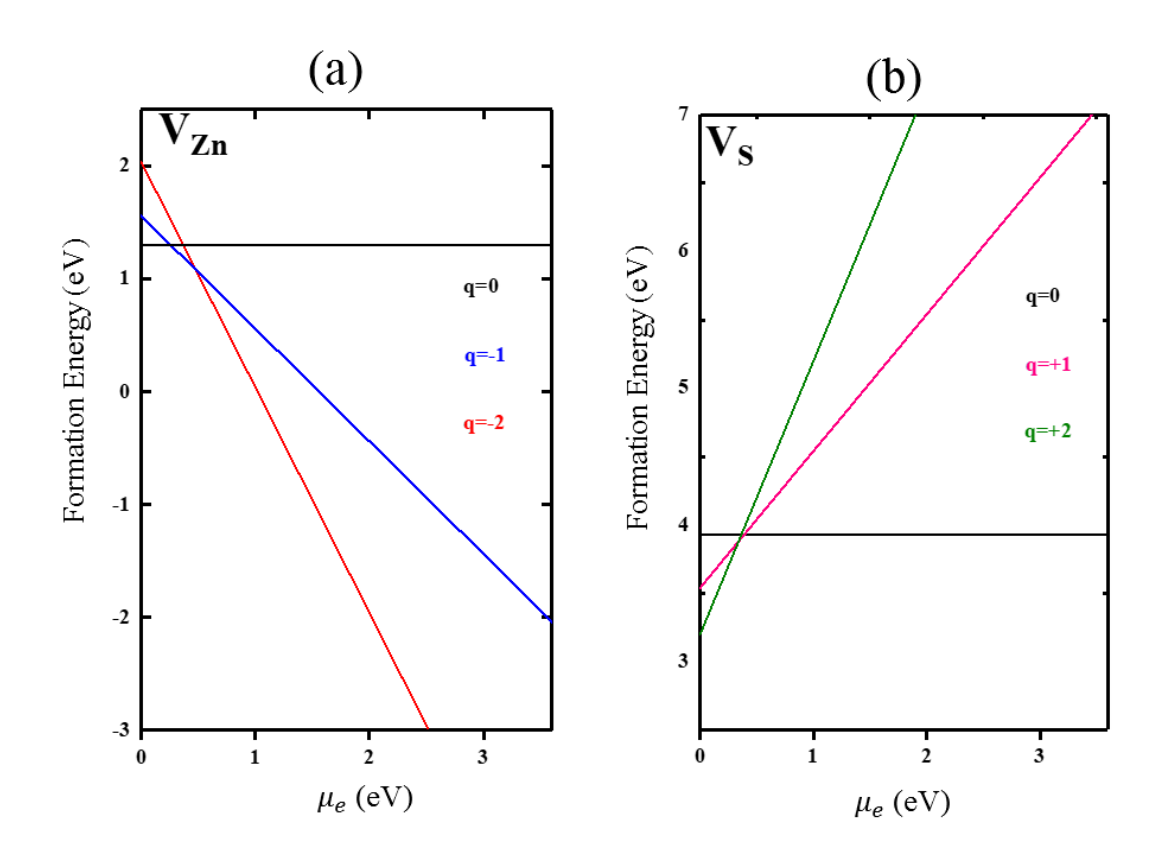


Figure 4.4: Formation Energy of (a) Zinc and (b) Sulfur vacancy as a function of the electronic chemical potential in an S-rich scenario.

The formation energy of defect D in a particular charge state q ($E_{form}(D^q)$) is a well-known strategy for describing the stability of point defects [45]. Considering the different charge states (q=-2,-1,0,1,2) for zinc and sulfur vacancy in an S-rich scenario we computed the formation energy (See SI) as a function of the electronic chemical potential μ_e as depicted in Fig. 4.4. In the neutral defect picture (i.e, q=0), zinc vacancy is more stable than sulfur vacancy ($E_{form}(V_{Zn}^0=1.3~eV)$), $E_{form}(V_S^0=3.9~eV)$). In addition, With μ_e pinned at

the top of valence band, we obtained $E_{form}(V_{Zn}^{-1}) = 1.56 \ eV$, $E_{form}(V_{Zn}^{-2}) = 2.04 \ eV$, $E_{form}(V_S^{+1}) = 3.54 \ eV$, $E_{form}(V_S^{+2}) = 3.20 \ eV$, according to Fig.4.5(a) and Fig.4.5(b), respectively. These findings are well-aligned with the general trend previously reported [53], which shows that charged zinc vacancies are more stable than charged sulfur vacancies. Furthermore, in this same scenario (μ_e pinned at the top of the valence band), the formation energy of charged zinc vacancy, especially the $E_{form}(V_{Zn}^{-1})$, is close to that of neutral zinc defects, which suggests that both neutral and charged cation defects are equally stable on ZnS and might coexist. On the other hand, according to our calculations, it is expected that if sulfur vacancies are formed on ZnS, it should stay in the charge state +2. Overall, the cation-defect ZnS is the most energetically favorable configuration in our system

An interesting parameter to investigate the nature of the stability (n-type or p-type) in the V_{Zn} -ZnS picture is the transition $\epsilon(q/q')$ highlighted in Fig. 4.4(a)-(b) by the crossing of each line. This parameter computes the particular E_{fermi} value where a transition from a defect in the charge q to q' takes place [45]. Zinc vacancy behaves as an acceptor, thus decreasing in energy as μ_e increases. According to the formation energy calculations, all the possible transition states $-\epsilon(-2/0)$, $\epsilon(-1/0)$, and $\epsilon(-2/-1)$ - occur slightly above the VBM. This finding illustrates that zinc vacancies in an S-rich (Zn-deficient) ZnS scenario behave as shallow-acceptors and are indeed stable as a p-type configuration.

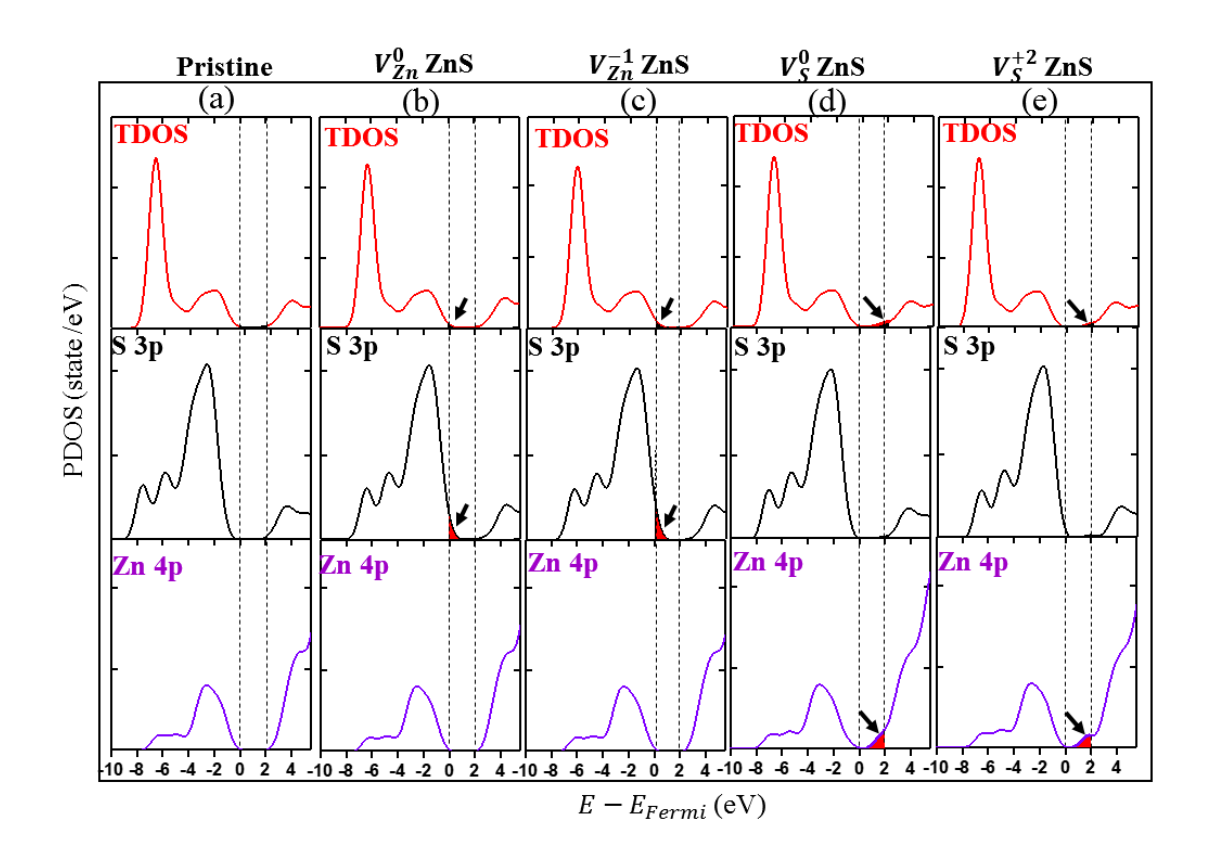


Figure 4.5: Projected Density of states of (a) pristine, (b) V_{Zn}^0 , (c) V_{Zn}^{-1} , (d) V_S^0 and (e) V_S^{+2} doped ZnS.The VBM was shifted to 0 eV for clarity.

4.3.4 Electronic Structure Analysis

Fig.4.5 shows the projected density of states of pristine ZnS and ZnS with vacancies. All the structures were calculated taking into account spin-polarization. In this sense, Fig.4.5 shows spin-up projected density of states of such structures. The calculated band gap of the pristine ZnS is 2.2 eV, which is an underestimated value as expected from calculations through PBE-GGA methodology [54]. Regarding the total density of states of each system, we found similar characteristics. Firstly, the Zn 3d states dominate the portion far from the valence band. The valence band is primarily composed of S 3p states, while the con-

duction band is mainly formed by Zn 4p and unfilled S 3p states. The main difference between defect-free and defective ZnS is the appearance of a few states inside the gap, indicated by the black arrow in Fig.4.5(b)-(e). For instance, there is a rise of a few states slightly above the Fermi-level after the formation of a zinc vacancy (Fig.4.5(b)-(c)). This finding is attributed to the decrease in the coordination number of S atoms due to the removal of zinc species, which promotes new S 3p-like states above the Fermi level, as highlighted by the filled red area in Fig.4.5(b)-(c) (middle plot). In addition, it tailors the gap to 2 eV. Although the aforementioned band gap underestimation through PBE-GGA calculations, this trend might indicate an electronic response improvement due to the formation of cation defects. The difference between neutral (Fig.4.5(b)) and charged (Fig.4.5 (c)) cation-doped ZnS is the density of such S 3p-like states arising inside the forbidden zone, which seems higher in the case of charged zinc vacancy. Overall, both structures could explain the enhancement of the electronic and optical response, as pointed out from XPS and PL experiments. On the other hand, the formation of sulfur vacancy gives rise to a few states slightly below the conduction band minimum, as revealed in Fig.4.5(d)-(e). The decrease of the Zn coordination due to the removal of sulfur results in some Zn 4p-like states, highlighted by the filled red area in Fig.4.5(d)-(e) (bottom panel). However, we did not observe a band gap reduction in either scenario (neutral or charged sulfur vacancy), indicating sulfur vacancies do not significantly improve the electronic response of the system. This finding might be attributed to the doping concentration limit. In general, sulfur vacancies in zinc blende ZnS are predicted to play a role in electronic and optical properties only at high defect concentration (higher than 25%) [12]. We maintained the doping below 5 %, making sulfur vacancy unlikely to explain our experimental findings. Based on our theoretical calculations, only neutral and charged zinc vacancy aligns well with the experimental results, particularly regarding the enhancement of the electronic and optical response and the p-type nature of the system. Therefore, we next focus exclusively on these structures to evaluate the optical properties of doped ZnS from a theoretical perspective.

4.3.5 Optical properties calculations

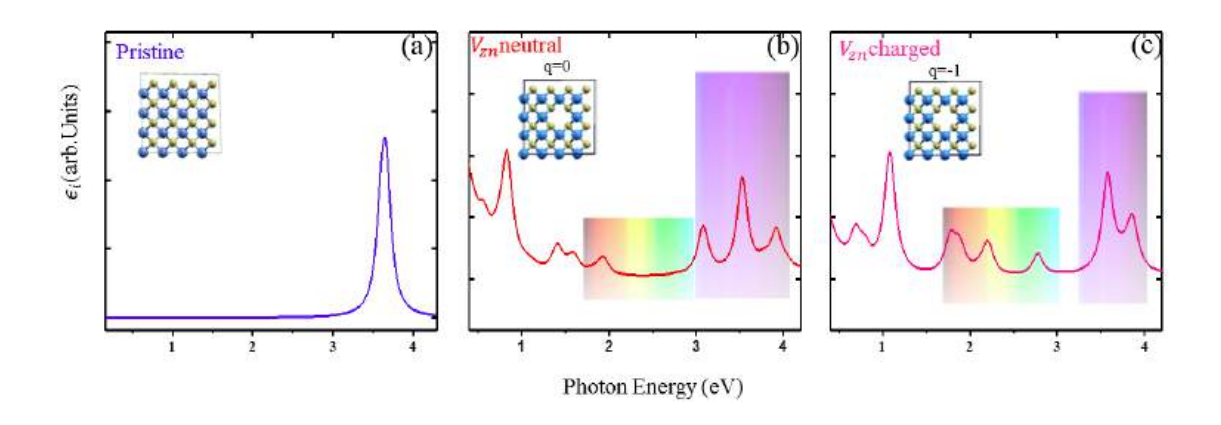


Figure 4.6: Theoretical absorption spectra of of (a) pristine, (b) neutral V_{Zn} and (c) charged V_{Zn} ZnS

A broad optical absorption range is a key prerequisite for a material to be considered a potential candidate for photocatalysis and optoelectronic devices applications. In this sense, Fig.4.6 compares the optical absorption of ZnS in three particular scenarios: pristine, neutral p-doped, and charged p-doped ZnS. In the first case, the only observed peak was the absorption at 3.6 eV, as shown in Fig.4.6(a). This peak corresponds to incident photons with energies matching the ZnS band gap. This result is in good agreement with the experimental band gap of ZnS, as expected, given that all the optical property calculations were performed using $PBE - \alpha$ hybrid-functional, with $\alpha = 0.27$ chosen to fit

the experimental band gap value. Conversely, due to the removal of a Zn atom from the pristine ZnS structure, several new absorption peaks were observed. In Fig.4.6(b), high absorption peaks at 0.8 eV (infrared region (IR)), 3.2 eV, and 3.6 eV (both in the ultraviolet (UV) range) are shown. The higher intensity of these components indicates that the neutral p-doped ZnS could readily absorb photons with such energies. In addition, the lower intensity absorption peaks are of particular interest, especially the component at 1.8 eV, corresponding to visible range absorption. This result can be addressed to the formation of a p-type ZnS, highlighting the role of zinc vacancies in enhancing the optical absorption. This improvement was experimentally observed through the green-like emission upon excitation with a 405 nm laser source, as shown in Fig.4.3(b). It is worth noting that before emission, the sample must absorb the incoming photons from the laser source. This step requires an absorption level close to 3.06 eV. In view of the new absorption peak at 3.2 eV in the V_{Zn}^0 -ZnS, this experimental finding might be attributed to the formation of neutral zinc vacancies. On the other hand, the neutral zinc defect does not match the results. Once PL first implies the absorption of photons with a particular source energy, a state at 2.54 eV in the absorption spectra is required in our experiments. However, changing the charge state of the system to q = -1, besides the new components observed in the neutral scenario, a component at 2.7 eV is found as revealed in Fig.4.6(c), in good agreement with the experimental prerequisite. The charged p-type ZnS also displays absorption peaks in a broad range, from IR (0.7 eV, 1.08 eV), visible (VIS) (1.8 eV, 2.2 eV, and 2.7 eV), and UV interval (3.6 eV and 3.8 eV). It is worth noting that in the dipole approximation we evaluate the imaginary part of the dielectric function computing direct inter-band transitions by a summation over several empty states, neglecting any many-body effects. Therefore, slight energy differences can occur, as well as a loss of information, as widely discussed [55, 56]. However, all signatures from this model should be retained through an improved methodology, which allows us to confirm the good agreement between the experiments and first-principle calculations.

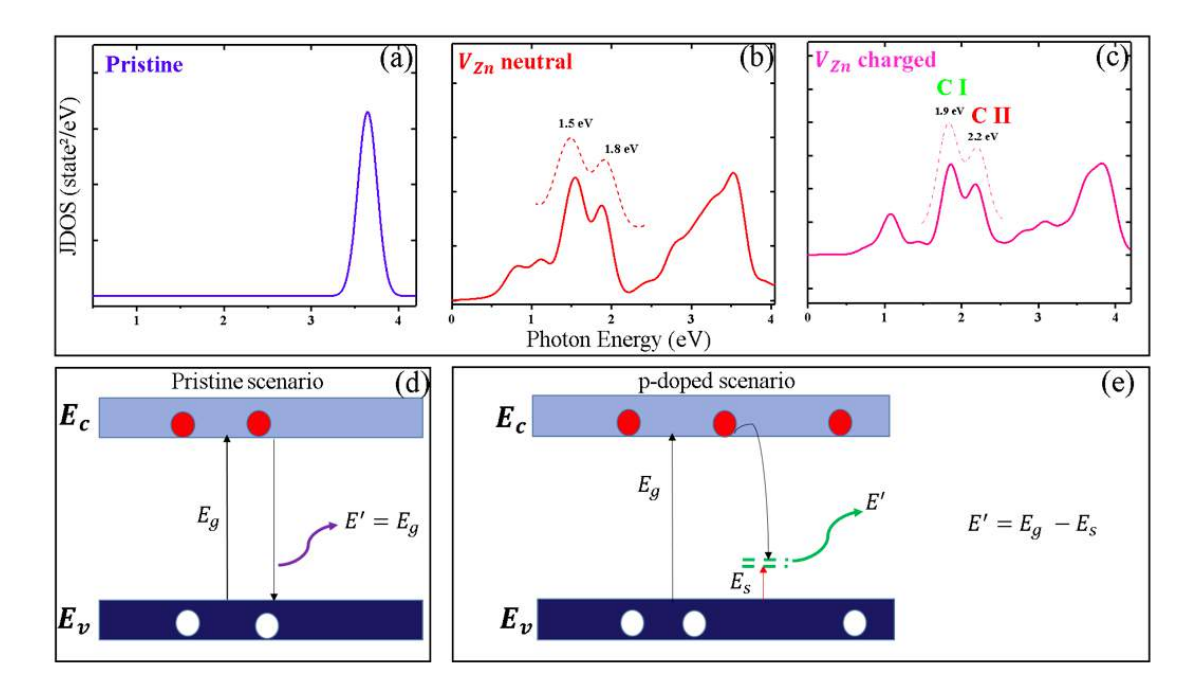


Figure 4.7: Joint Density of states (JDOS) of (a) pristine, (b) neutral V_{Zn} and (c) charged V_{Zn} ZnS. Pictorial diagram level illustrating the emissions in the (d) pristine and (e) p-doped scenarios.

To address the new PL peaks, a suitable approach is to evaluate the joint density of states (JDOS), which represents the allowed inter-band transitions at specific energy levels. Essentially, it can be understood as an emission-like spectrum, enabling the correlation of defect-induced states with experimental photoluminescence features. Fig.4.7(a)-(c) display the JDOS for both pristine and doped ZnS. Our analysis is confined to an energy range that includes IR, VIS, and UV-VIS regions. In the pristine system, there is only one emission, corresponding to a direct recombination process from the VBM to the CBM pro-

ducing photons with 3.6 eV. On the other hand, as we previously discussed, density of states (DOS) calculations show that when a p-type structure forms, new states slightly above the VBM emerge. These states can act as trapping sites, enabling recombination processes beyond the direct VBM-CBM transition. [52] To clarify the role of shallow levels in the emission spectra of ZnS, Fig. 4.7(b) to Fig.4.7(c) show the JDOS of p-type ZnS, obtained by removing one zinc atom from the pristine supercell. In Fig.4.7(b), the neutral configuration is evaluated, revealing new emission lines at 0.8 eV, 1.5 eV, and 1.8 eV, in addition to the 3.6 eV emission line. The high JDOS peaks at 1.5 eV and 1.8 eV suggest a higher probability of these emissions occurring. Therefore, we can infer that zinc vacancies not only enhance optical absorption but also improve optical emission. However, taking PL experiments as the reference, the neutral scenario alone cannot fully explain the two new emissions in the visible range, as discussed in the last section. Thus, we turn our attention to the charged system, depicted in Fig.4.7(c).

The features in this case are quite similar to those in the neutral structure, except for the energy of the emissions. The lowest probability of emission occurs at 1.2 eV, while the highest JDOS components, apart from the 3.6 eV peak, fall exactly in the visible range at 1.9 eV (C I) and 2.2 eV (C II). This finding aligns well with PL experiments, which revealed two new peaks at 2.05 eV and 2.12 eV. Therefore, our ab initio calculations confirm zinc vacancies broadening the ZnS emission lines and suggest these vacancies might be charged in the system. Indeed, as discussed in terms of the formation energy, both neutral and charged zinc vacancies are stable in zb-ZnS and may coexist. The pictorial model distinguishing the pristine and doped scenario is illustrated in Fig.4.7(d) to Fig.4.7(e). In the pristine scenario (Fig. 4.7(d), an electron is excited from the valence band

to the conduction band. Sequentially, this free excited electron recombines directly into the valence band, emitting a photon with energy E, which is equal to the band gap of the system. In contrast, in p-type-like structures, the additional shallow levels in the forbidden zone act as trapping sites. In this case, the free electron that jumped from VBM to CBM recombines at the impurity level E_s , resulting in an emission whose energy E' is the difference of the band gap and the shallow level energy.

Chapter 5

In situ growth of a type-II ZnO/ZnS

heterostructure: From stability to

band-offset

5.1 General Motivation and problem statement

As mentioned throughout this thesis, the search for new renewable energy sources opens the way for discovering and modeling new platforms to obtain highly efficient energy storage sources. If hydrogen storage as well as oxygen evolution reaction are some of the most exciting events hurrying up the industrial race, well-defined, stable interfaces enabling an efficient charge separation, mitigating charge recombination, are the groundbreaking for the solid state community.

A wide range of materials have been pointed out as promising candidates for photocatalytic applications, with particular interest in oxide and sulfide-based structures [57, 58]. In the first class, zinc oxide (ZnO) based materials stand out due to their high chemical stability, non-toxicity, and tunable electronic structure [59, 60, 61]. In the last group, zinc sulfide (ZnS)-based structures have been extensively explored [62, 63] - especially those modified by native defects or substitutional impurities - to enhance conductivity and tailor the band edges to match the redox potential required for water splitting and CO_2 Reduction [64, 65]. Mono-component photocatalysts often suffer from limited charge separation efficiency, which has motivated the exploration of hybrid heterostructures as an advanced approach to enhance photocatalytic performance.

5.2 Heterostructure architectures

The development of engineered heterostructure offers a promising approach to improve both efficiency and performance of different catalyst platforms [66, 13]. These architectures can act as a barrier, preventing the recombination of photogenerated charges, and thus enhancing the charge separation at the interface [67]. Although the potentialities of defect engineering for boosting heterostructure arrangements, there are some important requirements that must be fulfilled for improving photocatalytic processes. One of the main points is the band gap of the systems that will be placed into contact. The typical heterostructure arrangements illustrated in Fig. 5.1 highlight this point.

If we combine two materials whose band gap is way too different from each other (Bandgap(A) >> Bandgap(B), for instance), a type I heterostructure results.

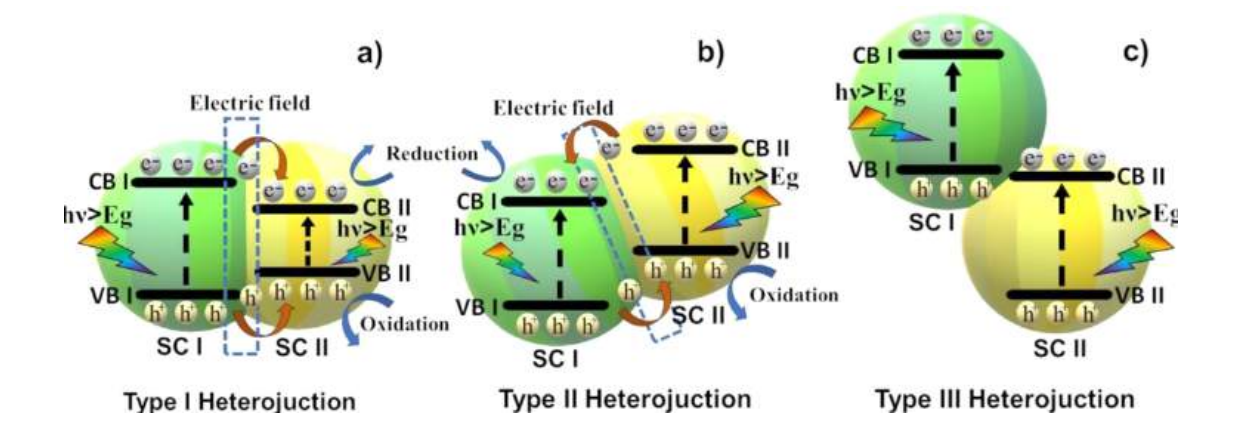


Figure 5.1: Illustration of some Heterostructure prototypes.

Taken from [68]

In this structure, illustrated in Fig.5.1 (a), the band edge of one of the systems is fully contained in between the edges of the other component. Although there is an electron flux toward the material with lower band gap, the charge accumulation in that zone is such that the system display only a single channel for charge separation, thus decreasing the efficiency.

On the other hand, materials with comparable band gap energy give rise to a higher efficient heterostructure, illustrated in Fig.5.1 (b). In this staggered configuration, a dual charge-trapping channel results, improving the charge separation efficiency. This kind of structure is well-known as type-II heterostructure. In this, while electron flow to the semiconductor that has a less negative CB, the holes are transferred to the material that has a less positive VB. The resulted built-in electric-field at the interface is the driving force for photocatalytic reactions.

If type-II heterostructure is the most desirable architectures for photocatalysis, type-III stacking is an option that must be avoided. In this system, the edges of each component are so far way, resulting in an interface with no charge transfer, as illustrated in Fig.5.1 (c). Fortunately, ZnO and ZnS display a similar electronic structure. Depending on the oxygen-to-sulfur content, these systems can operate in S-scheme configurations [69], or more effectively, as type-II heterojunctions—where photogenerated electrons in ZnO transfer to the ZnS conduction band, while holes migrate from ZnS to the ZnO valence band [70].

In this study, we report the in-situ growth of a type-II ZnO/ZnS heterostructure by a controlled oxidation of a ZnS single crystal. Combining X-ray photoelectron Spectroscopy (XPS) and Atomic force microscopy (AFM), we investigated the electronic structure and surface morphology of the resulting interface. A comprehensive understanding of the band alignment in such hybrid structures could significantly advance the rational design of ZnO/ZnS photocatalysts. The reader can access the full paper derived from this research free of charge at https://pubs.acs.org/doi/full/10.1021/acs.jpcc.5c05124.

5.3 Results and discussion

5.3.1 XPS analysis

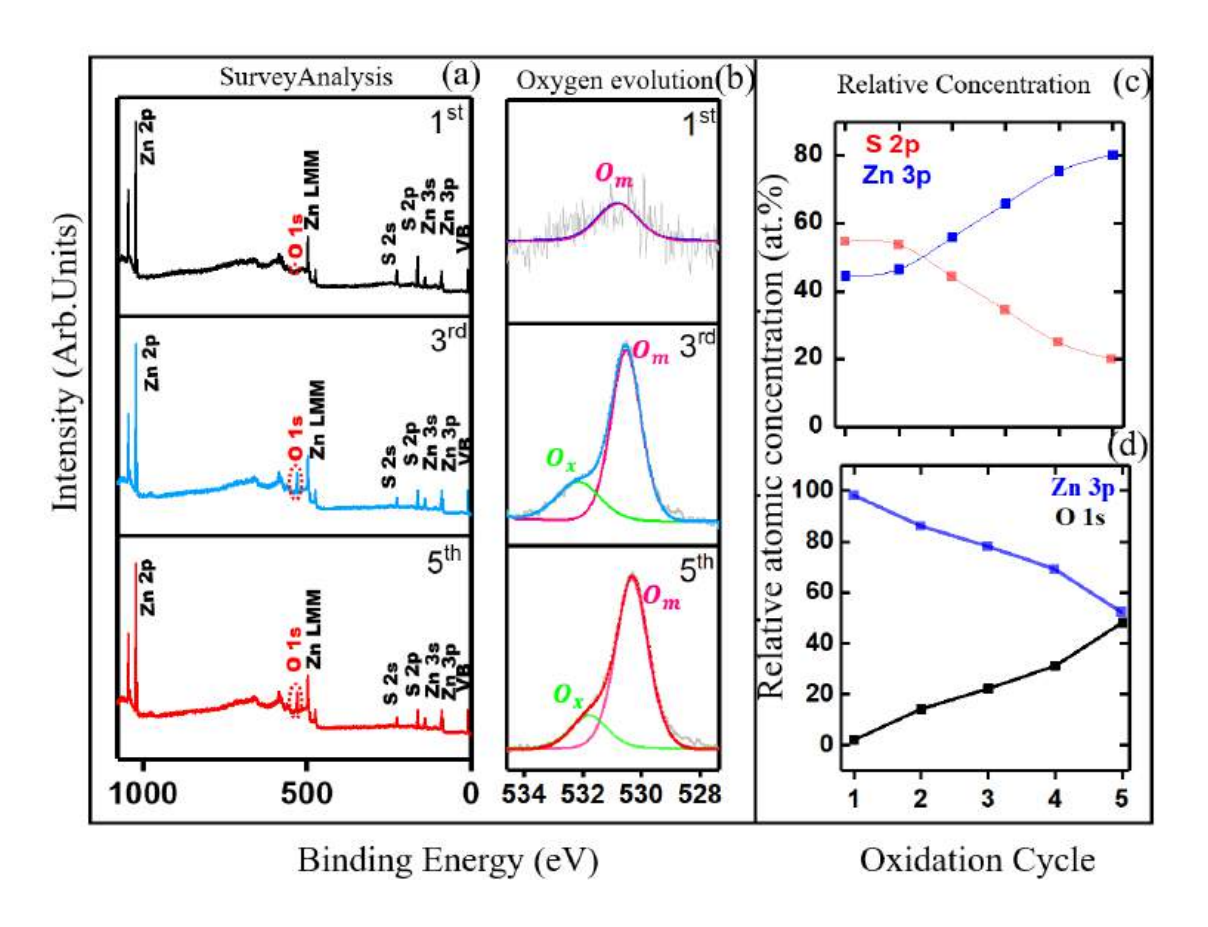


Figure 5.2: XPS (a) Survey and (b) high-resolution O 1s analysis of the ZnS sample after several oxidation cycles; (C) Zn 3p x O1s relative atomic concentration and (d) film thickness estimation as a function of the oxidation cycle. All the spectra were collected at Room temperature in UHV conditions. All binding energies were calibrated with respect to the Zn 3s orbital.

The evolution of the ZnS surface upon successive oxidation cycles was investigated through XPS analysis, as shown in Fig.5.2a. Core-level signals characteristic of ZnS, such as Zn 2p, S 2p, and Zn 3p, are clearly observed. For ZnS exhibiting improved conductivity relative to its insulating counterpart, these

components typically appear at 1022.8 eV (Zn 2p), 140.5 eV (Zn 3s), and 162.5 eV (S 2p) [46]. Upon oxidation, new spectral features emerge—most notably oxygen-related peaks such as O 1s and O KLL. A systematic shift toward lower binding energies is observed across several core levels as a function of oxidation cycles. Using the center of the Zn 2p peak as a reference, we note its position shifting from 1022.8 eV after the first cycle (black line) to 1022.5 eV after the third (light blue) and finally to 1022.2 eV after the last cycle (red line). These trends are consistently observed across all detected core levels and are summarized in Table S1 of the main manuscript [71]. The gradual shift toward lower binding energy is attributed to the progressive incorporation of oxygen into the ZnS lattice, resulting in the formation of a ZnO/ZnS heterojunction. Dong et al. [72] reported that such interfaces exhibit a similar shift in XPS peaks due to interfacial charge redistribution. Interestingly, the energy difference between the Zn 2p and O 1s peaks decreases from 492.0 eV (first cycle) to 491.4 eV (final cycle)—approaching the characteristic ΔE separation found in ZnO systems [73] and confirmed by our XPS data on a ZnO (0001) single crystal (Fig. S2 in [71]).

To further elucidate the chemical evolution, high-resolution O 1s spectra as a function of oxidation cycles are presented in Fig.5.2b. After the first cycle (black line), a weak but noticeable O 1s signal is detected. Repeating the oxidation treatment (up to five cycles, at which point saturation occurs) results in a progressive increase in the O 1s intensity, accompanied by a broadening of the peak envelope. In particular, it is well fitted into two components: A peak at 530 eV, related to oxygen bound to zinc (O_m) , and a satellite component at high binding energy addressed to dative bond of oxygen species (O_x) , with either water molecules or two atoms with different electron affinity [74]. No features related to oxygen-sulfur (SO_x) species are observed, likely due to their volatility

and desorption under UHV conditions [75]. Of particular interest is the slight shift of the O 1s spectrum in the final stage, in which the components lie 0.2 eV away from the positions measured in the former cycles. This aspect is well-aligned with the band-bending like effect due to the formation of a ZnO/ZnS heterostructure.

More information regarding the ZnO/ZnS heterostructure evolution is derived from the relative atomic concentration of sulfur and zinc, as shown in Fig. 5.4c. The comparison between S 2p and Zn 3p orbitals is a reliable measurement to analyze the effect of oxygen insertion into the ZnS lattice. As discussed in our previous study, the ZnS system is more conductive due to the formation of zinc vacancies in the system [38]. In this scenario, the sulfur concentration is higher relative to the Zn counterpart. On the other hand, upon oxidation, part of the S 2p content decreases. This event is related to the insertion of oxygen into the lattice rather than the formation of sulfur vacancies. Indeed, oxygen atoms display higher electronegativity than sulfur. Once the removal of zinc atoms promotes an S-enrichment of the surface, the zinc atoms that have moved inward to the surface tend to be more likely bound by oxygen than sulfur. Then, the ZnS surface becomes oxygen-rich, decreasing the S 2p concentration relative to the Zn 3p one. To gain quantitative insight into the oxygen uptake, the relative atomic concentration of O 1s and Zn 3p orbitals is plotted in Fig.5.2d. Given that O 1s and Zn 3p electrons originate from different sampling depths, their contributions are corrected using IMFP values calculated via the QUASES software [76]. Moreover, the Zn 3p orbital is most-likely bulk-sensitive, thus the vast majority of photoelectrons escaping from this orbital are signatures of zinc atoms bonded to sulfur species. In contrast, the O 1s signal is more surface-sensitive, providing information regarding zinc oxide present at the surface. Therefore a relative comparison between these orbitals enables an indirect estimation of the ZnS area covered by the ZnO overlayer. Initially, less than 2% of the ZnS surface is oxidized. After the third cycle, ZnO covers more than 30% of the surface, and by the final cycle, the O 1s and Zn 3p contributions are nearly equal, implying that approximately half of the ZnS surface is covered by ZnO. A quantitative estimation of the ZnO film covering the ZnS surface is obtained through the thickogram method [26]. For this description, O 1s and Zn 3p were selected as the film and substrate signals, respectively. The former is chosen because its contribution is exclusively addressed to the overlayer. The latter one is the most reliable way to avoid overestimation since all components coming from sulfur, like S 2s and S 2p, are more surface-sensitive and thus deeply affected by the oxygen increasing along the cycles, as discussed before. A full description of both the thickogram method and the parameters used to estimate the films are reported in the Appendix I. Overall, the thickness of the film spans from 0.5 nm to 4 nm.

5.3.2 AFM analysis

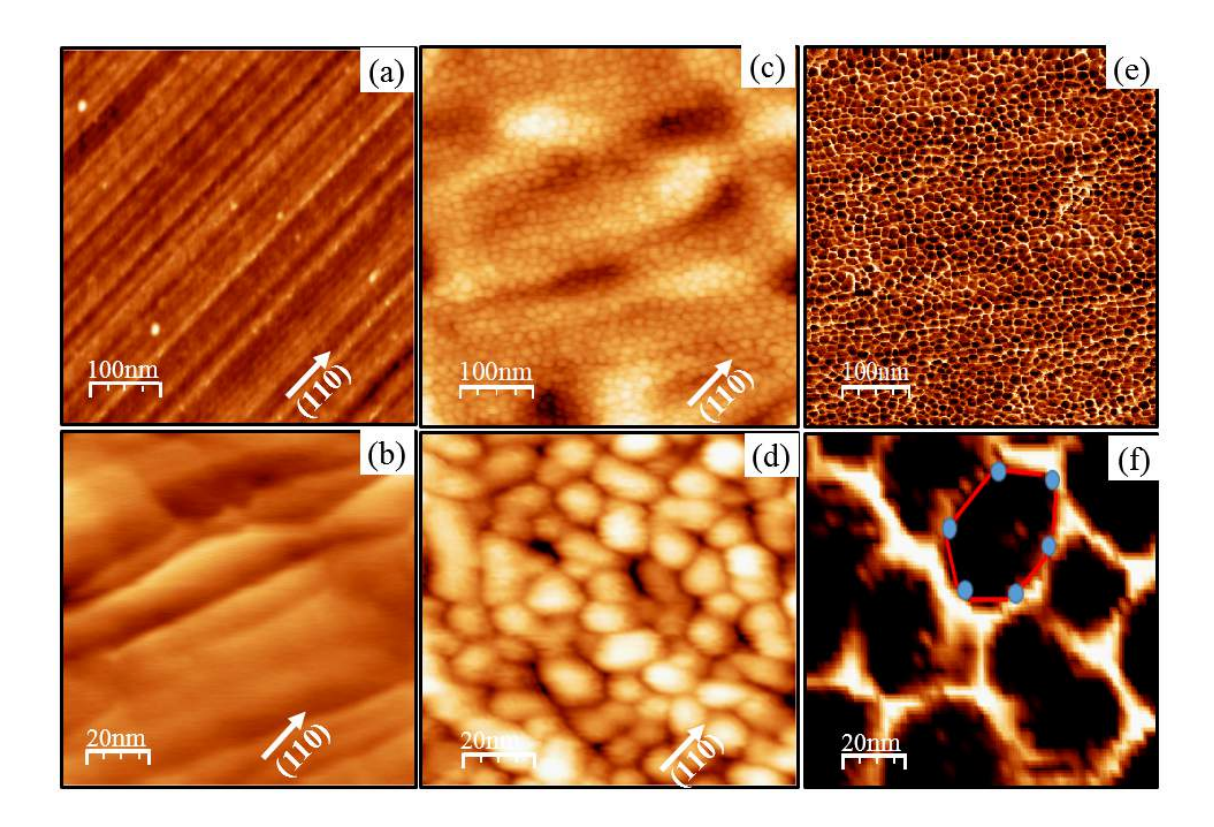


Figure 5.3: Tapping-mode AFM measurements of the ZnS (001) single-crystal (a) before and (b) after obtaining a ZnO/ZnS heterostructure. (C) Phase image of the height AFM image in (b). The up-left corner inset emphasizes the hexagon-like shape, as pointed by the red contour with 6 blue points in each vertices.

The morphological evolution of the ZnS surface following the formation of a ZnO overlayer was investigated via Atomic Force Microscopy (AFM), as shown in Fig. 5.3. In Fig. 5.3 (a)-(b), the pristine ZnS(001) surface prior to oxidation is presented. As discussed in our previous work [?], the ZnS (001) is a Tasker type III surface, which achieves equilibrium through specific lattice modifications such that surface dipole interactions are compensated. In our study, this compensation is induced by several cycles of gentle sputtering and UHV annealing at high temperature (up to 1520 K), promoting the preferential removal

of zinc atoms. In this scenario, the remaining zinc and sulfur species undergo opposite displacement -Zn atoms migrate slightly inward, while S atoms shift outward, resulting in a Sulfur-rich surface. Morphologically, this results in a relatively flat surface, composed of several small terraces and step edges aligned along the [110] direction. These step edges are useful for promoting confined atomic interactions via Coulomb repulsion mechanism, which can hinder lateral adatom diffusion. On the other hand, they may also enhance interfacial strain, particularly when there is a symmetry mismatch between the substrate and the overgrown film.

Upon surface oxidation, AFM topography reveals a densely packed array of ZnO nano-island layers characterized by triangular or hexagonal-like shapes, as shown in Fig. 5.3(c) and highlighted in Fig. 5.3(d). These islands display a height profile of 3-4 nm and average diameter of 8-12 nm. This layer-plus-island arrangement upon oxidation of ZnS surface is compatible with a compact ZnO film exposing top facets of either zinc blende (ZB) (111) or wurtzite (WZ) (0001) surface planes. Although ZnO preferentially adopts WZ structure, which is the most stable at ambient conditions, ZB ZnO structure cannot be ruled out, since it can be stabilized on cubic substrate, as in the case of ZB ZnS used in this study. Overall, in view of both substrate step-edge and the lattice mismatch between film and substrate - $a_{ZnO} = 3.25 \text{ Å}[77]$, $a_{ZnS} = 3.85 \text{ Å}[38]$ - makes the epitaxial growth of ordered ZnO films on ZnS highly unfavorable. The crystallographic arrangement of that heterostructure would be investigated by LEED. Yet, further LEED measurements does not results in well defined spots or patterns, potentially due to the overlayer thickness (of about of 4 nm), which is below the typical LEED coherence probing depth [78].

To gain further insight into local structural heterogeneities, we analyzed the corresponding AFM phase image. AFM phase imaging is a powerful tool for visualizing compositional or mechanical contrasts at the nanoscale. In Fig. 5.3(e), the ZnO islands manifest as bright contours, indicating phase contrast relative to the ZnS substrate. In particular, distinguished textures and distorted hexagonal features are also observed in some regions, as highlighted by the red contour and blue spots in Fig. 5.3 (f). The surface steps and terraces amplify local strain fields, leading to anisotropic relaxation or distortion of the growing ZnO domains. The presence of lattice mismatch and vicinal-induced strain are expected to influence not only the morphology but also the electronic structure of the ZnO/ZnS interface. These effects will be explored in the next section through high-resolution core-level and valence band XPS analyses.

5.3.3 Electronic structure analysis

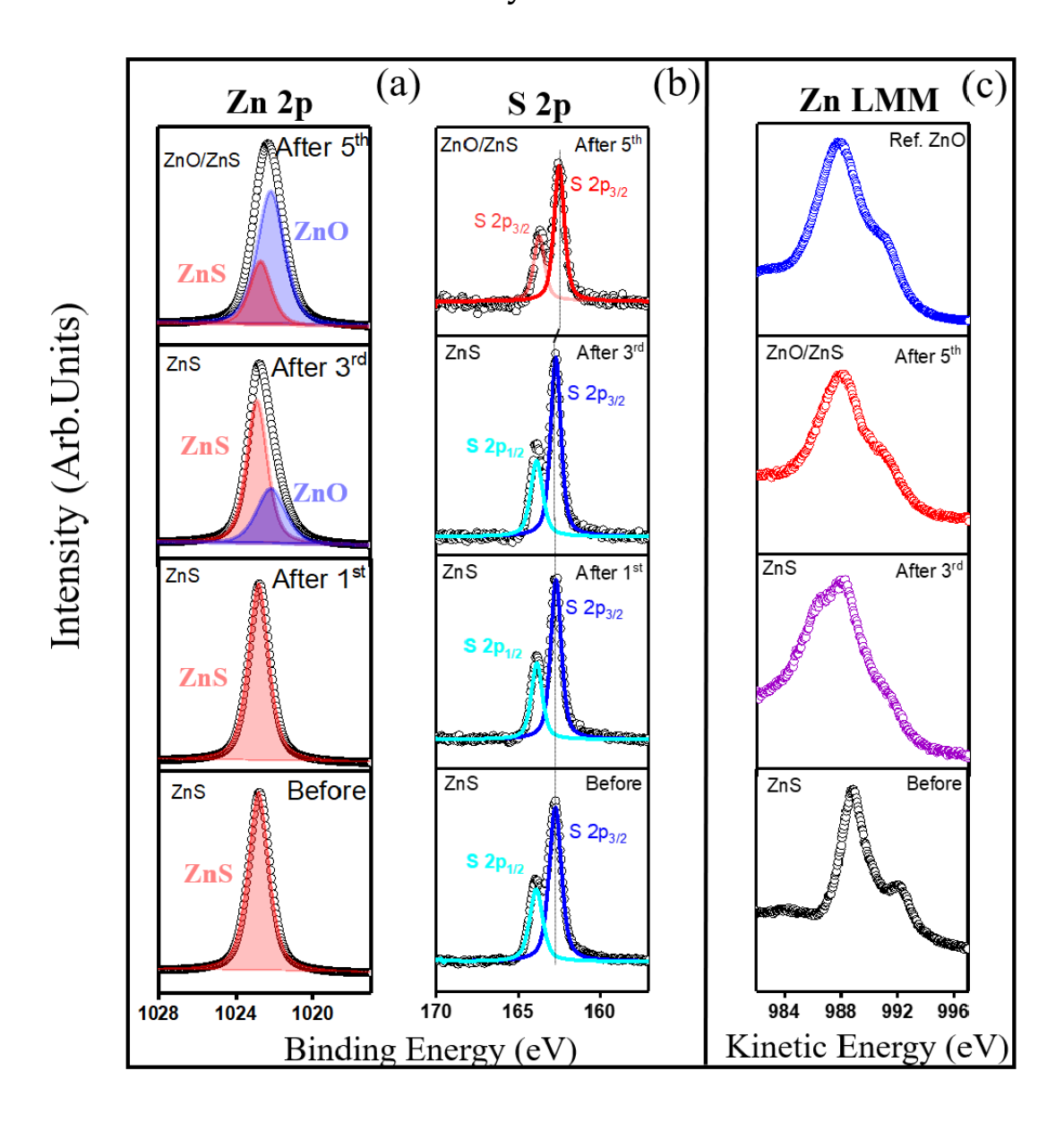


Figure 5.4: High-Resolution XPS spectra of (a) Zn 2p, (b) S 2p, and (C) Zn LMM. All the spectra were collected at room temperature.

The electronic structure of the ZnO/ZnS heterointerface is derived by high-resolution XPS spectra depicted in Fig.5.4. In Fig.5.4(a) is shown the $Zn\ 2p_{3/2}$ peak evolution during oxidation cycles. Before oxidation the center of the peak is centered at 1022.8 eV. This result is unchanged after the first oxidation cycle,

with the peak well described by a single component at the same binding energy. Yet, as long as the ZnS surface oxidation increases, the envelope is better described by two components, as noted in Fig.5.4(a) (third and forth panel). The component at high binding energy - 1022.8 eV, addressed to ZnS, and the lower binding energy contribution at 1022.2 eV is attributed to the Zn atoms coordinated with oxygen in the ZnO arrangement. Interestingly, while the ZnO signature after the third oxidation cycle correspond to 20 % of the overall $Zn 2p_{3/2}$ area, after the last cycle (Fig.5.4(a) top panel) it dictates the overall envelope covering more than 70 % of the total area. As discussed through Survey spectra analysis, the S-rich characteristic of the ZnS substrate is converted into an oxygen-rich surface upon oxidation. In the limit, when a ZnO/ZnS heterostructure is formed, almost a half of ZnS surface is covered by ZnO islands. Therefore, given that Zn 2p is the most surface sensitive peak of the system, it is not surprisingly that ZnO component dominates the overall signal. Notably, employing that contribution in the quantification of zinc and oxygen in the ZnO/ZnS heterointerface we obtained a Zn/O ratio of ~ 0.75 , in good agreement with a zinc-terminated ZnO surface [79]. Additionally, the ZnS component is slightly shifted toward low binding energy after the last oxidation cycle, indicating a subtle change in the local electrostatic potential after the formation of the ZnO/ZnS heterostructure. This shift is also noted when comparing the S 2p components in Fig.5.4b. Initially, before oxidation, the S $2p_{3/2}$ is found at 162.8 eV, 1.2 eV apart away from the S $2p_{1/2}$, as expected for ZnS systems. Despite keeping the same features through all the oxidation cycles, we noted the core component shifts to 162.6 eV in the hybrid system. This offset aligns well the band bending hypothesis [80], which takes place due to the formation of a hybrid interface. As ZnS and ZnO have a slightly different electronic structure, the Fermi level alignment upon contact results in a shift of the core-level components. The B.E. offset direction is directly related to the bending direction. While a high B.E. shift signals a downward bending of the bands, a low B.E. shift indicates an upward shift of the bands. Further support for the emergence of ZnO-like electronic structure is obtained from the analysis of the Zn LMM Auger region displayed in Fig.5.4c. In the ZnO reference sample, the Zn LMM line appears as a sharp, shoulder-free peak at ~ 989 eV -kinetic energy (K.E) units. In contrast, the ZnS spectrum exhibits a shoulder at higher K.E, characteristic of the different local coordination and oxidation state. This shape dramatically changes as a function of the oxidation cycles. Especially after the last cycle in which the ZnO/ZnS heterostructure results, this shoulder disappears, and the Auger peak becomes more ZnO-like in shape, highlighting the prevalence of Zn–O coordination. It is worth noting that changes in Auger line shape are strictly related to changes in the oxidation state [81]. This suggests that Zn atoms at the interface experience a mixed chemical environment, leading to electronic heterogeneity that may influence charge transfer or carrier confinement at the heterojunction.

5.3.4 Band offsets

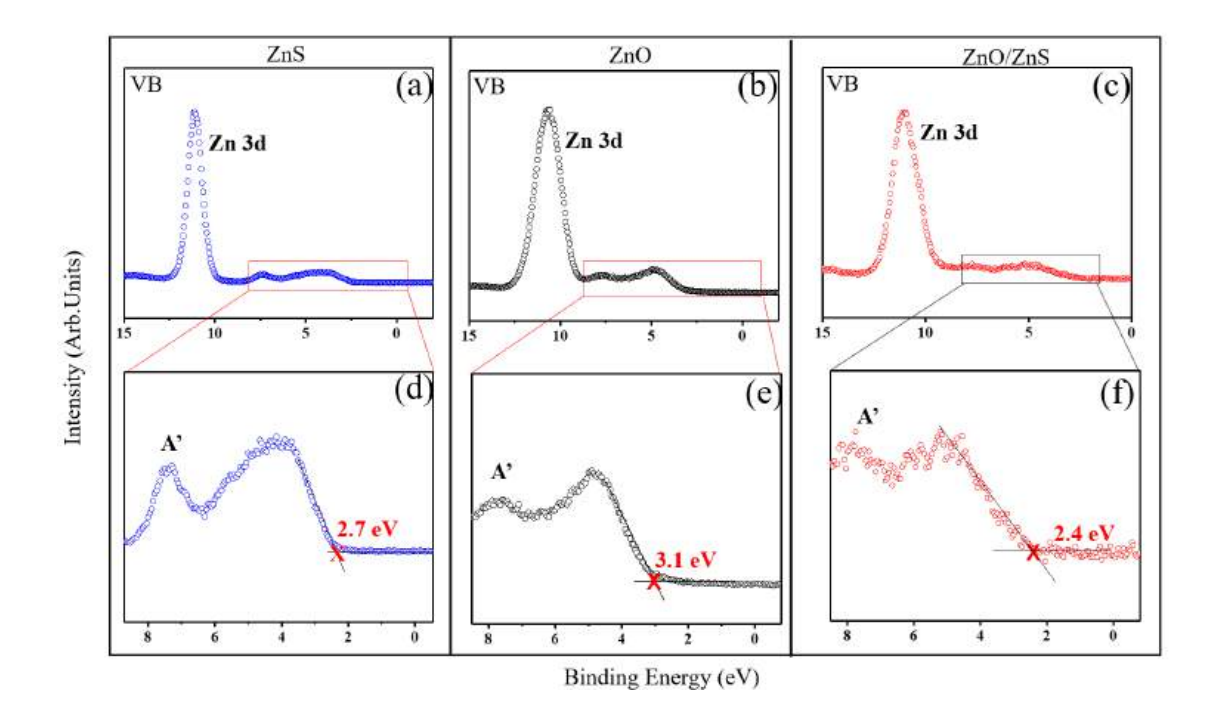


Figure 5.5: Valence band XPS spectra of (a) ZnS (b) ZnO (c) and ZnO/ZnS system. In (d), (e) and (f) are displayed the valence band maximum estimation for all these structures, in the mentioned order. All the spectra were collected at room temperature.

Fig.5.5 displays valence band (VB) XPS spectra and the respective VBM of the ZnS (001) and ZnO (0001) single-crystals, and the ZnO/ZnS heterostructure. The main peak in each scenario is the Zn 3d orbital, lying at 11.4 eV for ZnS (Fig.5.5(a)), 10.8 eV for ZnO (Fig.5.5(b)), and 11.0 for ZnO/ZnS (Fig.5.5(c)), respectively. The features between 3 eV to 8 eV are most likely dominated by S 3p (O2p) in pristine ZnS (ZnO) systems, with further minor contributions of Zn 4sp or Zn 3d, as highlighted in Fig. 5.5 (d) and (e), respectively [82]. Interestingly, these features are quite changed after the formation of a ZnO/ZnS heterostructure, as noted in Fig. 5.5 (f). In particular, the component labeled A' around 8 eV quite decreases in intensity. Subtle changes in this portion of the

valence band of group II-VI semiconductors like ZnO and ZnS are addressed to surface coverage [82]. In the case of the in situ growth of ZnO/ZnS heterostructure, we might connect this change with the decrease of the sulfur content upon the oxidation of the ZnS surface, as discussed in the last section. In this scenario the valence band of the heterointerface will be most likely ZnO in fashion. This electronic modification in the VB is better visualized via ultra-violet photoemission spectroscopy (UPS), revealing the tailling of the A' component (see the supporting information of the full paper).

More information regarding electronic structure modifications are derived from the VBM positions of each system displayed in in Fig.5.5(d)-(f). The VBM of ZnS is determined to be 2.7 eV, while ZnO exhibits a slightly higher VBM at 3.1 eV. Once ZnO possesses a narrower band gap than ZnS [83], the relative alignment of their electronic bands dictates that the VBM of ZnS is positioned lower (less positive) than ZnO VBM. On the other hand, the conduction band minimum (CBM) of ZnO is less negative than that of ZnS, arising close to -0.2 eV. These values might differ depending on particular sample characteristics, though the general trend is still valid. According to Nichols et al. [84], it is possible to estimate the band gap energy of each sample through the onset in the core spectra of the samples. In our case, the ZnS and ZnO band gap are 3.77 eV and 3.41 eV, respectively (Fig A2). These values are well aligned with typical literature results – 3.6 – 3.8 eV for ZnS and 3.2-3.5 eV for ZnO- Given the band gap of the systems, one can estimate the CBM ($CBM = E_{gap} - VBM$). While the ZnO CBM is close to -0.1 eV, the ZnS CBM is around -1.2 eV, consistent with the expected trend mentioned before. The measured VBM of the heterostructure (~ 2.4 eV) reflects the upward bending of the bands, further indicating interfacial charge redistribution. In view of the ZnO and ZnS VBM-CBM positions, we might characterize the ZnO/ZnS arrangement as a Type-II heterostructure, where the bands undergo an upward shift. This phenomenon agrees very well with our XPS core level analysis, which suggests a band-bending effect. It is also well-aligned with the previous discussion regarding the strain between the ZnO/ZnS heterostructure due to the lattice mismatch. That strain might give rise to a built-in electric field across the interface, leading the bands to bend.

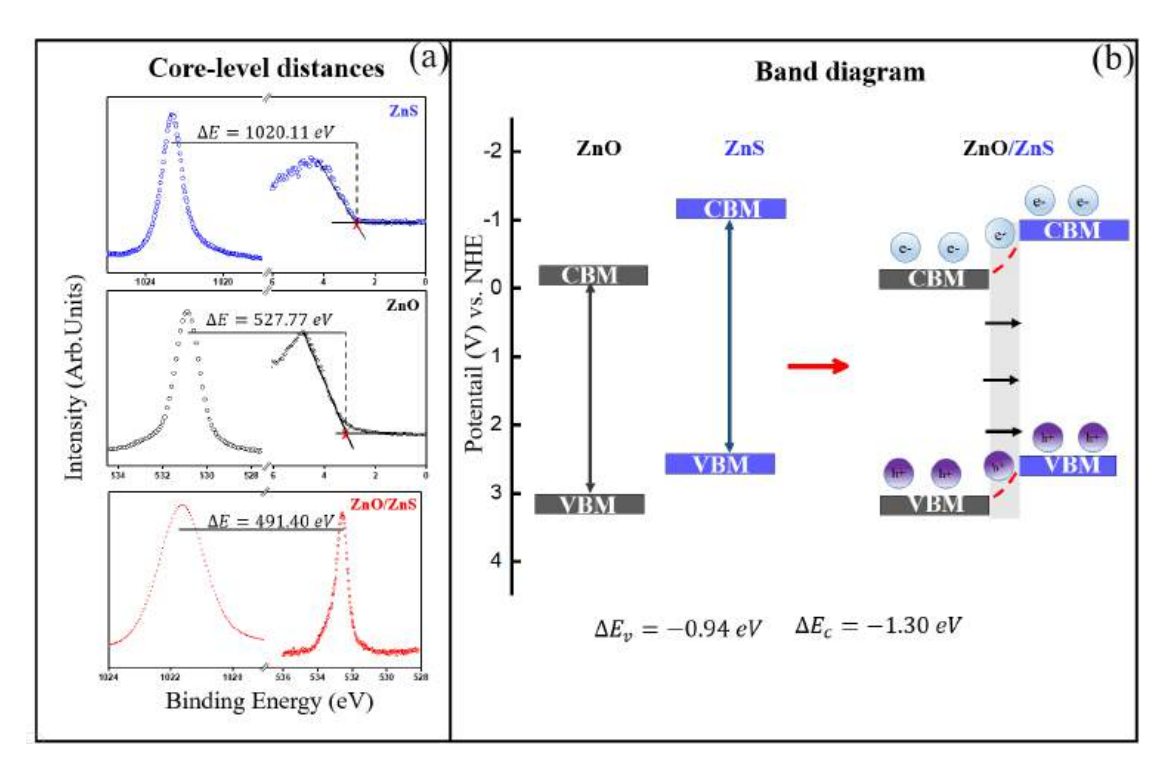


Figure 5.6: (a) Reliable XPS spectra to get the core-level shift estimation. (b) Pictorial band diagram illustrating the individual ZnO and ZnS configuration before contacting vs the hybrid system junction.

Interestingly, following the description of Schultz and co-workers, it is possible to measure the bending by computing the band offsets [85]. The valence band-offset E_{VBO} between a system A formed over a system B is given by:

$$E_{VBO} = (E_{core}^{A} - E_{VB}^{A})_{A} - (E_{core}^{B} - E_{VB}^{B})_{B} + (E_{core}^{B} - E_{core}^{A})_{A/B}.$$
 (5.1)

The first terms in Eq.5.1 E_{core} and E_{VB} refer to the core-level-VBM distance of the systems A and B, respectively. In our context, these values are the measurements on the ZnS and ZnO single-crystals. The last term, on the other hand, stands for the distance between the core peaks of each system upon contact. In the case of a ZnO/ZnS Eq.5.1 reads as:

$$E_{VBO} = (E_{O1s}^{ZnO} - E_{VBM}^{ZnO})_{ZnO} - (E_{Zn2p}^{ZnS} - E_{VBM}^{ZnS})_{ZnS} + (E_{Zn2p} - E_{O1s})_{ZnO/ZnS}.$$
(5.2)

The choice of Zn 2p as the core-level of ZnS and O 1s for ZnO is arbitrary, though there are some important features to be noted. We would have chosen S 2p and O 1s, for instance, for each respective system. However, the S 2p signal becomes narrow when the heterostructure is obtained. In addition, while the spin-orbit of the S 2p components is 1.3 eV, the components of Zn 2p arise 23 eV apart from each other, making Zn 2p orbital less susceptible to overestimation regarding the binding energy position. The Zn 2p orbital would work well for ZnO films, yet its component is not well-defined in the heterostructure, which could have led to inconsistencies in determining the binding energy position.

All the reliable binding energy positions for computing the bending of the ZnO/ZnS heterostructure are shown in Fig.5.6(a). In ZnS (Fig.5.6(a) top panel),

the distance between the Zn 2p and the VBM is 1020.11 eV. On the other hand, O 1s is 527.77 eV away from the VBM position in ZnO (Fig.5.6(a) middle panel). At the interface, O 1s and Zn 2p are separated by 491.40 eV. Taking into the account Eq.5.2, we found $E_{VBO} = -0.94 \ eV$. The estimated uncertainty in the E_{VBO} was derived from the fitting procedure for determining the VBM of each system, leading to an error propagation in the core level-to-VBM distance (first two terms in Eq.5.2). Based on our choice, we estimate the E_{VBO} uncertainty around $\pm 0.08 \ eV$. The band offset is completely determined by computing the conduction band offset E_{CBO} as follows [86]:

$$E_{CBO} = E_{VBO} + (E_{gap}^{ZnO} - E_{gap}^{ZnS}). {(5.3)}$$

Given the estimated band gap of ZnO (3.41 \pm 0.06 eV) and ZnS (3.77 \pm 0.06 eV) samples, and the calculated E_{VBO} , Eq.5.3 yields $E_{CBO} = -1.30\,eV$. In the E_{CBO} calculation we must also taking into account the error in the fitting procedure to estimating the band gap. Given the E_{VBO} and E_{gap} uncertainties, we obtained the E_{CBO} uncertainty of \pm 0.11 eV. A schematic representation of this band alignment at the interface is given in Fig.5.6(b). Based on our XPS measurements of each individual system and using the potential Vs NHE as a reference scale, the ZnO CBM is less negative and ZnS VBM less positive, as discussed before. Once the hybrid interface is formed, the upward shift of the ZnO bands with respect to ZnS implies the ZnO CBM become more negative, while its VBM turns less positive. This fact explains the negative band offset value. The presence of a sizable conduction band offset ($-1.30 \pm 0.11\,eV$) and valence band offset ($-0.94 \pm 0.08\,eV$) is critical from a catalytic standpoint. This alignment promotes efficient spatial separation of photogenerated carriers—electrons accumulate in

the ZnS conduction band, while holes concentrate in the ZnO valence band. Such separation minimizes recombination losses, thereby enhancing the lifetime of reactive species at the surface. Moreover, the built-in electric field that can drive charge migration toward the interface, potentially improving the kinetics of interfacial redox processes. In addition, the ZnS band gap might be tailored due to the increasing of ZnO layers, which might broad the optical absorption energy [87]. This property is of particular interest for an efficient photocatalytic performance.

Chapter 6

Insights into CO_2 adsorption and CO oxidation

6.1 Overall contextualization

In the past decade, the world has been experiencing a huge increase in pollutant gas emissions, especially CO_2 and CO [88]. It is not surprising that the reported correlation with the universal temperature rising up 2 C - Taking the former industrial period as a reference point. As discussed in many reviews and perspectives, the control of those gases, particularly the conversion of them into non-harmful products is one of the main challenges of the 21^{st} century.

Strategic reactions like CO_2 hydrogenation or CO oxidation are some of target mechanism that yield useful and green-friendly products, such as methanol and Hydrogen. On the other hand, there is a lack of efficient catalysis for boost-

ing these reactions. In the context of surface reactivity, the concept of efficiency is roughly linked to the catalyst capability of converting the initial product into final new yields. In a deeper perspective, it will depend on the number of active sites, which means places in the catalyst that allow for either trapping molecules or reacting them out.

Of particular interest in this thesis, native defects are a special route for improving catalytic capability. The new levels usually introduced by shallow impurities might significantly increase the number of active sites, which allow the interaction between the catalyst's surface and the target molecule. This is the first step toward reaction. The strength of that interaction is ultimately linked to the sub-sequent behavior of the activated molecule- they might stick on the surface, in the case of strong interaction, or might leave it away if a weak interaction results. The aspect regarding the nature of interaction is briefly discussed in the next subsection.

6.2 Useful background review

6.2.1 Adsorption mechanism: Chemisorption x Physisorption

The nature of catalyst-adsorbate interaction depends on energetic questions. The lower -more exothermic the adsorption energy is, the higher is the probability of that molecule interacting with the catalyst surface. Yet, that does not imply chemisorption. If long-range interaction dominates, the systems enrolled in the process might be interacting most likely in a VdW fashion. This is a weak interaction well known as physisorption. In a VdW-type bond, no charge transfer

is involved. The instantaneous dipole moments of the adsorbate and its nearest neighbors' surface atoms provide the attractive force.

On the other hand, high exothermic adsorption is typically addressed to the chemisorption mechanism, where a strong bond is created between the molecule and the substrate surface. In a microscopic point of view, we shall interpret chemisorption as the superposition of wavefunctions of valence electrons of molecule and substrate, giving rise to a new wave function that is the convolution of these mentioned ones. Therefore, the electrons associated with the bond might be thought of as moving both the adsorbate and the catalyst structure, which gives rise to a covalent bond.

6.2.2 Modeling molecule adsorption

The DFT framework allows for modeling the adsorption of molecules by computing the adsorption energy E_{ads} as follows:

$$E_{ads} = E_{S+Mol} - (E_S + E_m). (6.1)$$

In Eq.6.1, E_{S+Mol} and E_S stand for DFT total energy of the system with the molecule and the pristine itself, respectively. The term E_m is the DFT total energy of the individual molecule under investigation. The particular molecule is modeled by inserting it into a cubic box and allowing a full relaxation such that the force and energy in the system are lower than the threshold, which is typically 0.0001 eV / Å and 10^{-8} eV. The lower the adsorption energy, the easier it is for the molecule to be adsorbed in the system. The signal of the adsorption energy

ergy dictates whether an exothermic or an endothermic reaction will take place. While the first displays negative adsorption energies, the last one is positive and indicates that such a reaction is very energetically unfavorable.

Following the full relaxation of the ions, the molecule's starting configuration does not play a crucial role. Given that the molecule is available to relax, it will reach its ideal arrangement when its lower energy configuration is achieved. On the other hand, for some cases, it is important to consider its spin configuration. For instance, the singlet and triplet states of oxygen are quite similar; however, it dictates whether SiO_x oxidation will take place or not [89]. Yet, this property does not modify the trends observed in our investigations. Therefore, all molecules are positioned upward to the surface.

6.3 Results and Discussion

In this chapter we investigated whether CO_2 molecules are adsorbed on defective ZnS Surface. In the first part, we aim to explain the thermodynamic picture in which that reaction takes place, comparing the role of temperature and CO_2 pressure (coverage) in the overall reaction. Next, combining CO_2 gas at different environments, such as O_2 and CO, we compare whether that mixed atmosphere improves the CO_2 adsorption efficiency. Ending, DFT calculations shed light on the adsorption behavior comparing the defective and defect-free ZnS surface behavior upon interaction with CO_2 and O_2 .

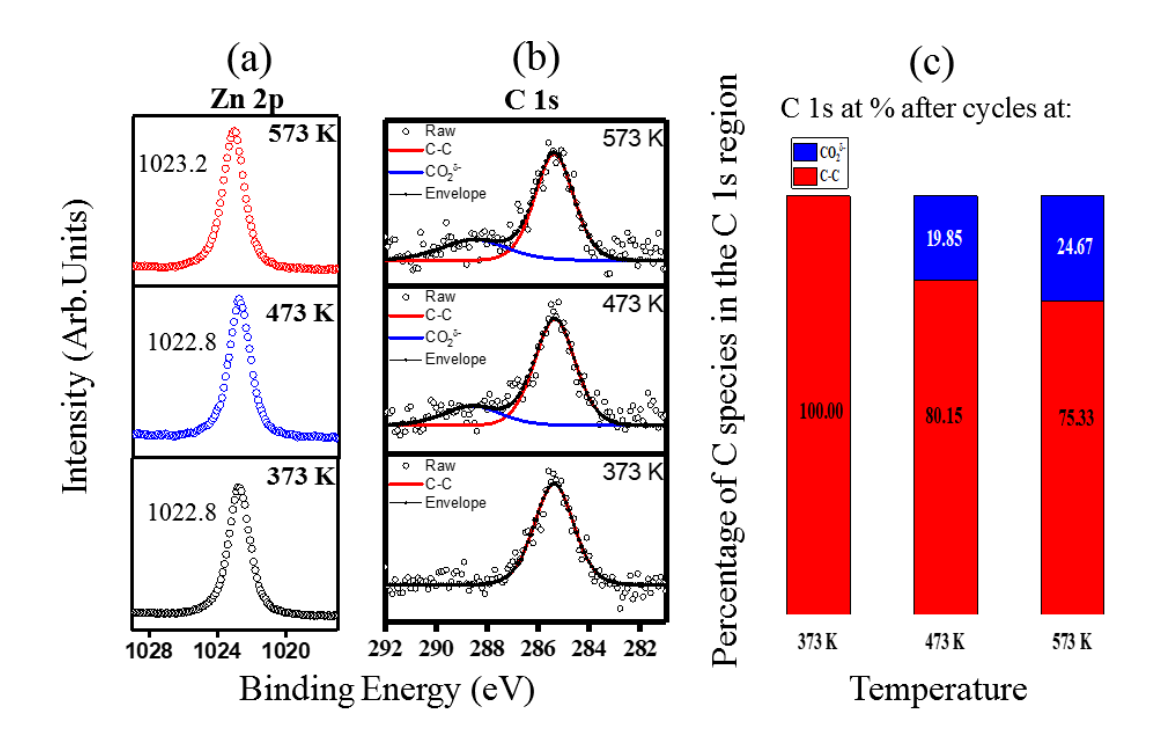


Figure 6.1: APXPS operando analysis of (a) Zn 2p (b) O 1s spectra as a function of the heating temperature; (C) Relative atomic concentration of the C 1s components after cycles as a function of the temperature.

6.3.1 CO_2 adsorption

The role of temperature in the adsorption of CO_2 molecules is assessed by analyzing the in situ reaction between CO_2 and the defective ZnS surface, as shown in Fig.6.1. Fig. 6.1(a) displays the Zn 2p core-level spectra of the ZnS surface exposed to 0.55 mbar of CO_2 at different temperatures. Initially, at 373 K, the Zn 2p peak appears at the expected binding energy (B.E.) of 1022.8 eV. This binding energy remains nearly unchanged as the temperature is raised to 473 K. However, at 573 K, a significant shift of +0.4 eV toward higher binding energy is observed. Such subtle modifications in the core-level position are typically associated with changes in the local chemical environment from which the photo-

electrons are emitted. In in situ XPS experiments like ours, a shift toward higher binding energy is generally interpreted as the onset of a chemical reaction—in this case, suggesting the interaction of CO_2 with the ZnS surface. Moreover, as discussed in the previous chapter, once the reaction stabilizes or new molecular species are incorporated into the system, it is common to observe a reversal in the binding energy shift, often toward lower values, reflecting changes in final-state effects or charge redistribution. Based on this behavior, we infer that 573 K represents a threshold temperature for initiating CO_2 adsorption or activation on the ZnS surface, where reactivity becomes thermodynamically favorable.

Further insights into CO_2 adsorption on ZnS are obtained by analyzing the C 1s core-level spectra under the same experimental conditions, as shown in Fig.6.1 (b). The characteristic fingerprint of CO_2 is a satellite peak appearing at higher binding energy, typically 3 eV above the main sp^3 -hybridized carbon signal centered at 285.8 eV [90]. At 373 K, the C 1s spectrum is well described by a single component at 285.8 eV, attributed to C–C bonds in an sp^3 configuration, commonly associated with background carbon contamination. Interestingly, as the temperature increases, a new feature emerges at high binding energy, approximately 3 eV above the sp^3 peak. This component is commonly assigned to activated CO_2 species and is widely reported as a signature of CO_2 adsorption and partial charge transfer [91]. This high-binding-energy component becomes more pronounced at 573 K, indicating that CO_2 adsorption initiates at 473 K but becomes substantially more effective at 573 K.

To gain quantitative insights, we analyzed the relative contributions of each C 1s component at each scenario discussed above CO_2 , as shown in Fig.6.1(c). At 373 K, no reaction is observed, and the C 1s signal is dominated by the C–C sp^3

component. At higher temperatures, the $CO_2^{\delta-}$ component increases in intensity, particularly at 573 K, where it contributes to more than 24 % of the total C 1s area. This finding reinforces that 573 K is the optimal temperature for promoting CO_2 adsorption on the ZnS surface under the studied conditions.

6.3.2 On the activation mechanism

The pathway for CO_2 activation on ZnS surface is not well established yet. As we discussed, there were no previous reports on ambient pressure experiments with the ZnS-catalyst model. In that way, we based our analysis on similar candidates to gain insights into the CO_2 activation mechanism. In most of AP-XPS investigations, the high binding energy component is addressed to carbonates CO_3 features [92, 93]. In this context, it is assumed that CO_2 activation proceeds via a dissociative reaction that drives the formation of carbonates according to [92]

$$CO_{2_{(g)}} \rightarrow CO_g + O_{chem}$$
 (6.2)

$$CO_{2_{(g)}} + O_{chem} \rightarrow CO_{3_{(ads)}} \tag{6.3}$$

However, there are some tricky points to be disclosed. First, CO_2 weakly interacts with late transition metal atoms as zinc [94]. Secondly, this reaction presumes CO_2 molecules undergo full dissociation, which is not necessarily true when interacting with defective catalyst surfaces. Instead, a charge transfer between the molecule and some active sites derived from defects might take place, giving rise to an intermediate dissociation [95]. In this context, we might spec-

ulate that oxygen from CO_2 interacts with zinc, which might lead to a partial oxidation of the ZnS surfaces, giving rise to the $CO_2^{\delta-}$ intermediate. Indeed, there are some species features that support our hypothesis. In particular, the shift of Zn 2p components after evacuation and the shoulder at higher binding energy of C 1s component under operando conditions. Regarding the first point, as we discussed in a previous work, the oxidation of ZnS surfaces leads to a core-level shift toward low binding energy after the reaction (i.e, after the system reaches its equilibrium). Notably, Zn 2p and S 2p are slightly shifted toward low binding energy after the CO_2 reaction (see SI). Moreover, we obtained two oxygen components, which are assigned to oxygen bonding to zinc at 531 eV and hydroxyl species that form after the reaction at 531.8 eV (See SI). This hydroxyl fingerprint is also detectable in the C 1s spectrum after evacuation (SI)[91]. Regarding the second point, the intermediate $CO_2^{\delta-}$ highlights the CO_2 activation mechanism. The reaction pathway is quite similar to the one described by Eq.(1), giving rise to a small oxygen contribution. The main difference is that the $CO_2^{\delta-}$ intermediate decomposes onto ZnS surfaces, rather than CO_2 molecules themselves, as occurs on Cu (111) surfaces [95, 96]. If we find carbonate species as well, we might speculate in a further step reaction as stated in eq.(2), yielding carbonate species as well. It is worth noting that although such interaction between adsorbate and substrate does occur, this charge transfer itself is not enough to promote the formation of a full zinc oxide layer. For this reason, we claim the CO_2 activation mechanism is a partial oxidation of ZnS, rather than a full CO_2 dissociation. Interestingly, as we recently discussed, ZnS surface oxidation tends to increase as long as more oxygen species enter the ZnS lattice, giving rise to a thin ZnO layer. Notably, when the oxidation saturates, the ZnS's Zn LMM drastically changes, becoming more ZnO-like [71]. Nevertheless, it will be not possible to get a full ZnO/ZnS interface by oxidizing ZnS via CO_2 , because the oxidative power of that molecule is much lower than O_2 [92] Indeed, the Zn LMM does not changed after the CO_2 adsorption on ZnS (See SI of the full paper)

Insights into the influence of CO_2 coverage on the adsorption process were obtained by comparing the system's behavior under different CO_2 dosing conditions. As previously discussed, the surface was initially exposed to 0.55 mbar of CO_2 . To evaluate the role of pressure, we then repeated the experiment under lower CO_2 exposure (0.1 mbar) while maintaining the system at the previously identified optimal temperature of 573 K. Fig. 6.2 compares the CO₂ adsorption features observed after reaction in both scenarios. The CO₂ fingerprint—a characteristic high-binding-energy C 1s component—appears narrower at low pressure compared to the broader contribution observed under operando conditions. Nonetheless, this feature remains detectable even under ultra-high vacuum (UHV) and without additional heating, consistent with a physisorption mechanism in which CO_2 molecules weakly interact with the ZnS surface. In this context, CO₂ molecules adsorbed during the reaction likely desorb when the gas is pumped down. The residual CO_2 , at low surface coverage, still interacts weakly with defective ZnS sites, giving rise to a small but measurable spectral contribution. The relative atomic concentration of each C 1s component is shown in Fig.6.2(b). These results indicate that CO_2 pressure does not play a dominant role in enhancing adsorption. Although a higher CO_2 pressure (0.55 mbar) leads to a slight increase in the CO_2 signal, it is followed by a substantial rise in the C–O(H) contribution. Specifically, after exposure to 0.1 mbar of CO_2 , the C–O(H) peak accounts for only 6.44 % of the total C 1s area, whereas after exposure to 0.55 mbar, this component increases to over 26 %. Based on

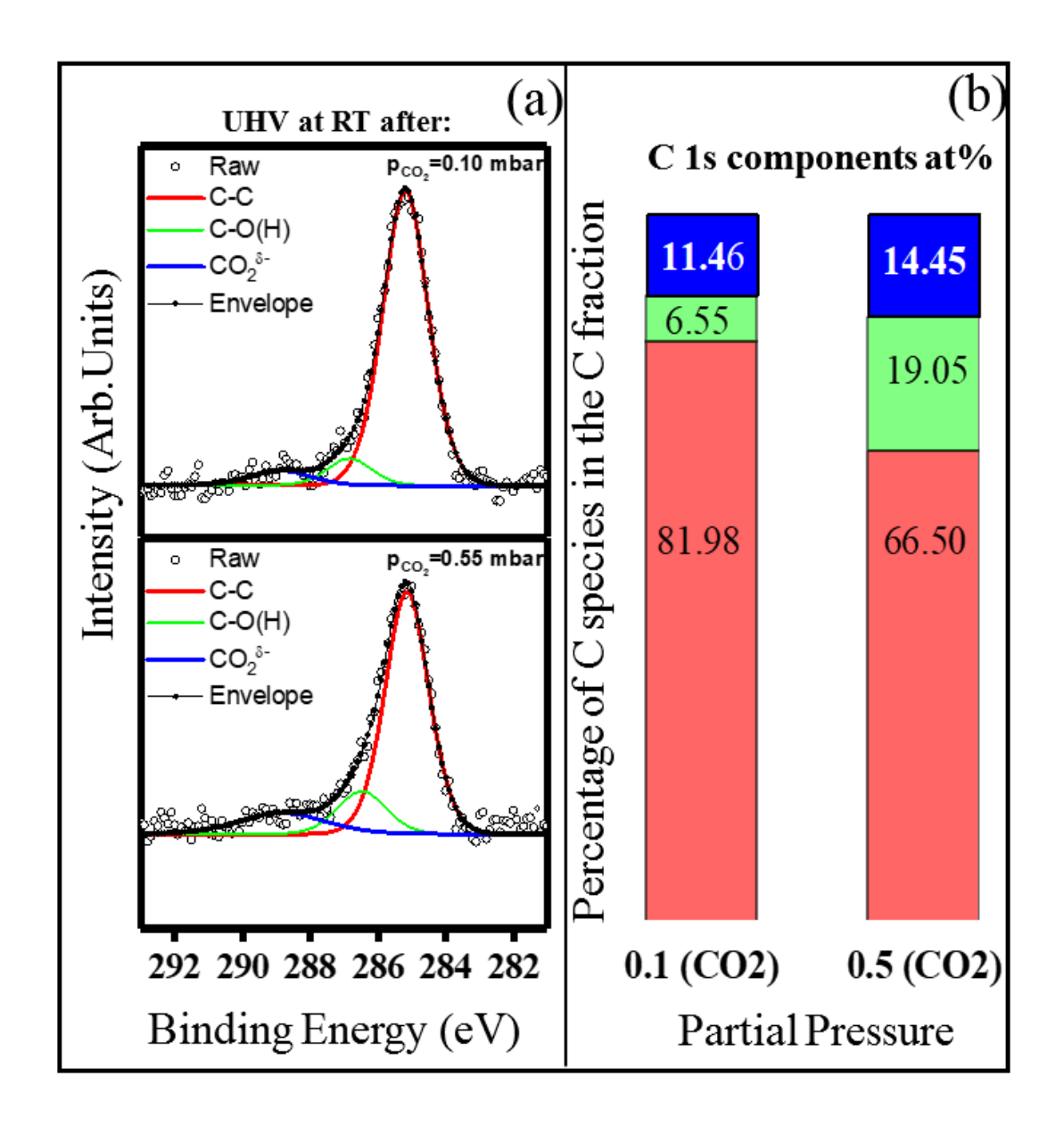


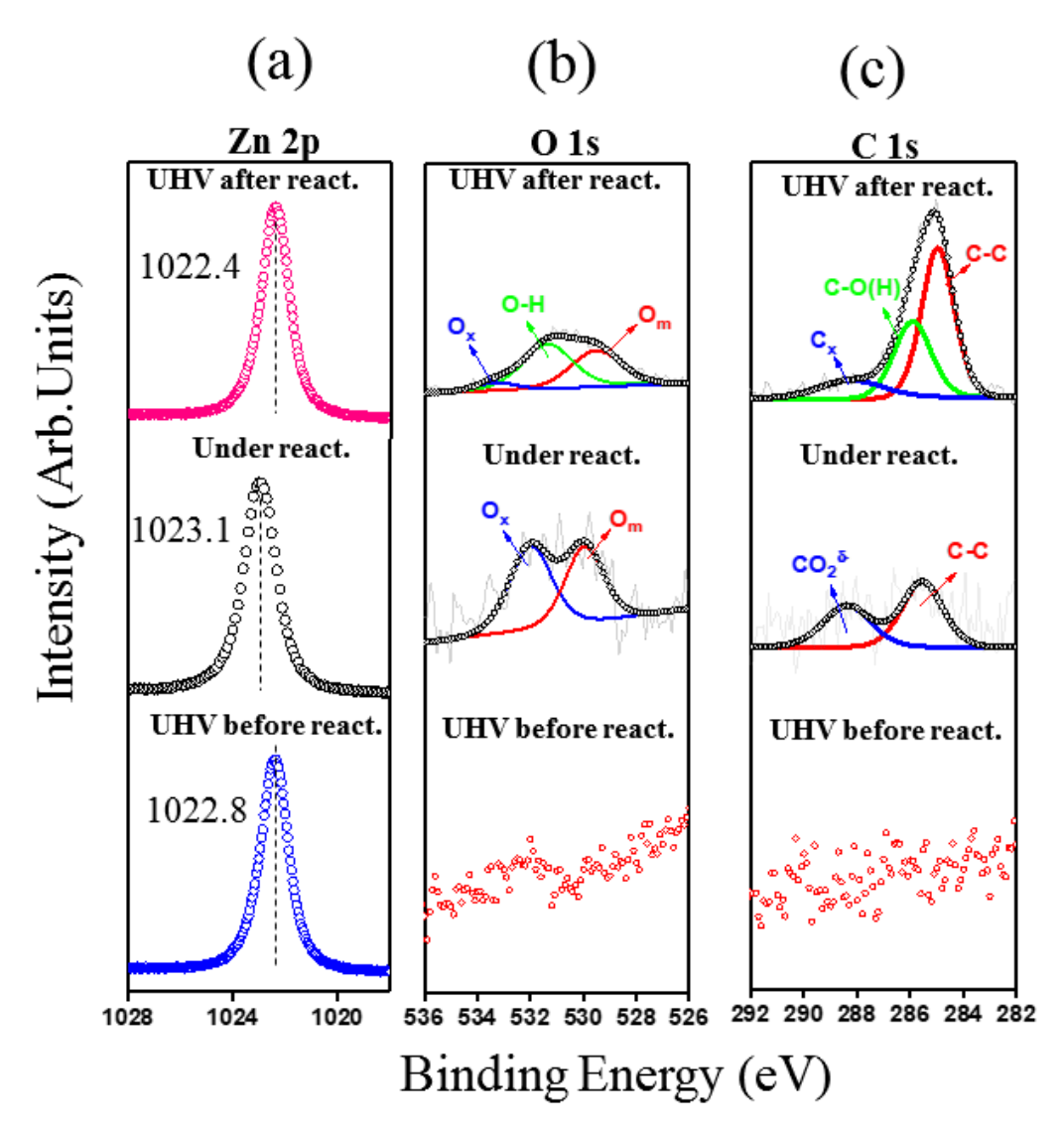
Figure 6.2: (a) C 1s components after NAP experiments at 0.55 mbar (top panel) and 0.1 mbar (bottom panel) of CO_2 ; (b) C 1s components relative concentration as a function of the pressure of CO_2 used in the experiments. In all cases, the sample was heated at 573 K. .

these findings, we selected 0.1 mbar of CO_2 at 573 K as the optimal target pressure and temperature conditions for CO_2 adsorption studies on ZnS surfaces, balancing effective activation with minimal impurity contributions.

Mixing atmosphere: CO_2 + CO

The mixture of CO_2 and other gases is a promising strategy for increasing the number of active sites, which might improve the CO_2 adsorption efficiency. In this regard, CO is a good candidate, since it is known to modify surfaces, either by introducing new vacancy sites by extracting one anionic atom or changing the oxidation of metals [97]. In this section we explore the effect of mixing CO_2 and CO (0.1 mbar each) in the defective ZnS surface.

Inspired by past innovative works that overlooked the traditional metalsensitive probe characteristic of CO, we explore its potential as an agent for restructuring catalyst surface [98]. In this scenario Fig. 6.3 displays the core level peaks of ZnS before, during, and after heating the system at 573 K in a combined CO and CO_2 atmosphere. The Zn $2p_{3/2}$ depicted in Fig.6.3 (a) shifts as a function of the reaction status: Under UHV, before the reaction, it lies at 1022.8 ev, as expected in ZnS systems [38, 46]. During the reaction (Fig. 6.3 (a) middle panel), it shifts toward high binding energy. Ending, after the reaction ((Fig. 6.3 (a) top panel), the component is slightly shifted toward low B.E, lying at 1022.6 eV. As discussed in the last section, changes in the core level B.E. suggest changes in the chemical environment resulting from the adsorption of foreign species in the system. In our context, it is strictly related to CO_2 interacting with ZnS surfaces. The shift toward high binding energy at operando conditions highlights the reaction between adsorbates and the catalyst's surface. The final shift after the reaction, on the other hand, reveals the final equilibrium configuration. In particular, this amount of shift is consistent with an initial oxidation of ZnS surfaces [71]. In this context, sulfate species are not expected, even after the reaction, due to their volatility [71]. These features suggest the defective ZnS surface was



React.: $p_{C0_2} = p_{co} = 0.1 \, mbar$. T= 573 K

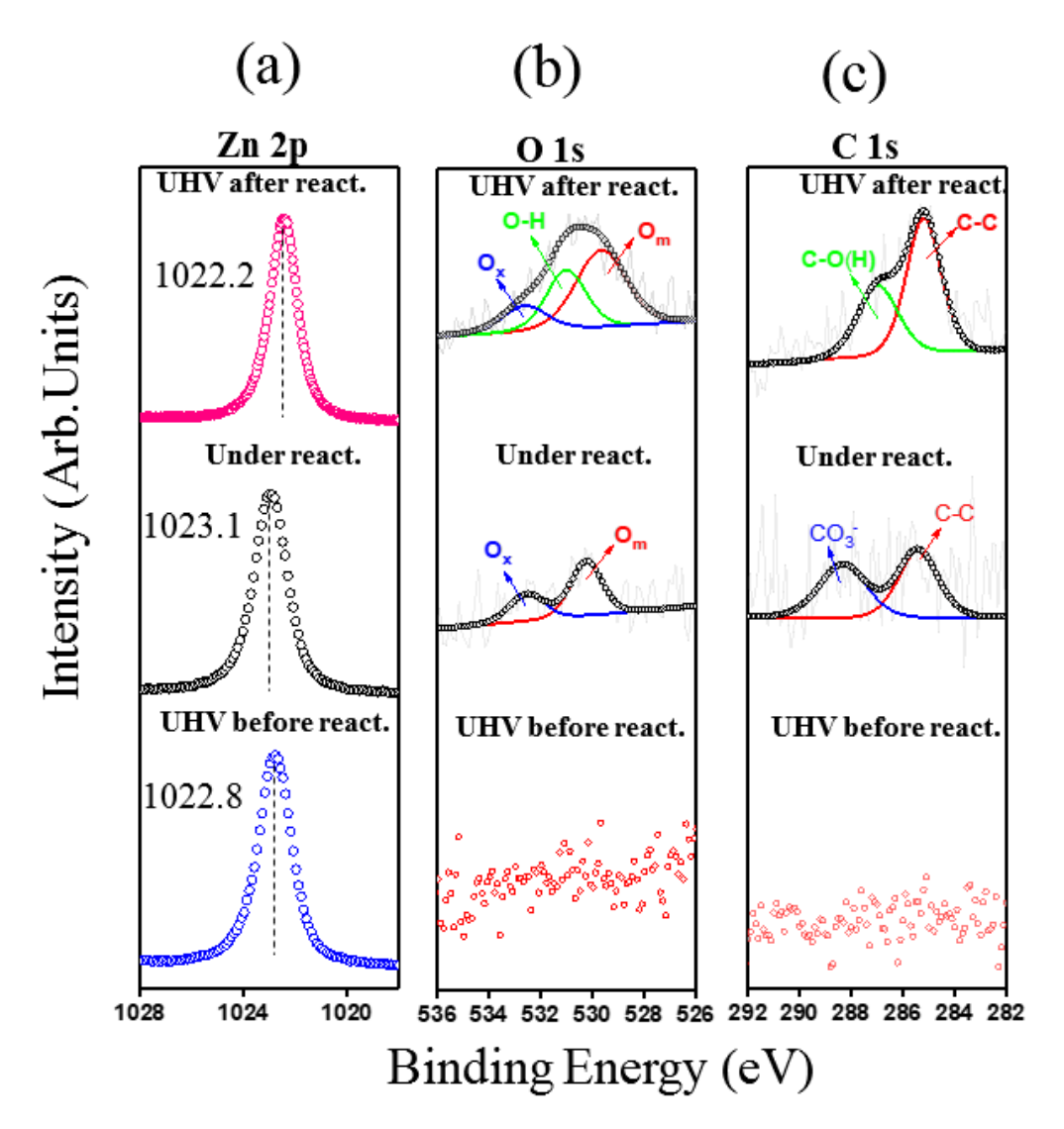
Figure 6.3: Zn 2p (left panel) and C 1s (right panel) of ZnS after a reaction in a mixed $CO+CO_2$ atmosphere (a) at 573 K and (b) 673 K The spectra called "before" means the system right before start the AP-XPS experiments, while the label "After" stands for spectra collected after AP XPS experiments, at room temperature.

activated by the mixed CO_2 and CO atmosphere. This hypothesis is well highlighted by analyzing the O 1s and C 1s peaks in the same scenarios mentioned

before, as shown in Fig.6.3 (b) and (c), respectively. Before the reaction, there are no signals of carbon or oxygen species. This aspect changes significantly under operando conditions. During the reaction (Fig.6.3 (b) middle panel), the O 1s component is well fitted by two oxygen species, highlighting the increase of the oxidative capability under a mixed CO_2+CO atmosphere. The component at low binding energy, at 531 eV, is addressed to the interaction of oxygen with metal atoms, denoted as O_m . The high binding energy component at 532.8 eV, denoted by O_x , represents oxygen species in a dative-bonding configuration [74]. This contribution is either related to the formation of CO_3 or the partial oxidation of ZnS through the $CO_2^{\delta-}$ activated species. At first glance, these values seem higher than the previous investigations regarding CO_2 fingerprint on Catalyst surfaces. However, it is worth considering nothing but the relative position of the intermediate species rather than the absolute binding energies. Given the chemisorbed component in the O 1s peak, usually addressed to oxygen close to metal catalyst, activated CO₂ fingerprints arise 1.8 eV at higher binding energies, while carbonate features arise 2.2 eV offset [95]. In our case, the two oxygen components separation is 1.9 eV, indicating the $CO_2^{\delta-}$ intermediate nature of the peak. After the reaction (Fig.6.3 (b) top panel), a new component related to O-H group is obtained, due to the desorption of water molecules from the chamber. In this scenario, the O_x component is slightly shifted toward high binding energy, likely due to the interaction with further hydrogen atoms from the C_x species obtained after evacuation. More information on the reaction mechanism is obtained by analyzing the C 1s peak, as shown in Fig.6.3 (c). Under reaction conditions, it is well fitted by two components, one at 285 eV addressed to C-C bonds and a high-binding energy one at 288.6 eV attributed to the activated CO_2 intermediate species. These components are essentially the same as those

obtained by exposing the catalyst surfaces to a CO_2 atmosphere alone, as discussed in the past section. The main difference in this mixed condition is the overall contribution of the activated species. While $CO_2^{\delta-}$ accounts for 24 per cent of the total C 1s area in a CO_2 atmosphere, it is responsible for 42.61 per cent in a mixed CO_2 + CO atmosphere. As long as the total pressure does not play a key role in the CO_2 activation, we might relate that improvement to the presence of further oxidative molecules, as CO. Although CO species are not expected to dissociate at ZnS surfaces, they might improve the activation of zinc atoms close to defect sites, partially changing their chemical state, introducing new active sites, or even promoting sub-surface zinc atoms to the top surface [98, 97], leading to an improved CO_2 activation. In this scenario, CO_2 molecules could also anchor close to oxygen species from CO, forming CO_3^- intermediates, which are also located around the 289-289.5 region [93, 95]. However, we are not able to disclose whether both species are contributing in this scenario. Following our fitting procedure, we decovoluted the C 1s shoulder in a unique component at 288.7 eV, which is likely addressed to $CO_2^{\delta-}$. Alternatively, we could speculate that if only activated $CO_2^{\delta-}$ species were present, the contribution of remaining C_x species obtained after evacuation would be higher, since there were more activated species available for recombination. Although these species are indeed observed after the reaction, as shown in Fig.6.3 (c) (top panel), the contribution of this component is only 21.98 per cent of the total C 1s area. Therefore, we might speculate the higher activation component area observed during the reaction was likely driven by the formation of both activated CO_2 species and carbonate CO₃ intermediates. The last component is unstable and might desorb after the reaction, explaining why the final contribution after the reaction is as similar as post the reaction with CO_2 alone.

6.3.3 Mixing atmosphere: $CO_2 + O_2$



React.: $p_{C0_2} = p_{O_2} = 0.1 \, mbar$. T= 573 K

Figure 6.4: Zn 2p (a) C 1s (b) and (c) O 1s components before (bottom panel) and after (top panel) AP XPS experiments in a mixed environment of O_2 and CO_2 . All the spectra were collected at Room temperature. In these experiments, the sample was heated up to 573 K.

To disclose the formation of activated CO_2 , CO_3 or both species in the CO_2

adsorption on ZnS surface, we heated up the system at 573 K in a $CO_2 + O_2$ environment. Given that oxygen atoms display a higher oxidative capability than CO_2 , the formation of a highly oxidized ZnS surface was expected, leaving CO_2 species to anchor on oxygen sites, forming CO_3 intermediates.

Fig.6.4 (a) displays the Zn $2p_{3/2}$ Core level component before, during, and after exposing the system to a combined CO_2 and O_2 environment. Similar features regarding the surface reactivity were found: While during the reaction (Fig.6.4 (a) middle panel), the component is slightly shifted by 0.2 eV toward high binding energy with respect to the peak before the reaction (Fig.6.4 (a) top panel), it is shifted by 0.6 eV toward low binding energy after evacuation (top panel). This amount of shift after evacuation indicates the ZnS surface was highly oxidized, likely due to the presence of oxygen species. Indeed, due to both surface and electronic similarity of sulfur and oxygen species, oxygen atoms can be readily adsorbed on ZnS surface by occupying some surface sulfur sites. This straight oxidation via oxygen species seems more efficient than both CO_2 and CO_2 + CO atmosphere. The O 1s analysis displayed in Fig.6.4 (b) highlights this hypothesis. The sample before reaction does not feature any trace of oxygen species. On the other hand, under reaction, there are two notable oxygen components, at 531.3 eV and 533 eV, attributed to oxygen binding to zinc and dative-bonded oxygen species. These characteristics are very similar to those observed under the mixing of CO_2 and CO. However, the relative contribution of each species is quite different. Especially the O_x component, which is responsible for 30 per cent of the total O 1s signal in the mixed CO_2 + O_2 atmosphere, 12 percent higher than in the case of a CO_2 + CO counterpart. The increase of that contribution might be addressed to the full dissociation of oxygen species, which indeed display a higher oxidative capability than CO2

molecules [99]. After evacuation, besides the persistence of those components, an O-H group derived from the interaction of oxygen species with the desorbed water molecules after the reaction can be observed. As discussed, O_x species are slightly shifted toward high binding energy in this scenario, likely due to the interaction with further hydrogen species, besides metal and carbon atoms. In this context, it is expected that the formation of a highly oxidized ZnS surface could lead CO_2 species to anchor on oxygen sites in a co-adsorption mechanism rather than a straight interaction with metal species. This design is favorable for the formation of $CO3^-$ species, as revealed in the C 1s peak analysis shown in Fig.6.4 (c). The flat line C 1s signal before the reaction is converted into an envelope that is deconvoluted into two main components under operando conditions: C-C species at 285.2 eV and a satellite peak at 289.3 eV. In the previous sections, we denoted the satellite component by $CO_2^{\delta-}$. However, since the interaction between oxygen and ZnS ($O_2 \rightarrow 2~O_{ads}$ proceeds faster than the interaction between CO_2 and ZnS, we might speculate that the interaction of CO_2 and the catalyst surface is mediated by oxygen species derived from the oxygen dissociation. Therefore, the satellite peak is most likely a *CO*3⁻-like component. Furthermore, the offset between the sp^3 carbon and the intermediate species is higher than 3 eV, which is the typical value for addressing the C 1s shoulder to CO2 activated species. Also, even the absolute binding energy is in good agreement with previous investigations that reported the formation of CO^3 carbonate species. Indeed, the oxidation of ZnS via oxygen adsorption does not form a full ZnO layer [71], which could completely hinder the charge transfer from CO_2 to zinc atoms. However, the vast majority of the available active sites are likely from adsorbed oxygen species. Therefore, although the presence of further $CO_2^{\delta-}$ components cannot be ruled out, their contribution to that region,

if it exists, would be almost negligible. This speculation is emphasized by the lack of C_x species after evacuation, as depicted in the top panel of Fig.6.4 (c). As discussed, $CO3^-$ species are unstable and likely desorb from the surface. If some activated CO_2 species were present, a minor though negligible C_x feature would be detected after reaction. Therefore, we might speculate that $CO_2 + O_2$ is favorable for $CO3^-$ formation.

DFT modeling

Modeling the CO_2 interaction with ZnS surfaces

To gain insights into the adsorption mechanism of CO_2 on ZnS surfaces, we investigated both the geometric and energetic aspects of CO_2 interaction with pristine and defective ZnS (001) surfaces, as illustrated in Fig.6.5. Our models considered a sulfur-terminated ZnS (001) surface under sulfur-rich conditions, in line with experimental preparation protocols. This polar surface is characterized by sulfur segregation at the outermost atomic layers, while the subsurface Zn atoms exhibit slight inward displacements upon structural relaxation.

For the relaxed pristine structure, the vertical Zn–S bond distance at the top-most layer ($d(Zn^{top} - S^{top})$) is 2.45 Å, and the lateral S–S distance between neighboring surface sulfur atoms is 2.17 Å. A CO_2 molecule, initially placed in its linear geometry (180°), was positioned atop the surface with its molecular axis perpendicular to the slab - Fig.6.5 (a). Upon optimization, no significant interaction between CO_2 and the pristine ZnS surface was observed, as noted in Fig.6.5 (b). The adsorption energy was calculated to be –0.07 eV, indicating a thermodynamically favorable yet extremely weak interaction. Notably the distances

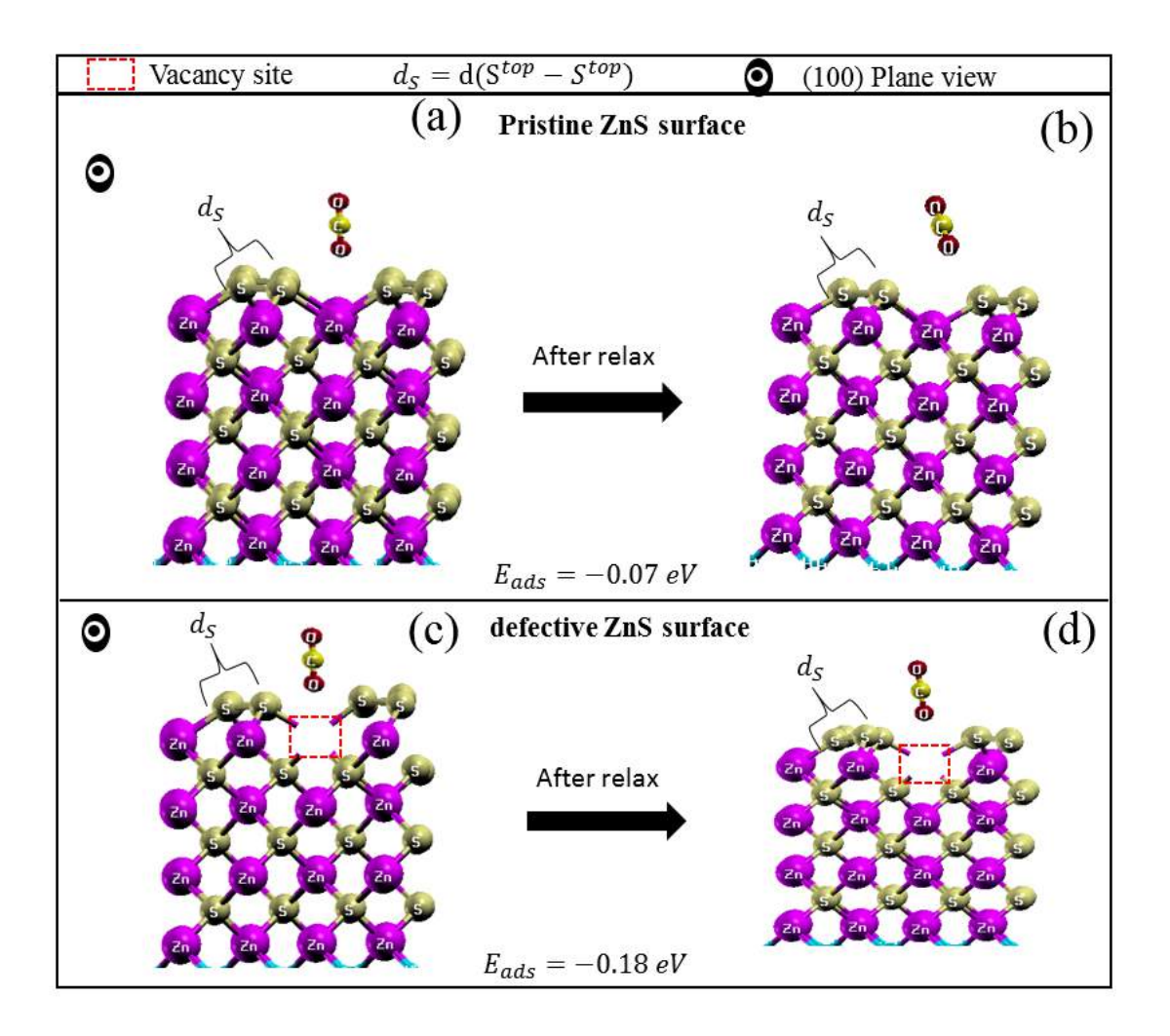


Figure 6.5: DFT modeling of ZnS pristine (a),(b), and doped (c),(d) before (left panel) and after (right panel) interacting with CO_2 .

between outer most zinc and sulfur species - $d(Zn^{top} - S^{top})$ $d(S^{top} S^{top})$, respectively, distances were not disturbed, and the CO_2 molecule geometry remained nearly linear, slightly bending to 179.5°, suggesting minimal polarization. This negligible structural and electronic perturbation supports the view that pristine polar ZnS surfaces are chemically inert to CO_2 , in agreement with prior studies reporting low reactivity of stoichiometric II–VI semiconductors toward closed-shell molecules [100].

To explore the effect of native point defects on reactivity, we introduced a zinc vacancy (V_{Zn}) at the surface, which has been previously identified as the most thermodynamically stable defect under S-rich conditions [46]. Upon removal of one Zn surface atom, as shown in 6.5 (c)-(d), the surrounding sulfur atoms undergo localized relaxation. The distance between zinc and sulfur atoms in the vicinity of the vacancy slightly increases to 2.47 Å, reflecting an outward displacement and increased local sulfur density. Interestingly, upon exposure to CO_2 , this bond length further extends to 2.48 Å, while the lateral S-S distance slightly contracts from 2.14 Å to 2.13 Å. These subtle though measurable relaxations imply a localized surface reconstruction in the presence of CO_2 , likely induced by the altered electronic environment near the vacancy. The adsorption energy of CO_2 on the Zn-deficient surface was found to be -0.18 eV, noticeably more negative than on the pristine surface. This finding suggests the CO_2 adsorption on Zns is thermodynamically favorable in a zinc-deficient scenario. The enhanced interaction suggests that zinc vacancies promote partial activation of CO_2 , possibly through electrostatic mild charge transfer. Such behavior is consistent with literature showing that vacancy sites can serve as electron donors or centers of surface polarization, facilitating interactions with electrophilic molecules like CO_2 .

The overall results derived from this simulation highlight that CO_2 interaction with pristine polar ZnS surface is very unlikely, while it might take place in the presence of native defects like zinc vacancies, via a weak van der Waals interaction, which agrees very well with the experimental results derived from AP-XPS. This weak interaction confirms the hypothesis that CO_2 undergoes partial activation on ZnS rather than a full dissociation. Given the poor oxidative capability of CO_2 compared to oxygen molecules, the CO_2 activation might be

mitigated when mixing both atmospheres. This trend will be discussed next through modeling the oxygen adsorption on the same ZnS surfaces.

Modeling O_2 adsorption

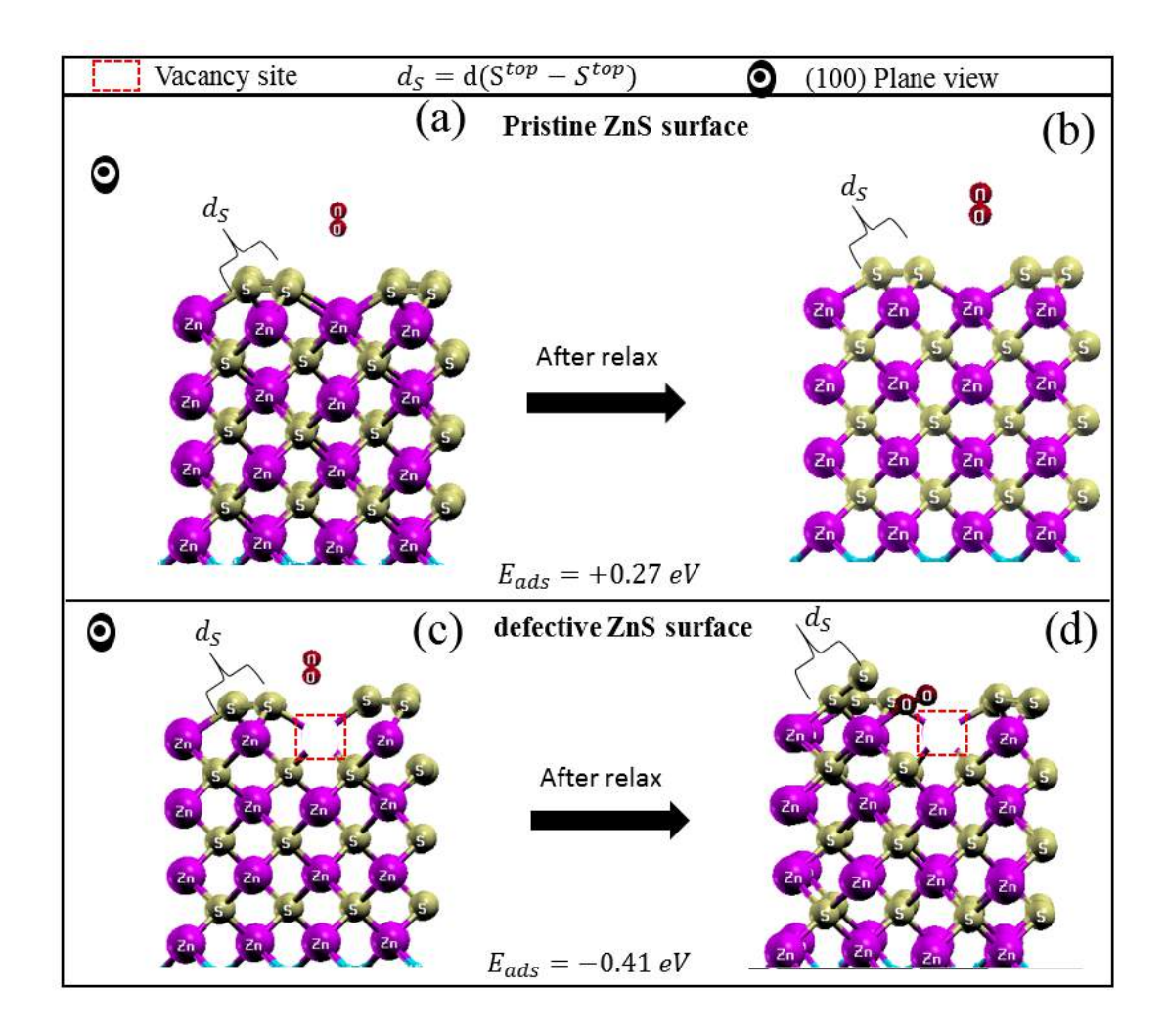


Figure 6.6: DFT modeling of ZnS pristine (a),(b), and doped (c),(d) before (left panel) and after (right panel) interacting with O_2 .

We turn our attention to the interaction of oxygen and ZnS surfaces. The adsorption process was modeled by placing an oxygen molecule upward to the ZnS slab, positioned close to the outermost zinc atom. The optimized oxygen

d(O-O) is 1.23 Å, in good agreement with previously results [101, 102]. Fig.6.6 (a)-(b) illustrates the structural features of oxygen adsorption on the defect-free ZnS (001) surface. As discussed in the past section, before reaction, the top layer sulfur atoms are separated by 2.17 Å, while the Zn-S distance is 2.45 Å. The Zn-Zn separation between adjacent zinc atoms is 3.84 Å, in good agreement with our previous simulation [38]. The main bond-length modification after relaxing the system was noted in the d(O-O) separation, which was elongated to 1.25 Å. These findings would suggest that oxygen might react even with defect-free ZnS surfaces. However, one can note the quite high adsorption energy $E_{ads_{O_2}} = +0.27eV$. Therefore, oxygen adsorption on defect-free ZnS is in fact an endothermic process, which is not thermodynamically favorable.

The scenario is dramatically changed in the presence of a zinc vacancy, as revealed by Fig.6.6(c)-(d). Although d(Zn-S) remains similar to that of the pristine surface, the $d(S^{top}-S^{top})$ decrease by 0.07 Å . This contraction is indicative of a localized sulfur segregation driven by the relaxation of surface atoms near the vacancy site. In addition, the d(O-O) increases to 1.32 Å. This increase is often addressed to a dissociative chemisorption mechanism [103]. As noted in Fig. 6.6 (d), the oxygen molecule indeed sticks on the ZnS surface with a lower adsorption energy - $E_{ads} = -0.41 \ eV$. This fact explains why oxygen atoms are readily adsorbed on defective ZnS, as we observed experimentally. The mechanism behind such a chemisorption is explained as follows: 1) Sulfur atoms close to the vacancy sites move upward to the ZnS surface, breaking or weakening their bonds with neighboring Zn atoms. This structural rearrangement leads to the reduction of $d(S^{top}-S^{top})$); 2) Next, the oxygen molecule is tilted, shifting laterally to interact with an uncoordinated Zn atom near vacancy sites. This helps for compensating the dangling bond created by sulfur displacement, leading to

a polarized O_2 configuration with an extended O-O distance. At this energetically favorable configuration, the bond strength is likely reduced compared to molecular O_2 species, which suggests oxygen might undergo dissociation depending on the particular environment that they will be subjected to. Once all DFT calculations were carried out at 0 K and without the presence of further adsorbate, we were not able to visualize the full dissociation of the chemisorbed oxygen species, which likely takes place by heating the system at 573 K as experimentally suggested.

6.3.4 CO oxidation

Stoichiometric X Oxygen-rich environment

One key catalytic reaction is the CO oxidation. This reaction can produce CO_2 activated species that can be reused in a green-friendly reaction like the Methanol synthesis process. To gain insight into the CO oxidation process on defective ZnS surfaces, we exposed the system to two distinct mixed CO + O_2 environments: a stoichiometric and an oxygen-rich atmosphere. Fig.6.7 displays the XPS spectra after the exposure of ZnS to stoichiometric conditions ($P_{O_2} = P_{CO} = 0.1 mbar$). Before the reaction, Zn 2p was found at 1022.8 eV, and no carbon or oxygen-related features were observed. Following exposure to the gas mixture, the Zn 2p B.E is slightly shifted toward lower values, lying at 1022.6 eV, as shown in Fig.6.7 (a). As discussed in this chapter, this B.E shift is roughly related to modifications in the chemical environment of the catalyst. the formation of CO_2 would be expected to manifest as a C 1s component near 288 eV. However, as shown in Fig.6.7 (b), the C 1s peak is well fitted by two

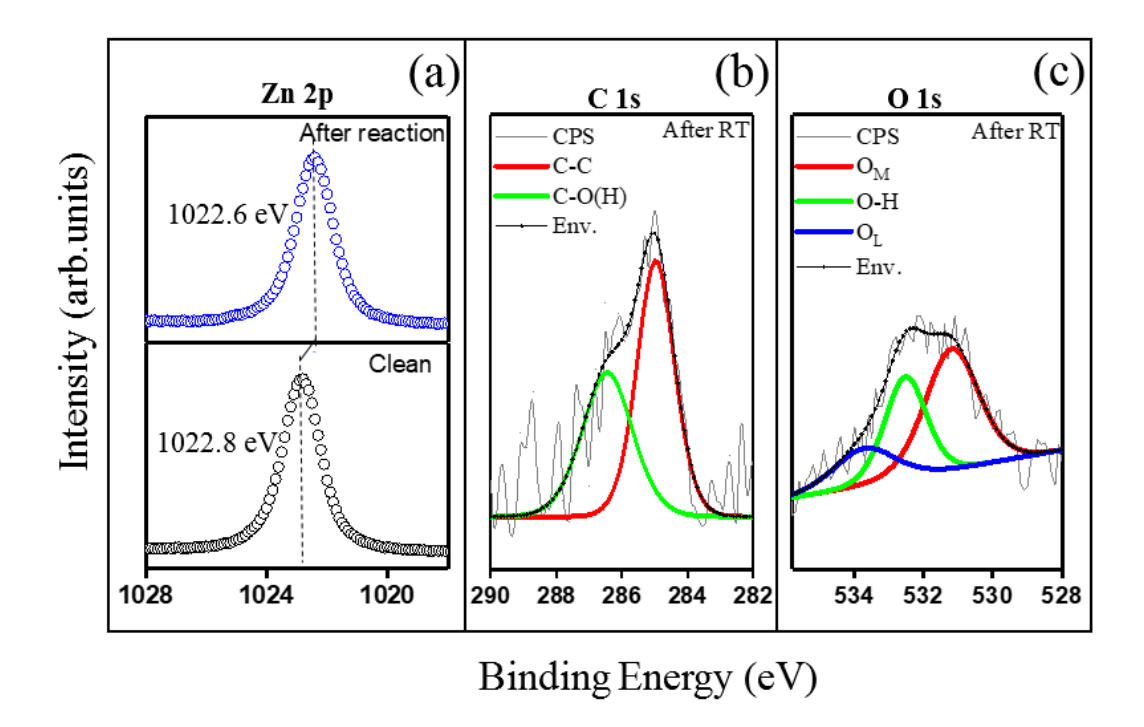


Figure 6.7: Zn 2p (a), C 1s (b), and O 1s(c) before (bottom panel) and after (top panel) AP-XPS experiments in a stoichiometric CO + O_2 atmosphere. During the experiments, the samples were heated at 573 K. All the spectra were collected at room temperature.

components, one at 285 eV, related to sp^3 carbon, and another at 287 eV most likely linked to C-O(H) species that desorb from the chamber to the sample surface after the AP experiment. The absence of the CO_2 fingerprint suggests that the surface reactivity of CO surface reactivity under stoichiometric conditions is negligible. On the other hand, the oxidation of ZnS surface is still taking place, as noted in Fig.6.7 (c). The oxygen component is described by three components: The O_m , at 531 eV, related to oxygen-Metal bond, the O-H at 532 eV, well aligned with the existence of O-H groups as suggested from C 1s spectrum, and a last component at 533 eV, which is labeled as chemisorbed oxygen in the lattice (O_L) in a bridge site. This bridge is likely occurring between zinc and another oxygen atom. Therefore, we might suppose the oxygen molecule sticks as an O_2

structure rather than a dissociated oxygen.

The oxygen atoms that diffuse through the ZnS surface might occupy the active sites derived from the formation of cation defects on the ZnS surface. However, instead of what was observed in the mixing of CO_2 and O_2 , there is no competition for these active sites. Indeed we exposed the system to CO only, and we do not obtain any kind of surface reactivity fingerprint (not shown). We suspect the CO interaction with ZnS is unfavorable, independently of the number of active sites. In this scenario, CO molecules can only interact via indirect adsorption, i.e, co-adsorbing onto available oxygen sites. However, this procedure typically depends on the coverage. For some metal catalysts an O_2 rich environment can suppress the formation of CO_2 [104]. On the other hand, metal oxide alloy demands a higher coverage of trapping molecules, like water, that might improve the adsorption of molecules whose interaction on a non-passivated surface was poor. In the case of ZnS, an oxygen-rich atmosphere might pave the way for the CO oxidation process.

Fig.6.8 displays the XPS spectra of ZnS after exposing the system to an O_2 -rich environment ($P_{O_2} = 2P_{CO}$). Similar to the features in the stoichiometric scenario, the core-level Zn 2p component arises slightly shifted toward low binding energy. Compared to the B.E position in the stoichiometric scenario, the Zn 2p component is 0.2 eV shifted toward low binding energy, lying at 1022.4 eV as shown in Fig.6.8 (a). Interestingly, the C 1s component in this case is deconvoluted into three components rather than two as in the last scenario. In addition to the sp^3 and C-O(H) , the CO_2 fingerprint is well highlighted at 288.3 eV, as revealed in Fig.6.8 (b). This result is a strong evidence of the CO oxidation in the defective ZnS surface. The features of the O 1s spectra provide insights on

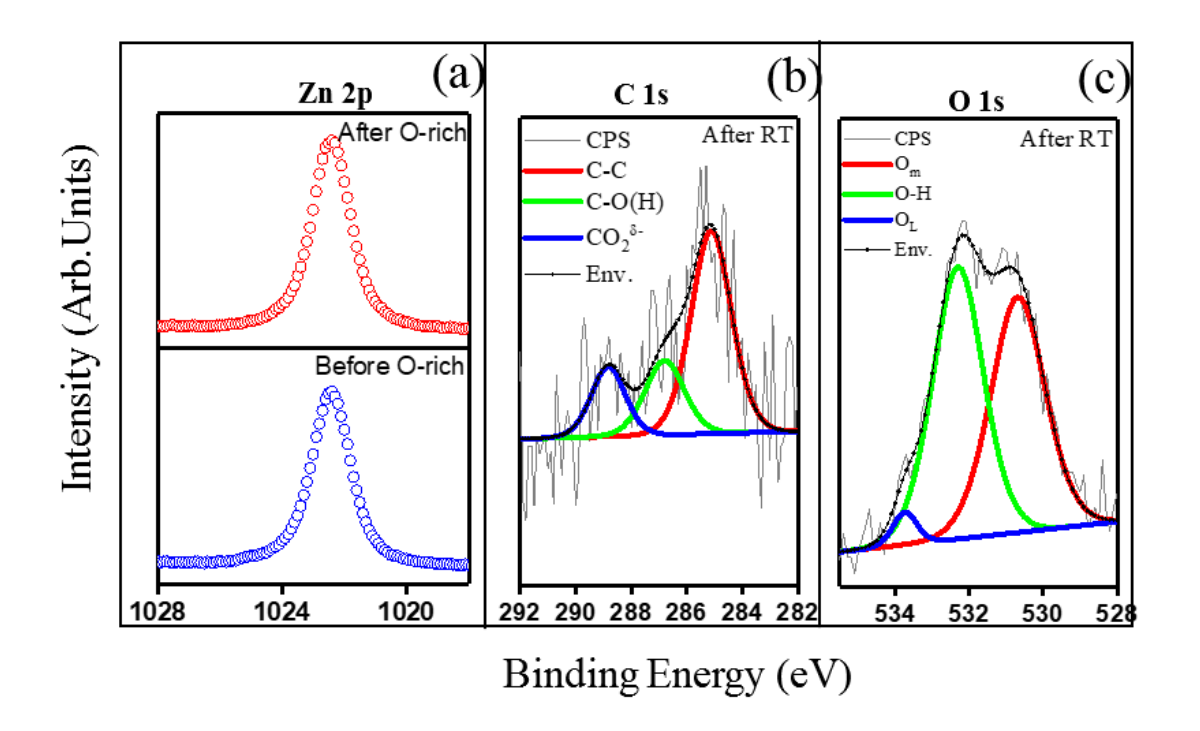


Figure 6.8: Zn 2p (a), C 1s (b), and O 1s(c) before (bottom panel) and after (top panel) AP-XPS experiments in an oxygen-rich CO + O_2 atmosphere. During the experiments, the samples were heated at 573 K. All the spectra were collected at room temperature.

the sites used for reacting CO. Although the spectrum is still fitted with three components (Fig.6.8 (c)) we noted an appreciable decrease in the O_L component. We might suspect that in an oxygen-rich environment, CO molecules co-adsorb onto oxygen bridge sites. One of the oxygen molecules used in the bridge configuration is trapped by CO molecules, leading to a decrease in the O_L components. This hypothesis is well explained with the assistance of DFT calculations, as discussed in the next subsection.

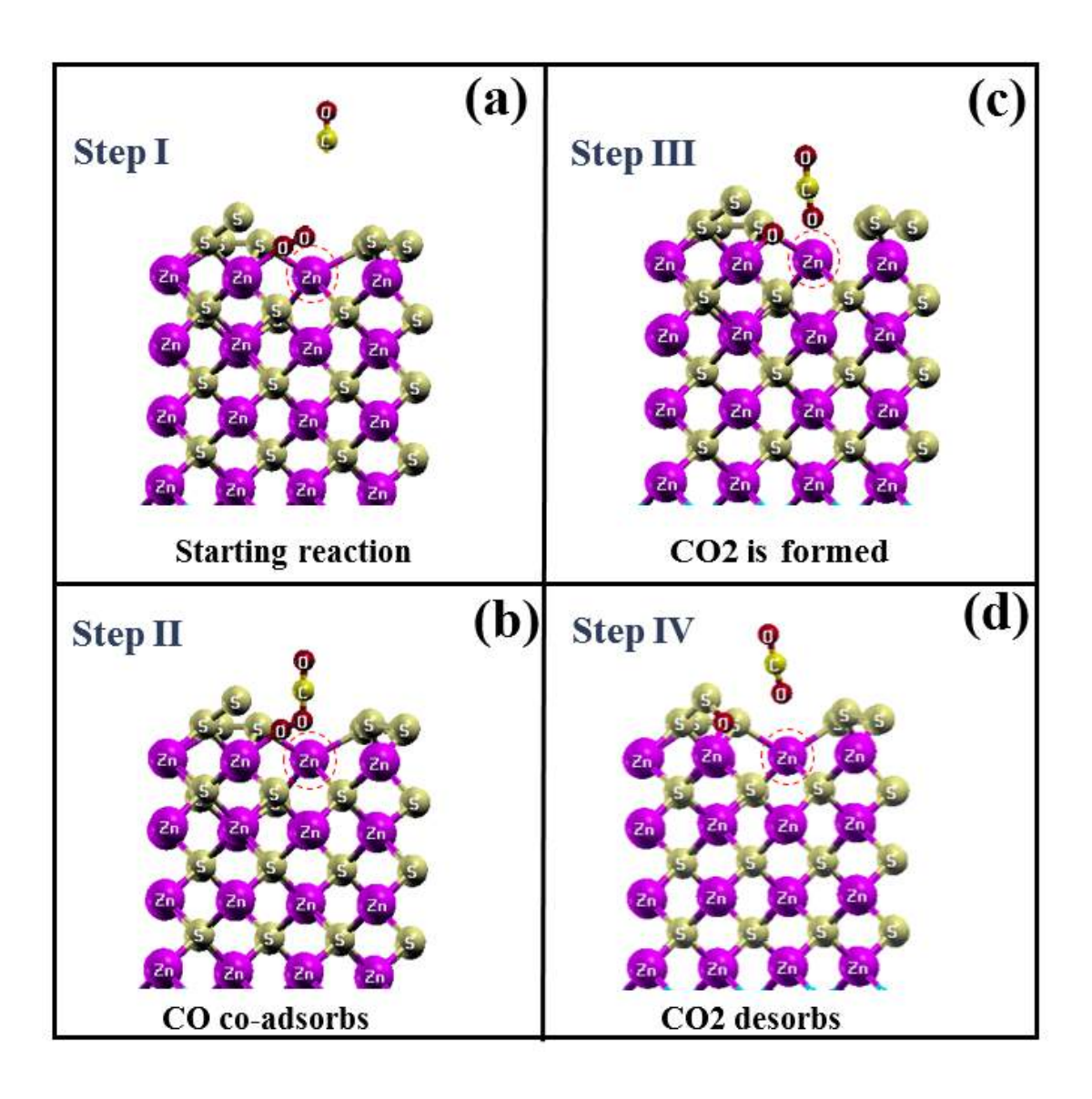


Figure 6.9: DFT model of CO oxidation on ZnS surface

DFT modeling

Insights from the co-adsorption of CO molecules experimentally proposed is derived from a DFT analysis. To model the oxygen-rich scenario, we use a defective ZnS surface with an oxygen molecule weakly chemisorbed, as discussed in the last section. In this scenario, a linear CO molecule vertically aligned is

placed to one of the oxygen already adsorbed on the ZnS surface, as shown in Fig6.9 (a) (step I). The distance of carbon and oxygen of the CO molecule is d(C-O) = 1.16 Å, in good agreement with literature results. After relaxing the whole system, the CO molecule is adsorbed on the oxygen sites, close to the vacancy site, as depicted in Fig6.9 (b) -step II. As we discussed, the distance of adsorbed oxygen atoms has increased after sticking on the defective ZnS (001) surface. This elongation turn the dissociation of such species thermodynamically stable, especially when an atom with higher electroaffinity is available, as in the case of carbon atoms from CO.

This scenario leads to the dissociation of the adsorbed oxygen species. One of the oxygen atoms is trapped by CO, forming the CO_2 molecule, as shown in Fig6.9 (c) - step III. Interestingly, the distance of the trapped oxygen and the oxygen of CO is circa of 2.3 Å, in good agreement with the distance of oxygen atoms in CO_2 . In addition, the distance $d(S^{top} - S^{top})$ increases from 1.99 Å to 2.07 Å, a typical value of defective ZnS before reaction. This scenario seems almost stable, with the resulting CO_2 molecule barely interacting with the ZnS surface. The final relaxation step confirms such a hypothesis. The step IV is shown in Fig6.9 (d). In this, the CO_2 molecules are slightly tilted such that the O-C-O angle becomes 179.86°, nearly linear and even closer to 180° than CO₂ directly exposed to the ZnS surface. In addition, $d(S^{top} - S^{top})$ further increases, reaching 2.08 Å. Notably, the remaining oxygen atom makes a bridge bond between a zinc atom close to the vacancy site and a surface sulfur atom that previously exhibited an extra dangling bond due to the oxidation of the ZnS surface. These findings highlight that the interaction of CO_2 molecule is even weaker if the defective ZnS surface is oxidized, confirming one of the experimental assumptions. Moreover, they explain the decrease in intensity of the O_L peak, observed in XPS measurements. Given that CO molecule is adsorbed on an oxygen site, it will decrease the contribution of the bridged oxygen in the Zn-O-O configuration.

Chapter 7

General Remarks

In this thesis, we explored the role of defects on ZnS surfaces. Motivated by real-world challenges, including demands for cleaner energy and pollution gases control, we aimed to explore the solid-state physics foundations behind all the questions raised by these open issues. Combining traditional surface science techniques and first-principles calculations based on DFT theory, we demonstrated that zinc vacancies (V_{Zn}) are the driving force behind the enhancement of the electronic, optical, and catalytic properties of ZnS systems. Besides stabilizing the system as a p-type semiconductor, V_{Zn} in ZnS increases the number of majority carriers, broadens the absorption and emission range, and introduces new active sites that enable surface reactivity with oxygen-containing molecules such as O_2 , CO, and CO_2 . In the last case in particular, it allowed for the growth of an impurity-free ZnO/ZnS heterostructure, enhanced CO_2 adsorption, and promoted CO oxidation. These improvements position cation doped ZnS-systems as promising candidates for photocatalytic applications.

Appendix A

Further Experimental details

In this chapter, we briefly provide information regarding some of the experimental procedures carried out in this thesis. We hope these parameters will be helpful for reproducing the main results reported in the core of this document

A.1 Sample preparation and description of further experimental techniques

Sample preparation

The ZnS single crystals purchased from Surfacenet gbmh were prepared in situ via several cycles of argon sputtering (E=600 eV, $I_S=5\mu A$, t=5 min) and annealing at different temperatures (up to 1520 K, during 30 min). ZnO

single crystals purchased from Maltech gbmh were prepare in the same way, but with different sputtering and annealing parameters. The sample was chemically etched in a HCl solution several times for short period before introducing it into the vacuum chamber. After that, the surface was in-situ prepared by several cycles of sputtering (E = 1000 eV, $I_S = 7\mu A$, t = 5 min) followed by annealing at 750 K. LEED patten revealing well defined and sharp spots was the criteria for checking the sample cleanliness procedure.

PL experiments

The PL experiments were performed by Dr.Ludiane Lima at CBPF at the Interface's lab. The PL spectra were obtained at room temperature in backscattering geometry using a home-built system equipped with an Andor Shamrock spectrometer within idUS charge-coupled device (CCD) detector. The measurements were obtained using a 488 nm laser with a spot diameter better than 1 μ m, reaching the sample with a power of 0.4 mW. The PL data were fitted by a Voigt function, mixing Gaussian and Lorentzian line shapes

AFM measurements

The AFM measurements were performed by Msc. Igor Coelho at CBPF at the Interface's lab. Ex-situ Atomic Force Microscopy (AFM) measurements were performed using a Bruker Nanoscope V Multimode 8 microscope operating in tapping mode. A silicon probe (NSG50, NT-MDT) with a nominal force constant

of 0.5 *N/m* and a resonance frequency of approximately 150 *kHz* was employed. Both topographic (height) and phase images were simultaneously acquired. The phase signal is extracted by monitoring the phase shift between the cantilever excitation and its oscillation outcome, and provides additional information on local surface properties. All the images were analyzed via the WSxM software [105]. The microscope was enclosed within an acoustic chamber and mounted on a pneumatic anti-vibration stage to prevent noise and micro vibrations from affecting measurement accuracy.

Preparation of a ZnO/ZnS interface

After successively cleaning the ZnS substrate following the sputtering and annealing procedures mentioned above, the sample was exposed to a controlled oxygen atmosphere at about $p_{O_2} = 2.10^-5$ mbar. At the same time, the sample was heated up to 573 K during 60 minutes. During the cooling down, the emission current was slowly decrease in a rate of 0.25 mA/s. The sample was held at the preparation chamber after pumping the gas out. Once room temperature was achieved, the sample was transferred to the XPS analysis chamber and the spectra were collected.

A.2 Relative Atomic concentration - IMFP correction scheme

Although XPS is not a quantitative technique, one can get insights by comparing relative atomic concentration analysis. Yet, some advices to avoid any overestimation are need in this regard. The main source of errors during this procedures lies in the lack of correction when comparing photoelectron that escape from different depths. Even taking into account their relative sensitive factor (R.S.F), traditional XPS software analysis like CasaXPS does not incorporate any correction regarding the IMFP . Instead, they computes the ratio between of each created region- that incorporates the right R.S.F with respect to the total area.

One strategy to correct this method is weight the values obtained through relative area quantification by the respective IMFP of each orbital employed in the analysis. Therefore, given regions A and B, whose IMPF are $IMFP^A$ and $IMFP^B$, the real relative atomic concentration of A with respect to B is given by

$$Real(A \text{ at \%}) = \left[\frac{Old(A \text{ at \%})/IMFP^{A}}{\left(\frac{Old(A \text{ at \%})}{IMFP^{A}}\right) + \left(\frac{Old(B \text{ at \%})}{IMFP^{B}}\right)}\right] \times 100. \tag{A.1}$$

In Eq.A.1 $Old(A \ at \%)$ and $Old(B \ at \%)$ are the relative atomic concentration of A and B, respectively, derived from the software. It can be noted from Eq.A.1, if the portions display same IMFP, no corrections is needed and the value provided by the software will be already accurately. This was our case when comparing S 2p concentrations with respect to Zn 3p.

A.3 Thin film thicker estimation through the Thickogram method

A popular method for estimating the thicker t of a film in XPS experiments is to evaluate the attenuation of the substrate signal I_s with respect to the growth of the overlayer signal I_o such as

$$t = -\lambda \cos(\theta) \ln\left(1 + \frac{I_0/s_0}{I_s/s_s}\right),\tag{A.2}$$

where λ si the inelastic mean free path of the core level signal and θ is the takeoff angle. Although this method works well for thicker and very uniform films, it fails when applied to thicker or non uniform films. The main reason for that inaccurate in these cases is the assumption that either electron escaping from the substrate as those from the film display identical attenuation length.

Indeed, their attenuation length might differ depending on the roughness of the film as well as on their homogeneity itself. Fortunately, in the beginning of the century *Peter Compson* has proposed an innovative method that fill all gaps in this regard [26]. The general idea consist of solving geometrically the following equation:

$$ln\left(\frac{I_0/s_0}{I_s/s_s}\right) - \left[\left(\frac{E_0}{E_s}\right)^{0.75} - 1/2\right] \frac{t}{\lambda_0 \cos \theta} - ln2 = ln \sinh\left(\frac{t}{2\lambda_0 \cos \theta}\right)$$
(A.3)

The general thickogram plot is shown in Fig. A.1. The linear term on the left side of EqA.3 gives the straight line intersection of the thickness scale, which is given by the right side of EqA.3. Given that, the thickness of film is estimated

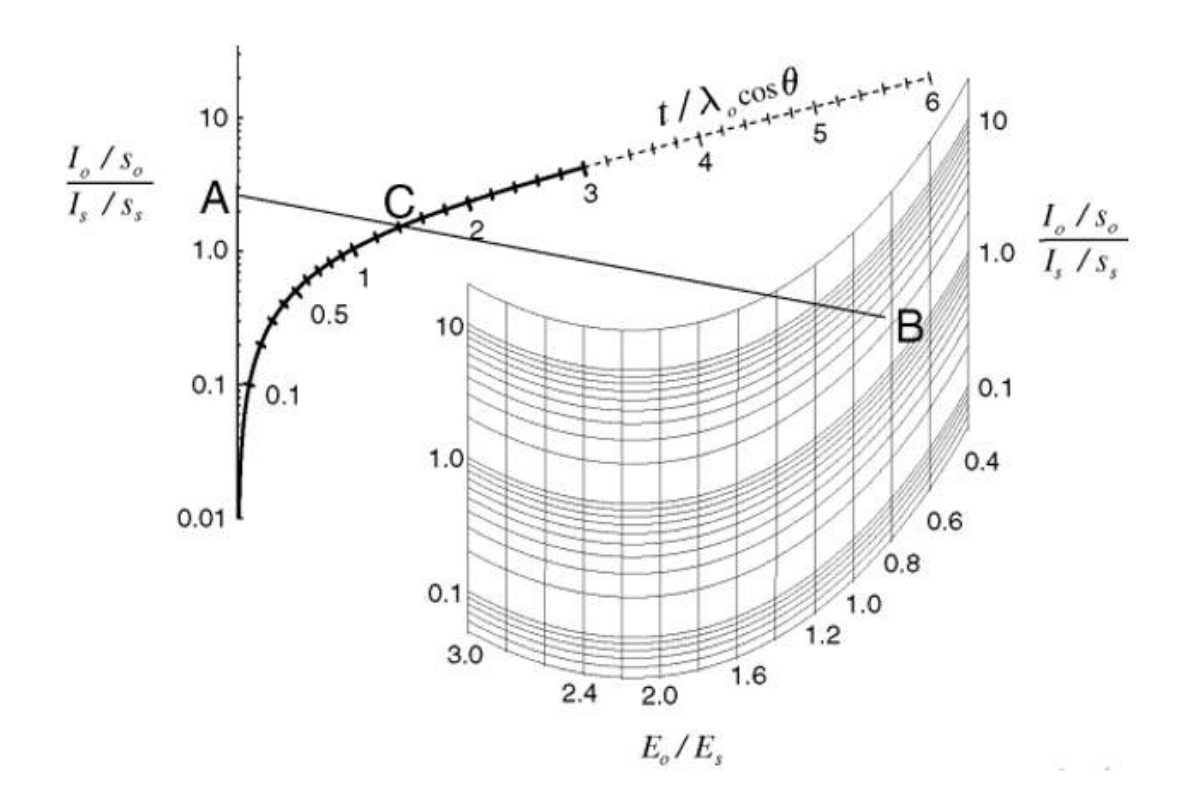


Figure A.1: The thickogram method.

Taken from [26]

by following the follow steps:

- 1. In the axis A, compute the ratio of **peak intensities from overlayer and substrate** I_0 **and** I_s respectively, taking into account their respective sensitive factor
- 2. In axis B, compute the **kinetic energy ratio** $\frac{E_0}{E_s}$ corresponding to the same intensity ratio
- 3. Ending, find the intersection point between A and B in the thickness curve C

It is worth noting the choice of the components for the substrate and over-

layer signal play a dramatic role. In general, high attenuation on the substrate signal peak lead to an overestimation of the film thickness. On the other hand, if the overlayer signal is also present in the substrate, one might undergo in errors when estimating the intensity ratio, leading to underestimation of the film thickness. Therefore, as explained in chapter 6, we choose the Zn 3p and O 1s as signal of substrate and overlayer contributions, since the first is most likely bulk like and thus not varying through the oxidation cycles, and the last is the core level component that comes from the overlayer solely.

A.4 Band gap estimation from XPS

Electrons experience several energy loss mechanisms during their pathway leaving the surface. Some of the most common are related to collective oscillations (bulk bpl and surface spl plasmons) and single-particle excitations ΔE_{SP} . Given that, the general kinetic energy E_K of electrons as follow:

$$E_K = \hbar\omega - E_B - \hbar\omega_{bpl} - \hbar\omega_{spl} - \Delta E_{SP}. \tag{A.4}$$

The loss contribution appear in XPS spectra as broader copies of the core level peaks, at lower kinetic energies. For instance, *bpl* are usually find 20 up to 30 eV away from the main peak - the most intense component in the spectrum. Among all loss mechanism regarding single particle excitations, the jump of electron from the valence band to the conduction band is lowest in energy. It is worth noting that this distance is essentially the band gap of the material. Its contributions will arise at higher binding energies with respect to the main

peak. However its poor signal turn its overall signatures almost negligible. By increasing both the dwell time and number of scans in XPS experiments, one can observe its features through an onset plot of the core main peak, as discussed by *Nichols* and colleagues [84]. Therefore, fixing the center of the main peak E_{center} , we can estimate the band gap by computing the difference of the "zero-level intersection" E_{ZL} and evaluating the difference between these parameters:

$$E_{gap} = E_{ZL} - E_{center} \tag{A.5}$$

It is worth mentioning that this method works even for insulating sample, once it is derived from relative binding energies distance rather than absolute values. In our case, the Zn 2p was selected as reference for both ZnS and ZnO single crystal. In Fig.A.2 (a) and (b) are shown the band gap estimation for both systems. Our findings reinforces the reliability of this method.

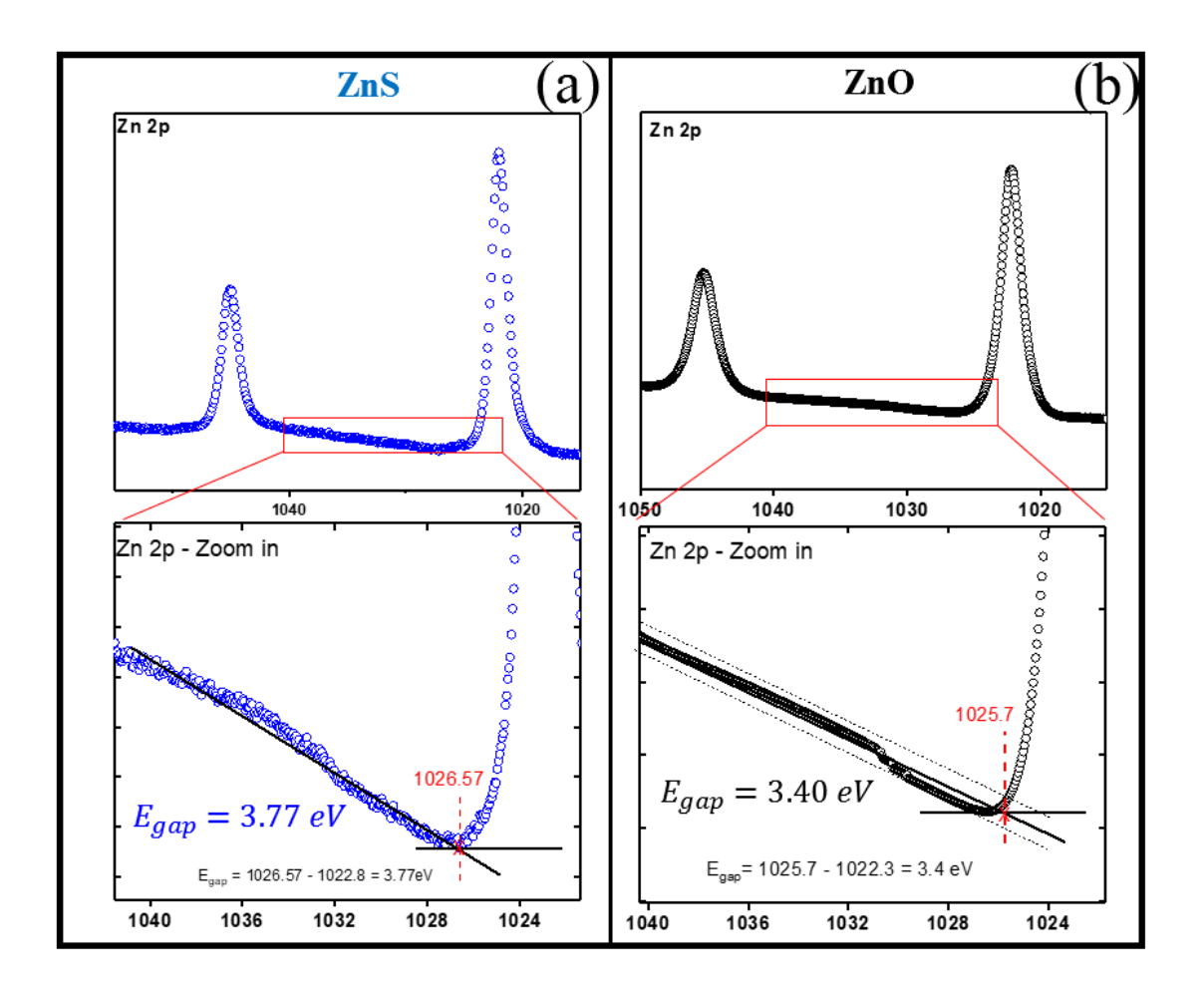


Figure A.2: The band gap estimation method applied on (ZnS) and (ZnO) systems.

Appendix B

Further Computational details

In this chapter we shortly describe one of the DFT methods employed in this thesis: the $PBE - \alpha$. Before explaining fundamental aspects of that approximation, we provided an overall description of the computational method used throughout this thesis.

B.1 Computational method

The ZnS system with and without defects were theoretically investigated through first-principles calculations based on the density functional theory (DFT), using the Quantum Espresso software [106]. For geometric optimization and electronic structures insights, the calculations were performed within the generalized gradient approximation (GGA), following the description Perdew, Burke and Enzenhorf [107] and employing ultra-soft pseudo-potential [108] to

solve the Kohn-Sham equations. The equilibrium lattice parameters were obtained through calculations with a $6\times6\times3$ **k**-mesh for the Brillouin zone integration using a Gaussian smearing function of $\sigma=0.05$ eV. For modeling the system with and without defect a $(2\times2\times1)$ supercell was constructed. The defective ZnS structures were obtained by removing one atom (vacancy defect) from the supercell, thus keeping the doping limit lower than 5%. The kinetic energy of the wave functions and density charge cutoffs were 38 Ry and 456 Ry, respectively. The calculations were considered converged when the Hellman-Feynman forces on each atom were less than 0.0001 eV / Å

To improve the description of the optical properties calculations, a mixing with Hartree and Fock to describe the exchange-correlation energy based on the $PBE-\alpha$ hybrid functional theory [31] was applied. In this regard, Norm-Conserving pseudo- potentials were used [109]. In our study, we employed $\alpha=0.27$, which was the best value matching the experimental band gap of 3.6 eV. Besides the energy cutoff of the wave functions kinetic energy in the reciprocal space, a cutoff on the Fock space with the same value was added to accelerate the convergence of the calculations. The optical properties were evaluated within the dipole approximation, following the random-phase approximation [110]. The absorption spectra are obtained by computing the average of the imaginary part of the dielectric tensor, which is obtained according to the Kramers-Kronig relations [111]. The JDOS was calculated employing a Gaussian occupation with the same smearing σ to ensure methodological consistency.

B.2 The $PBE - \alpha$ method

The following discussion is find in the documentation of the *Quantum Espresso* software. In general, hybrid functionals contain some amount of exact exchange, similar as in Hartree-Fock theory. So essentially the exchange correlation term will takes into account contributions from both PBE and Hartree calculations. In the case of $PBE - \alpha$, we have:

$$E_{xc}^{PBE-alpha} = \alpha E_x^{HF} + (1 - \alpha)E_x^{PBE} + E_c^{PBE}.$$
 (B.1)

The parameter α rules the amount of the HF/DF exchange, as explained by *Becke* [31]:

$$E_{xc}^{PBE-\alpha} = E_{xc}^{GGA} + \alpha (E_x^{HF} - E_x^{GGA}). \tag{B.2}$$

If we fix $\alpha = 1/4$ the method is called PBE0 i.e :

$$E_{xc}^{PBE0} = E_{xc}^{GGA} + \frac{1}{4}(E_x^{HF} - E_x^{GGA})$$
 (B.3)

The calculation of the "corrected potential" is proceeded by the following steps:

Bring the wavefunctions to the real space via FFT

$$\psi_{\mathbf{k}}(\mathbf{G}) \xrightarrow{FFT} \psi_{\mathbf{k}}(\mathbf{r})$$
 (B.4)

and then build "auxiliary charge densities":

$$\rho_q = \psi_{\mathbf{k}-\mathbf{q}}^* \psi_{\mathbf{k}}(\mathbf{r}) \tag{B.5}$$

Note those wavefunctions are the converged solutions of the Kohn-Sham equations following PBE methodology. Once the auxiliary charge densities are builded:

• Transfer it to reciprocal space by another FFT

$$\rho_q \xrightarrow{FFT} \rho_q(\mathbf{G}) \tag{B.6}$$

• Solve Poisson equation to compute the potential $V_q(\mathbf{G})$

$$V_q(\mathbf{G}) = \frac{4\pi e^2}{|\mathbf{q} + \mathbf{G}|^2} \rho_q(\mathbf{G})$$
(B.7)

• Return to real space and accumulate the results

$$\hat{V}_x \psi_{\mathbf{k}} = \hat{V}_x \psi_{\mathbf{k}} + \hat{V}_q(\mathbf{r}) \psi_{\mathbf{k} - \mathbf{q}}$$
(B.8)

Bibliography

- [1] D. A. Drabold, S. K. Estreicher, Theory of defects in semiconductors, Springer, 2007. 1.1
- [2] X. Shi, H. Xiao, H. Azarabadi, J. Song, X. Wu, X. Chen, K. S. Lackner, Sorbents for the direct capture of co2 from ambient air, Angewandte Chemie International Edition 59 (18) (2020) 6984–7006. 1.1
- [3] S. Ranjan, S. Balaji, R. A. Panella, B. E. Ydstie, Silicon solar cell production, Computers & Chemical Engineering 35 (8) (2011) 1439–1453. 1.1
- [4] X. Wang, H. Zhong, S. Xi, W. S. V. Lee, J. Xue, Understanding of oxygen redox in the oxygen evolution reaction, Advanced Materials 34 (50) (2022) 2107956. doi:10.1002/adma.202107956. 1.1
- [5] Y. Wang, J. Li, Z. Wei, Transition-metal-oxide-based catalysts for the oxygen reduction reaction, Journal of Materials Chemistry A 6 (18) (2018) 8194–8209. doi:10.1039/C8TA01321G. 1.1
- [6] J. Hwang, R. R. Rao, L. Giordano, Y. Katayama, Y. Yu, Y. Shao-Horn, Perovskites in catalysis and electrocatalysis, Science 358 (6364) (2017) 751–756. doi:10.1126/science.aam7092. 1.1

- [7] K. Ren, S. Yue, C. Li, Z. Fang, K. A. Gasem, J. Leszczynski, S. Qu, Z. Wang, M. Fan, Metal halide perovskites for photocatalysis applications, Journal of Materials Chemistry A 10 (2) (2022) 407–429. doi: 10.1039/D1TA09148D. 1.1
- [8] Z. Cheng, W. Qi, C. H. Pang, T. Thomas, T. Wu, S. Liu, M. Yang, Recent advances in transition metal nitride-based materials for photocatalytic applications, Advanced Functional Materials 31 (26) (2021) 2100553.
 doi:10.1002/adfm.202100553. 1.1
- [9] R. He, X. Huang, L. Feng, Recent progress in transition-metal sulfide catalyst regulation for improved oxygen evolution reaction, Energy & Fuels 36 (13) (2022) 6675–6694. doi:10.1021/acs.energyfuels.2c01429.
- [10] J. Wang, S. Lin, N. Tian, T. Ma, Y. Zhang, H. Huang, Nanostructured metal sulfides: classification, modification strategy, and solar-driven co2 reduction application, Advanced Functional Materials 31 (9) (2021) 2008008. 1.1
- [11] E. M. Davis, G. Berti, H. Kuhlenbeck, V. Vonk, A. Stierle, H.-J. Freund, Growth of well-ordered iron sulfide thin films, Physical Chemistry Chemical Physics 21 (36) (2019) 20204–20210. 1.1
- [12] M. Liu, S. Wang, C. Wang, G. Zhang, Y. Wang, X. Li, J. Chu, Understanding of electronic and optical properties of zns with high concentration of point defects induced by hot pressing process: The first-principles calculations, Computational Materials Science 174 (2020) 109492. doi: 10.1016/j.commatsci.2019.109492. 1.1, 4.3.4
- [13] Z. Wang, M. Xiao, J. You, G. Liu, L. Wang, Defect engineering in photocat-

- alysts and photoelectrodes: from small to big, Accounts of Materials Research 3 (11) (2022) 1127–1136. doi:10.1021/accountsmr.1c00201. 1.1, 5.2
- [14] L. Bao, Y. Dong, C. Dai, G. Xu, Y. Yang, X. Liu, D. Ma, Y. Jia, C. Zeng, Optimizing the electronic structure of zns via cobalt surface doping for promoted photocatalytic hydrogen production, Inorganic Chemistry 60 (20) (2021) 15712–15723. 1.1
- [15] H. Pang, X. Meng, P. Li, K. Chang, W. Zhou, X. Wang, X. Zhang, W. Jevasuwan, N. Fukata, D. Wang, et al., Cation vacancy-initiated co2 photoreduction over zns for efficient formate production, ACS Energy Letters 4 (6) (2019) 1387–1393. doi:10.1021/acsenergylett.9b00711. 1.1, 3.1
- [16] C. Shahi, J. Sun, J. P. Perdew, Accurate critical pressures for structural phase transitions of group iv, iii-v, and ii-vi compounds from the scan density functional, Physical Review B 97 (9) (2018) 094111. doi:10.1103/PhysRevB.97.094111. 1.1
- [17] M. M. Khan, K. O. Abdulwahab, Metals-and non-metals-doped zns for various photocatalytic applications, Materials Science in Semiconductor Processing 181 (2024) 108634. doi:/10.1016/j.mssp.2024.108634.
 1.1
- [18] J. Yoon, I. T. Kim, J. Bae, J. Hur, High-performance zns@ graphite composites prepared through scalable high-energy ball milling as novel anodes in lithium-ion batteries, Journal of Industrial and Engineering Chemistry 76 (2019) 258–267. doi:/10.1016/j.jiec.2019.03.050. 1.1

- [19] F. A. Stevie, C. L. Donley, Introduction to x-ray photoelectron spectroscopy, Journal of Vacuum Science & Technology A 38 (6) (2020). 2.1, 2.3
- [20] R. Al-Gaashani, S. Radiman, A. Daud, N. Tabet, Y. Al-Douri, Xps and optical studies of different morphologies of zno nanostructures prepared by microwave methods, Ceramics International 39 (3) (2013) 2283–2292. doi:10.1016/j.ceramint.2012.08.075. 2.1
- [21] G. Greczynski, L. Hultman, X-ray photoelectron spectroscopy: Towards reliable binding energy referencing, Progress in Materials Science 107 (2020) 100591. 2.1
- [22] G. Greczynski, L. Hultman, A step-by-step guide to perform x-ray photoelectron spectroscopy, Journal of Applied Physics 132 (1) (2022). 2.2, 2.1, 3.2
- [23] Thermo scientific reports, https://xpssimplified.com/elements/zinc.php, accessed: 2020-04-21. 2.2
- [24] A. G. Shard, Practical guides for x-ray photoelectron spectroscopy: Quantitative xps, Journal of Vacuum Science & Technology A 38 (4) (2020). 2.1
- [25] Peak fitting in casa xps, http://www.casaxps.com/help_manual/manual_updates/peak_fitting_in_xps.pdf. 2.1
- [26] P. J. Cumpson, The thickogram: a method for easy film thickness measurement in xps, Surface and Interface Analysis: An International Journal devoted to the development and application of techniques for the analysis of surfaces, interfaces and thin films 29 (6) (2000) 403–406. doi:

- 10.1002/1096-9918(200006)29:6<403::AID-SIA884. **2.1**, **5.3.1**, A.3, A.1
- [27] P. Hohenberg, W. Kohn, Inhomogeneous electron gas, Physical review 136 (3B) (1964) B864. doi:10.1103/PhysRev.136.B864. 2.2
- [28] J. D. M. Vianna, Teoria Quântica de Moléculas e Sólidos: simulação computacional, Livraria da Física, 2004. 2.2, 2.2
- [29] J. P. Perdew, K. Burke, M. Ernzerhof, Generalized gradient approximation made simple (vol 77, pg 3865, 1996) (1997). doi:10.1103/PhysRevLett.77.3865.2.2
- [30] J. P. Perdew, W. Yang, K. Burke, Z. Yang, E. K. Gross, M. Scheffler, G. E. Scuseria, T. M. Henderson, I. Y. Zhang, A. Ruzsinszky, et al., Understanding band gaps of solids in generalized kohn–sham theory, Proceedings of the national academy of sciences 114 (11) (2017) 2801–2806. doi:10.1073/pnas.1621352114. 2.2
- [31] A. D. Becke, Density-functional thermochemistry. iv. a new dynamical correlation functional and implications for exact-exchange mixing, The Journal of Chemical Physics 104 (3) (1996) 1040–1046. doi:10.1063/1.470829. 2.2, B.1, B.2
- [32] B. G. Janesko, Replacing hybrid density functional theory: motivation and recent advances, Chemical Society Reviews 50 (15) (2021) 8470–8495. 2.2
- [33] X. Leng, F. Jin, M. Wei, Y. Ma, Gw method and bethe–salpeter equation for calculating electronic excitations, Wiley Interdisciplinary Reviews: Computational Molecular Science 6 (5) (2016) 532–550. 2.2

- [34] P. Giannozzi, S. Baroni, N. Bonini, M. Calandra, R. Car, C. Cavazzoni, D. Ceresoli, G. L. Chiarotti, M. Cococcioni, I. Dabo, et al., Quantum espresso: a modular and open-source software project for quantumsimulations of materials, Journal of physics: Condensed matter 21 (39) (2009) 395502. doi:2.doi:10.1088/09538984/21/39/395502. 2.2, 4.2
- [35] S. Zhang, S.-H. Wei, A. Zunger, Intrinsic n-type versus p-type doping asymmetry and the defect physics of zno, Physical Review B 63 (7) (2001) 075205. doi:10.1103/PhysRevB.63.075205. 3.1
- [36] L. Li, C. Yao, L. Wu, K. Jiang, Z. Hu, N. Xu, J. Sun, J. Wu, Zns covering of zno nanorods for enhancing uv emission from zno, The Journal of Physical Chemistry C 125 (25) (2021) 13732–13740. doi:10.1021/acs.jpcc.1c02971. 3.1
- [37] C. Noguera, Polar oxide surfaces, Journal of Physics: Condensed Matter 12 (31) (2000) R367. doi:10.1088/0953-8984/12/31/201. 3.1
- [38] P. Oliveira, C. Arrouvel, F. Stavale, Zinc blende zns (001) surface structure investigated by xps, leed, and dft, Vacuum 229 (2024) 113566. doi:10. 1016/j.vacuum.2024.113566. 3.1, 4.3.1, 4.3.2, 5.3.1, 5.3.2, 6.3.2, 6.3.3
- [39] N. Dengo, A. Vittadini, M. M. Natile, S. Gross, In-depth study of zns nanoparticle surface properties with a combined experimental and theoretical approach, The Journal of Physical Chemistry C 124 (14) (2020) 7777–7789. doi:10.1021/acs.jpcc.9b11323. 3.2, 4.3.1
- [40] D. Barreca, A. Gasparotto, C. Maragno, E. Tondello, T. R. Spalding, Analysis of nanocrystalline zns thin films by xps, Surface Science Spectra 9 (1) (2002) 54–61. doi:10.1116/11.20030117. 3.2, 4.3.1

- [41] D. W. Langer, C. J. Vesely, Electronic core levels of zinc chalcogenides, Physical Review B 2 (12) (1970) 4885. doi:10.1103/PhysRevB.2.4885.3.2
- [42] A. Ferraz, K. Watari, J. Alves, Surface electronic properties of zns, znse and znte (110), Surface science 307 (1994) 959–962. doi:10.1016/0039-6028(94)91523-7.3.2
- [43] P. Tasker, The stability of ionic crystal surfaces, Journal of Physics C: Solid State Physics 12 (22) (1979) 4977. doi:10.1088/0022-3719/12/22/036. 3.2
- [44] Leedpat, version 4.2, utility by k.e. hermann (fhi) and m.a. van hove (hkbu), berlin / hong kong, 2014, http://www.fhi-berlin.mpg.de/ KHsoftware/LEEDpat/index.html. 3.2
- [45] A. Janotti, C. G. V. de Walle, Native point defects in zno, Physical Review B—Condensed Matter and Materials Physics 76 (16) (2007) 165202. doi: 10.1103/PhysRevB.76.165202. 4.1, 4.3.3
- [46] P. R. A. de Oliveira, L. Lima, G. Felix, F. Stavale, P. Venezuela, Formation mechanism, stability, and role of zinc and sulfur vacancies on the electronic properties and optical response of zns, Journal of Physics D: Applied Physics 58 (2025) 385305. doi:10.1088/1361-6463/ae048a. 4.2, 5.3.1, 6.3.2, 6.3.3
- [47] J. H. Scofield, Hartree-slater subshell photoionization cross-sections at 1254 and 1487 ev, Journal of Electron Spectroscopy and Related Phenomena 8 (2) (1976) 129–137. doi:10.1016/0368-2048 (76) 80015-1. 4.3.1

- [48] D. R. Baer, K. Artyushkova, H. Cohen, C. D. Easton, M. Engelhard, T. R. Gengenbach, A. Roberts, Xps guide: Charge neutralization and binding energy referencing for insulating samples, Journal of Vacuum Science & Technology A 38 (3) (2020). doi:10.1116/6.0000057. 4.3.2
- [49] M. Cöpuroğlu, H. Sezen, R. L. Opila, S. Suzer, Band-bending at buried sio2/si interface as probed by xps, ACS Applied Materials & Interfaces 5 (12) (2013) 5875–5881. doi:10.1021/am401696e. 4.3.2
- [50] H. Hu, W. Zhang, Synthesis and properties of transition metals and rareearth metals doped zns nanoparticles, Optical Materials 28 (5) (2006) 536– 550. doi:10.1016/j.optmat.2005.03.015. 4.3.2
- [51] K. Hoang, Rare-earth defects and defect-related luminescence in zns, Journal of Applied Physics 131 (1) (2022). doi:10.1063/5.0069390. 4.3.2
- [52] S. Zott, K. Leo, M. Ruckh, H. W. Schock, Radiative recombination in cuinse2 thin films, Journal of Applied Physics 82 (1) (1997) 356–367. doi:10.1063/1.366546.4.3.2,4.3.5
- [53] J. Yao, Y. Li, N. Li, S. Le, Theoretical investigations of the effect of vacancies on the geometric and electronic structures of zinc sulfide, Physica B: Condensed Matter 407 (18) (2012) 3888–3892. doi:10.1016/j.physb. 2012.06.016. 4.3.3
- [54] J. P. Perdew, W. Yang, K. Burke, Z. Yang, E. K. Gross, M. Scheffler, A. Görling, Understanding band gaps of solids in generalized kohn–sham theory, Proceedings of the National Academy of Sciences 114 (11) (2017) 2801–2806. doi:10.1073/pnas.1621352114. 4.3.4

- [55] Y. Li, H. Shu, S. Wang, J. Wang, Electronic and optical properties of graphene quantum dots: The role of many-body effects, The Journal of Physical Chemistry C 119 (9) (2015) 4983–4989. doi:10.1021/jp506969r. 4.3.5
- [56] R. Webster, L. Bernasconi, N. M. Harrison, Optical properties of alkali halide crystals from all-electron hybrid td-dft calculations, The Journal of Chemical Physics 142 (21) (2015). doi:10.1063/1.4921822. 4.3.5
- [57] S. Gautam, H. Agrawal, M. Thakur, A. Akbari, H. Sharda, R. Kaur, M. Amini, Metal oxides and metal organic frameworks for the photocatalytic degradation: A review, Journal of Environmental Chemical Engineering 8 (3) (2020) 103726. doi:10.1016/j.jece.2020.103726. 5.1
- [58] F. Jamal, A. Rafique, S. Moeen, J. Haider, W. Nabgan, A. Haider, M. Imran, G. Nazir, M. Alhassan, M. Ikram, et al., Review of metal sulfide nanostructures and their applications, ACS Applied Nano Materials 6 (9) (2023) 7077–7106. doi:10.1021/acsanm.3c00417. 5.1
- [59] S. Chen, A. M. Abdel-Mageed, C. Mochizuki, T. Ishida, T. Murayama, J. Rabeah, M. Parlinska-Wojtan, A. Bruckner, R. J. Behm, Controlling the ovacancy formation and performance of au/zno catalysts in co2 reduction to methanol by the zno particle size, ACS Catalysis 11 (15) (2021) 9022–9033. doi:10.1021/acscatal.1c01415. 5.1
- [60] B. Song, L.-H. Xie, H2 activation mechanisms on zno-based catalysts, The Journal of Physical Chemistry C 129 (10) (2025) 4825–4840. doi: 10.1021/acs.jpcc.4c08549.5.1
- [61] X. Fu, J. Li, J. Long, C. Guo, J. Xiao, Understanding the product selectivity

- of syngas conversion on zno surfaces with complex reaction network and structural evolution, ACS Catalysis 11 (19) (2021) 12264–12273. doi:10.1021/acscatal.1c02111. 5.1
- [62] X. Xu, S. Li, J. Chen, S. Cai, Z. Long, X. Fang, Design principles and material engineering of zns for optoelectronic devices and catalysis, Advanced Functional Materials 28 (36) (2018) 1802029. doi:10.1002/ adfm.201802029. 5.1
- [63] H. Jiang, H. Peng, H. Guo, Y. Zeng, L. Li, Y. Zhang, Y. Chen, X. Chen, J. Zhang, R. Chu, Interfacial mechanical strength enhancement for high-performance zns thin-film anodes, ACS Applied Materials & Interfaces 12 (46) (2020) 51344–51356. doi:10.1021/acsami.0c13139. 5.1
- [64] X. Hao, Y. Wang, J. Zhou, Z. Cui, Y. Wang, Z. Zou, Zinc vacancy-promoted photocatalytic activity and photostability of zns for efficient visible-light-driven hydrogen evolution, Applied Catalysis B: Environmental 221 (2018) 302–311. doi:10.1016/j.apcatb.2017.09.006.
- [65] W. Luo, A. Li, B. Yang, H. Pang, J. Fu, G. Chen, N. Zhang, Synthesis of a hexagonal phase zns photocatalyst for high co selectivity in co2 reduction reactions, ACS Applied Materials & Interfaces 15 (12) (2023) 15387–15395. doi:10.1021/acsami.2c21966. 5.1
- [66] H. Wang, L. Zhang, Z. Chen, J. Hu, S. Li, Z. Wang, J. Liu, X. Wang, Semiconductor heterojunction photocatalysts: design, construction, and photocatalytic performances, Chemical Society Reviews 43 (15) (2014) 5234– 5244. doi:10.1039/C4CS00126E. 5.2

- [67] D. Salazar-Marín, G. Oza, J. D. Real, A. Cervantes-Uribe, H. Pérez-Vidal, M. Kesarla, J. T. Torres, S. Godavarthi, Distinguishing between type ii and s-scheme heterojunction materials: A comprehensive review, Applied Surface Science Advances 19 (2024) 100536. doi:j.apsadv.2023. 100536. 5.2
- [68] A. Shabbir, S. Sardar, A. Mumtaz, Mechanistic investigations of emerging type-ii, z-scheme and s-scheme heterojunctions for photocatalytic applications-a review, Journal of Alloys and Compounds (2024) 175683.
 5.1
- [69] M. Cai, C. He, H. Yu, A. Shui, Fabrication of the ternary dual s-scheme zno/zns/in2s3 heterojunction for enhancing pollutant photodegradation, Applied Surface Science 652 (2024) 159284. doi:10.1016/j.apsusc. 2023.159284. 5.2
- [70] Z. Guo, W. Huo, T. Cao, X. Liu, S. Ren, J. Yang, H. Ding, K. Chen, F. Dong, Y. Zhang, Heterojunction interface of zinc oxide and zinc sulfide promoting reactive molecules activation and carrier separation toward efficient photocatalysis, Journal of Colloid and Interface Science 588 (2021) 826–837. doi:10.1016/j.jcis.2020.11.118.5.2
- [71] P. de Oliveira, I. Coelho, G. Felix, P. Venezuela, F. Stavale, Growth and surface characterization of a type-ii zno/zns heterostructure, The Journal of Physical Chemistry C (2025). doi:10.1021/acs.jpcc.5c05124. 5.3.1, 6.3.2, 6.3.2, 6.3.3
- [72] C. Dong, X. Zhang, W. Dong, X. Lin, Y. Cheng, Y. Tang, S. Zhao, G. Li, F. Huang, Zno/zns heterostructure with enhanced interfacial lithium absorption for robust and large-capacity energy storage, Energy & Environ-

- mental Science 15 (11) (2022) 4738–4747. doi:10.1039/D2EE00050D. 5.3.1
- [73] I. Fidelis, C. Stiehler, M. Duarte, C. Enderlein, W. Silva, E. A. Soares, S. Shaikhutdinov, H.-J. Freund, F. Stavale, Electronic properties of ultrathin o-terminated zno (0001⁻) on au (111), Surface Science 679 (2019) 259–263. 5.3.1
- [74] T. J. Frankcombe, Y. Liu, Interpretation of oxygen 1s x-ray photoelectron spectroscopy of zno, Chemistry of Materials 35 (14) (2023) 5468–5474. doi:10.1021/acs.chemmater.3c00801.5.3.1,6.3.2
- [75] A. J. Smith, C. H. Lee, X. Wang, The characterization of sox species on catalyst surfaces using xps: A review, Surface Science Reports 77 (5) (2022) 100574. doi:10.1016/j.surfrep.2022.100574. 5.3.1
- [76] S. Tanuma, C. J. Powell, D. R. Penn, Calculations of electron inelastic mean free paths. v. data for 14 organic compounds over the 50–2000 ev range, Surface and interface analysis 21 (3) (1994) 165–176. doi:10.1002/sia. 740210302. 5.3.1
- [77] M. R. Castell, T. Nguyen, J. A. Martin, Atomic-scale structure and surface relaxation of zno (0001) surfaces studied by stm and afm, Surface Science 723 (2022) 122015. doi:10.1016/j.susc.2022.122015. 5.3.2
- [78] P. Bhakuni, M. Krajčí, S. Roy Barman, Quasiperiodic gallium adlayer on i-al-pd-mn, Physical Review B 109 (4) (2024) 045427. doi:10.1103/PhysRevB.109.045427. 5.3.2
- [79] O. Dulub, U. Diebold, G. Kresse, Novel stabilization mechanism on polar surfaces: Zno (0001)-zn, Physical review letters 90 (1) (2003) 016102. 5.3.3

- [80] T. C. Taucher, I. Hehn, O. T. Hofmann, M. Zharnikov, E. Zojer, Understanding chemical versus electrostatic shifts in x-ray photoelectron spectra of organic self-assembled monolayers, The Journal of Physical Chemistry C 120 (6) (2016) 3428–3437. doi:10.1021/acs.jpcc.5b12387. 5.3.3
- [81] J. Fox, J. Nuttall, T. Gallon, Solid state effects in the auger spectrum of zinc and oxidised zinc, Surface Science 63 (1977) 390–402. doi:10.1016/0039-6028 (77) 90354-5. 5.3.3
- [82] K. Sawada, Y. Shirotori, K. Ozawa, K. Edamoto, M. Nakatake, Valence band structure of the zno (101⁻ 0) surface studied by angle-resolved photoemission spectroscopy, Applied surface science 237 (1-4) (2004) 343–347. doi:10.1016/j.apsusc.2004.06.100.5.3.4
- [83] F. Stavale, N. Nilius, H.-J. Freund, Stm luminescence spectroscopy of intrinsic defects in zno (0001) thin films, The Journal of Physical Chemistry Letters 4 (22) (2013) 3972–3976. doi:10.1021/jz401823c. 5.3.4
- [84] M. Nichols, W. Li, D. Pei, G. Antonelli, Q. Lin, S. Banna, Y. Nishi, J. L. Shohet, Measurement of bandgap energies in low-k organosilicates, Journal of Applied Physics 115 (9) (2014). doi:10.1063/1.4867644. 5.3.4, A.4
- [85] T. Schultz, M. Kneiss, P. Storm, D. Splith, H. von Wenckstern, M. Grundmann, N. Koch, Band offsets at κ-([al, in] x ga1-x) 2o3/mgo interfaces, ACS Applied Materials & Interfaces 12 (7) (2020) 8879–8885. doi:10.1021/acsami.9b21128.5.3.4
- [86] E. N. Jin, M. T. Hardy, A. L. Mock, J. L. Lyons, A. R. Kramer, M. J. Tadjer,

- N. Nepal, D. S. Katzer, D. J. Meyer, Band alignment of sc x al1–x n/gan heterojunctions, ACS Applied Materials & Interfaces 12 (46) (2020) 52192–52200. doi:10.1021/acsami.0c15912. 5.3.4
- [87] A. Torabi, V. N. Staroverov, Band gap reduction in zno and zns by creating layered zno/zns heterostructures, The Journal of Physical Chemistry Letters 6 (11) (2015) 2075–2080. 5.3.4
- [88] U.S. Department of Energy, Energy efficiency scaling for two decades: Research and development roadmap, accessed: 2025-04-03 (July 2022). 6.1
- [89] W. Orellana, A. J. Da Silva, A. Fazzio, Oxidation at the s i/s i o 2 interface: Influence of the spin degree of freedom, Physical review letters 90 (1) (2003) 016103. 6.2.2
- [90] S. B. Patel, J. Wang, C. Li, A. Al-Mahboob, D. Stacchiola, J. T. Sadowski, G. Zhou, Initiation of dusting corrosion in high-temperature alloys under co exposure, Acta Materialia (2025) 121178. 6.3.1
- [91] H. Zhang, L. Xie, C. Huang, Z. Ren, H. Wang, J. Hu, H. Zhang, Z. Jiang, F. Song, Exploring the co2 reduction reaction mechanism on pt/tio2 with the ambient-pressure x-ray photoelectron spectroscopy, Applied Surface Science 568 (2021) 150933. 6.3.1, 6.3.2
- [92] V. Mehar, J. Kim, A. Hunt, I. Waluyo, J. A. Rodriguez, Ap-xps study of the reaction of o2 and co2 with zn–au (111) surface alloys: Activation of o–o/c–o bonds and the formation of zno, The Journal of Physical Chemistry C 128 (33) (2024) 13852–13863. 6.3.2, 6.3.2
- [93] T. Koitaya, S. Yamamoto, Y. Shiozawa, K. Takeuchi, R.-Y. Liu, K. Mukai, S. Yoshimoto, K. Akikubo, I. Matsuda, J. Yoshinobu, Real-time obser-

- vation of reaction processes of co2 on cu (997) by ambient-pressure x-ray photoelectron spectroscopy, Topics in Catalysis 59 (5) (2016) 526–531. 6.3.2, 6.3.2
- [94] H.-J. Freund, M. W. Roberts, Surface chemistry of carbon dioxide, Surface Science Reports 25 (8) (1996) 225–273. 6.3.2
- [95] X. Deng, A. Verdaguer, T. Herranz, C. Weis, H. Bluhm, M. Salmeron, Surface chemistry of cu in the presence of co2 and h2o, Langmuir 24 (17) (2008) 9474–9478. 6.3.2, 6.3.2
- [96] Y. Yang, J. Evans, J. A. Rodriguez, M. G. White, P. Liu, Fundamental studies of methanol synthesis from co 2 hydrogenation on cu (111), cu clusters, and cu/zno (0001 [combining macron]), Physical Chemistry Chemical Physics 12 (33) (2010) 9909–9917. 6.3.2
- [97] Y. Li, Z. Zhao, M. Zhao, H. Zhu, X. Ma, Z. Li, W. Lu, X. Chen, L. Ying, R. Lin, et al., Oxygen-vacancy induced structural changes of co species in coal2o4 spinels for co2 hydrogenation, Applied Catalysis B: Environment and Energy 347 (2024) 123824. 6.3.2, 6.3.2
- [98] C. Zhou, H. T. Ngan, J. S. Lim, Z. Darbari, A. Lewandowski, D. J. Stacchiola, B. Kozinsky, P. Sautet, J. A. Boscoboinik, Dynamical study of adsorbate-induced restructuring kinetics in bimetallic catalysts using the pdau (111) model system, Journal of the American Chemical Society 144 (33) (2022) 15132–15142. 6.3.2
- [99] M. M. Montemore, M. A. Van Spronsen, R. J. Madix, C. M. Friend, O2 activation by metal surfaces: implications for bonding and reactivity on heterogeneous catalysts, Chemical reviews 118 (5) (2017) 2816–2862. 6.3.3

- [100] K. Li, J. Ge, E. Li, Z. Li, H. Wang, Y. Wang, Y. Zhou, J.-J. Zhu, A review of ii–vi semiconductor nanoclusters for photocatalytic co 2 conversion: synthesis, characterization, and mechanisms, EES Catalysis 1 (5) (2023) 687–694. 6.3.3
- [101] J. Yang, L. Z. Tan, A. M. Rappe, Hybrid functional pseudopotentials, Physical Review B 97 (8) (2018) 085130. 6.3.3
- [102] Y. Han, An evaluation for geometries, formation enthalpies, and dissociation energies of diatomic and triatomic (c, h, n, o), no3, and hno3 molecules from the paw dft method with pbe and optb88-vdw functionals, AIP Advances 12 (12) (2022). 6.3.3
- [103] R. van Bree, G. Kroes, O2 dissociation on cu (111) dynamics on a novel screened hybrid van der waals dft potential energy surface, The Journal of Physical Chemistry C 128 (45) (2024) 19182–19196. 6.3.3
- [104] C. Stampfl, M. Scheffler, Density-functional theory study of the catalytic oxidation of co over transition metal surfaces, Surface science 433 (1999) 119–126. 6.3.4
- [105] I. Horcas, R. Fernández, J. Gomez-Rodriguez, J. Colchero, J. Gómez-Herrero, A. M. Baro, Wsxm: A software for scanning probe microscopy and a tool for nanotechnology, Review of scientific instruments 78 (1) (2007). doi:10.1063/1.2432410. A.1
- [106] P. Giannozzi, S. Baroni, N. Bonini, M. Calandra, R. Car, C. Cavazzoni, R. M. Wentzcovitch, Quantum espresso: A modular and open-source software project for quantum simulations of materials, Journal of Physics:

- Condensed Matter 21 (39) (2009) 395502. doi:10.1088/0953-8984/21/39/395502. B.1
- [107] J. P. Perdew, K. Burke, M. Ernzerhof, Generalized gradient approximation made simple, Physical Review Letters 77 (18) (1996) 3865. doi: 10.1103/PhysRevLett.77.3865. B.1
- [108] D. Vanderbilt, Soft self-consistent pseudopotentials in a generalized eigenvalue formalism, Physical Review B 41 (11) (1990) 7892. doi: 10.1103/PhysRevB.41.7892. B.1
- [109] D. R. Hamann, Optimized norm-conserving vanderbilt pseudopotentials, Physical Review B—Condensed Matter and Materials Physics 88 (8) (2013) 085117. doi:10.1103/PhysRevB.88.085117. B.1
- [110] G. Onida, L. Reining, A. Rubio, Electronic excitations: density-functional versus many-body green's-function approaches, Reviews of modern physics 74 (2) (2002) 601. doi:10.1103/RevModPhys.74.601. B.1
- [111] S. Z. Karazhanov, P. Ravindran, A. Kjekshus, H. Fjellväg, B. G. Svensson, Electronic structure and optical properties of zn x (x= o, s, se, te): A density functional study, Physical Review B—Condensed Matter and Materials Physics 75 (15) (2007) 155104. doi:10.1103/PhysRevB.75. 155104. B.1